

DENSITY FUNCTIONAL INVESTIGATION OF NANO-STRUCTURES

A THESIS SUBMITTED TO
THE GRADUATE SCHOOL OF NATURAL AND APPLIED SCIENCES
OF
MIDDLE EAST TECHNICAL UNIVERSITY

BY

OLCAY ÜZENİ AKTÜRK

IN PARTIAL FULFILLMENT OF THE REQUIREMENTS
FOR
THE DEGREE OF DOCTOR OF PHILOSOPHY
IN
PHYSICS

JANUARY 2010

Approval of the thesis:

DENSITY FUNCTIONAL INVESTIGATION OF NANO-STRUCTURES

submitted by **OLCAY ÜZENĞİ AKTÜRK** in partial fulfillment of the requirements for the degree of **Doctor of Philosophy in Physics Department, Middle East Technical University** by,

Prof. Dr. Canan Özgen
Dean, Graduate School of **Natural and Applied Sciences**

Prof. Dr. Sinan Bilikmen
Head of Department, **Physics**

Prof. Dr. Mehmet Tomak
Supervisor, **Physics Department, METU**

Examining Committee Members:

Prof. Dr. Yakup Cevdet Akgöz
Engineering Sciences Dept., METU

Prof. Dr. Mehmet Tomak
Physics Dept., METU

Prof. Dr. Cevdet Tezcan
Mechanical Eng. Dept., Başkent University

Assoc. Prof. Dr. Hatice Kökten
Physics Dept., METU

Assoc. Prof. Dr. Sadi Turgut
Physics Dept., METU

Date:

I hereby declare that all information in this document has been obtained and presented in accordance with academic rules and ethical conduct. I also declare that, as required by these rules and conduct, I have fully cited and referenced all material and results that are not original to this work.

Name, Last Name: OLCA Y ÜZEN Gİ AKTÜRK

Signature :

ABSTRACT

DENSITY FUNCTIONAL INVESTIGATION OF NANO-STRUCTURES

Aktürk, Olcay Üzengi

Ph.D., Department of Physics

Supervisor : Prof. Dr. Mehmet Tomak

January 2010, 110 pages

In this thesis, we first investigate the physical properties of some metal atoms, molecules and their clusters. We then study the interaction of these with silicon and graphene surfaces. The adsorption of NH_3 and H_2S molecules on Au_3Pt_3 is also studied.

We calculate the equilibrium atomic structures of metal clusters using density functional theory (DFT) up to eight atoms. The electronic structures of these free and adsorbed clusters are also calculated in detail.

We find that the adsorption generally modifies the structure of the Au_3Pt_3 cluster and the adsorbate (NH_3 and H_2S).

We also study the site-dependent shapes of the Au_8 cluster, associated adsorption energies, band structures and the corresponding charge distribution for the $Si(100)$ asymmetric surface. We show that the electronic properties of the cluster and the substrate complex change with the location of the cluster on the surface.

We study the Au_nPt_n clusters on graphene surface. We observe that graphene can

be metallic or semiconducting depending on the number of *Au* and *Pt* atoms in the cluster and the charge transfer between the cluster and the graphene.

We have studied bismuth both as an adsorbate and substitutional dopant in graphene. We have shown that bismuth causes a weak p-type doping for the adsorption case within generalized gradient approximation (GGA), but it n-dopes graphene when it is substitutional and for the adsorption case within local density approximation (LDA). Our results are in agreement with recent angle-resolved photoemission results for the weak adsorption.

Keywords: DFT, clusters, silicon, graphene

ÖZ

NANO YAPILARIN YOĞUNLUK FONKSİYONEL TEORİSİ İLE İNCELEMESİ

Aktürk, Olcay Üzengi

Doktora, Fizik Bölümü

Tez Yöneticisi : Prof. Dr. Mehmet Tomak

Ocak 2010, 110 sayfa

Tezde, ilk olarak bazı metal atomlarının, kümelerin ve moleküllerin fiziksel özelliklerini inceledik. Daha sonra silisyum ve grafin yüzeyi ile bu yapılar arasındaki etkileşimleri çalıştık. Ayrıca Au_3Pt_3 üzerine NH_3 ve H_2S ' in bağlanması çalışıldı.

Metal kümelerinin, yoğunluk fonksiyonel teorisi (YFT) kullanarak, atomik kararlı yapıları sekiz atoma kadar hesapladık. Bu kümelerin serbest ve yüzeyle bağ oluşturma durumundaki elektronik yapıları detaylı bir biçimde incelendi.

Bağlanmanın, hem Au_3Pt_3 kümesi hemde bağlanan NH_3 ve H_2S moleküllerinin yapısını değiştirdiği bulundu.

$Si(100)$ yüzeyi için, Au_8 kümesinin, yüzeyle bağlanma yerine bağlı olarak şeklini, bağlanma enerjisini, bant yapılarını ve karşılık gelen yük dağılımları çalışıldı. Kümenin ve alt tabanın elektronik özelliklerinin yüzey üzerindeki kümenin konumuna göre değiştiği gösterildi.

Grafin yüzeyi üzerine Au_nPt_n kümesi çalışıldı. Kümedeki Au ve Pt atomu sayısına ve

kümeden grafine yük geçişine bağlı olarak, grafinin metalik ve ya yarıiletken özellik gösterebileceği bulundu.

Grafin üzerine bizmut'un katkılanma ve bağlanma özelliği incelendi. Genelleştirilmiş gradient yaklaşımı için (GGY), Bizmut, bağlanma durumunda zayıf p-tipi katkılanmaya sebep olur, fakat yerel yoğunluk yaklaşımı (YYY) için n-tipi katkılanmaya neden olur. Elde ettiğimiz sonuçlar zayıf bağlanma için açılma -ayrışımı yapılmış foto-yayılım sonucu ile uyumludur.

Anahtar Kelimeler: YFT, kümeler, silisyum, grafin

To My Father, My Mother and My Husband

ACKNOWLEDGMENTS

I would like to express my deep and sincere feelings to my supervisor Prof. Dr. Mehmet Tomak. I am very grateful to him for his effort in teaching me numerous concepts and useful discussion on physics during my PhD education. Without him, all this work would have not been possible.

I would like to thank to the examining committee members for their valuable hints that helped and encouraged me to go ahead with my thesis.

I would like to thank my loved husband. I am deeply thankful to him for encouraging me and being always with me. I want to also thank him for his support during PhD. I would like to express my deep sincere and love feelings to my father and mother lives at my heart. They always supported me during their life time.

I would like to thank also TUBİTAK. The numerical calculations reported in this thesis were performed at TUBITAK ULAKBİM, High Performance and Grid Computing Center (TR-Grid e-Infrastructure).

I would like to thank also METU Graduate School of Natural and Applied Sciences. A part of this thesis was supported by METU Graduate School of Natural and Applied Sciences (No: BAP-2006-07.02-00-01).

TABLE OF CONTENTS

ABSTRACT	iv
ÖZ	vi
DEDICATION	viii
ACKNOWLEDGMENTS	ix
TABLE OF CONTENTS	x
LIST OF TABLES	xii
LIST OF FIGURES	xiv
CHAPTERS	
1 INTRODUCTION	1
2 DENSITY FUNCTIONAL THEORY	9
2.1 Born-Oppenheimer Approximation	10
2.2 The Hartree-Fock Approximation	12
2.3 Thomas-Fermi Theory	16
2.4 Basis of The Density Functional Theory	18
2.4.1 The Hohenberg-Kohn Theorem	18
2.4.2 The Kohn-Sham Equation	20
2.4.3 Local Density Approximation (LDA)	25
2.4.4 Generalized Gradient Approximation (GGA)	26
2.4.4.1 Langreth-Mehl Functional	27
2.4.4.2 BLYP Functional	27
2.4.4.3 PBE Functional and Its Revisions	28
2.4.5 Pseudopotentials	29
2.4.5.1 Ultrasoft Pseudopotentials	32

3	LOW DIMENSIONAL SYSTEMS BASED ON CLUSTERS	35
3.1	Computational Details	38
3.2	The Stable Configuration of Pt,Cu, Clusters	39
3.3	Vibrational Modes and The Stable Configurations of Au Clusters . .	40
3.4	Vibrational Modes and The Stable Configurations of Ag Clusters . .	45
3.5	The Stable Configurations Of Au_nPt_m Clusters	48
3.6	NH ₃ and H ₂ S Adsorption on Au_3Pt_3 Cluster	50
3.6.1	Computational Details	50
3.6.2	The Electronic Properties of NH ₃ and H ₂ S Adsorption on Au_3Pt_3 Cluster	51
4	Au ₈ CLUSTER ADSORPTION ON Si(100):2x1 ASYMMETRIC SURFACE	61
4.1	Computational Details	63
4.2	Si Bulk and Si(100):2x1 Asymmetric Surface	64
4.3	Electronic and Structure Properties Analysis	65
5	CLUSTERS ADSORPTION ON GRAPHENE	72
5.1	Graphene	72
5.2	Au_nPt_n Clusters Adsorbed on Graphene	75
5.2.1	Computational Details	77
5.2.2	Electronic Properties of Au_nPt_n Clusters Adsorbed on Graphene	78
5.3	Bismuth Doping of Graphene	86
5.3.1	Computational Details	87
5.3.2	The Adsorption and Substitution and Electronic Properties of Bi and Bi_2 on Graphene	88
6	CONCLUSION	94
	REFERENCES	98
	VITA	109

LIST OF TABLES

TABLES

Table 3.1	The Bond length and binding energies of <i>Pt</i> and <i>Cu</i> clusters.	39
Table 3.2	The dimer length and binding energy of Au clusters [19].	41
Table 3.3	The normal mode frequency of <i>Au</i> ₂ [19].	44
Table 3.4	The dimer length and binding energy of Ag clusters [19].	47
Table 3.5	The normal mode frequency of <i>Ag</i> ₂ [19].	47
Table 3.6	GGA results for <i>NH</i> ₃ on <i>Au</i> ₃ <i>Pt</i> ₃ : adsorption energies E_a (eV), bond lengths (d) (Å), the total charge transfer from the adsorbate to <i>Au</i> ₃ <i>Pt</i> ₃ ($\Delta\rho$), total magnetization (M)($\mu_B/cell$) for all sites, NB stands for 'not binding' [24].	53
Table 3.7	LDA results for <i>NH</i> ₃ on <i>Au</i> ₃ <i>Pt</i> ₃ : adsorption energies E_a (eV), bond lengths (d) (Å), the total charge transfer from the adsorbate to <i>Au</i> ₃ <i>Pt</i> ₃ ($\Delta\rho(e)$), total magnetization (M) ($\mu_B/cell$)for all sites [24].	55
Table 3.8	GGA results for <i>H</i> ₂ <i>S</i> on <i>Au</i> ₃ <i>Pt</i> ₃ : E_a (eV), bond lengths (d) (Å) and the total charge transfer from the adsorbate to <i>Au</i> ₃ <i>Pt</i> ₃ ($\Delta\rho(e)$), total magnetization (M) ($\mu_B/cell$) for all sites [24].	57
Table 3.9	LDA results for <i>H</i> ₂ <i>S</i> on <i>Au</i> ₃ <i>Pt</i> ₃ : E_a (eV), bond lengths (d) (Å)the total charge transfer from the adsorbate to <i>Au</i> ₃ <i>Pt</i> ₃ ($\Delta\rho(e)$), the total magnetization (M) ($\mu_B/cell$)for all sites [24].	59
Table 4.1	The adsorption energies and bond lengths of <i>Au</i> ₈ cluster for different sites on the Si(100):(2x1) surface [2].	65
Table 5.1	<i>Au</i> and <i>Pt</i> on graphene: the bond length (d) the adsorption energy (E_a) and the total charge transfer from the graphene to <i>Au</i> and from <i>Pt</i> to graphene for the most stable relaxed position calculated by using LDA and GGA [3].	79

Table 5.2	$AuPt$ on graphene: the bond length (d) the adsorption energy (E_a) and the total charge transfer from the graphene to $AuPt$ for the most stable relaxed position calculated by using LDA and GGA [3].	81
Table 5.3	Au_2Pt_2 on graphene: the bond length (d) the adsorption energy (E_a) and the total charge transfer from the Au_2Pt_2 to graphene for the most stable relaxed position calculated by using LDA and GGA [3].	83
Table 5.4	Au_3Pt_3 on graphene: the bond length (d) the adsorption energy (E_a) the total charge transfer from the graphene to Au_3Pt_3 for the most stable relaxed position calculated by using LDA and GGA [3].	83
Table 5.5	Bi_n on graphene: a lattice parameter, the adsorption energy E_a , substitutional energy E_{sub} and the charge transfer from the atom to graphene (+) , graphene to atom (-) for the most stable relaxed position [43].	91
Table 5.6	Bond length for the most stable relaxed position [43].	91

LIST OF FIGURES

FIGURES

Figure 2.1	KS-chart [6, 14]	24
Figure 2.2	The real and the pseudo wavefunction and potentials match above a certain cutoff radius r_c [219]	29
Figure 3.1	The stable structures of Pt and Cu clusters within GGA and LDA.	40
Figure 3.2	The stable structures of Au_n (a) within GGA and (b) LDA, (c) DOS and partial DOS of Au_8 LDA (d) STM image for HOMO of Au_8 GGA, (e) STM image for LUMO of Au_8 GGA [19].	42
Figure 3.3	Vibration modes of stable configuration of Au_n clusters obtained by using (a) GGA and (b) LDA [19].	43
Figure 3.4	The stable structures of Ag_n (a) within GGA and (b) LDA, (c) DOS and partial DOS of Ag_8 LDA (d) STM image for LUMO of Ag_8 GGA, (e) STM image for HOMO of Ag_8 GGA [19].	45
Figure 3.5	Vibration modes of stable configuration of Ag_n clusters obtained by using (a) GGA and (b) LDA [19].	48
Figure 3.6	The stable structures of Au_nPt_m within GGA and LDA.	49
Figure 3.7	Au_3Pt_3 - NH_3 and - H_2S within GGA, (a) the stable configuration of Au_3Pt_3 , (b) initial (left) and final (right) configurations at H1 (c) initial (left) and final (right) configurations at H2, (d) initial (left) and final (right) configurations at T1, (e) initial (left) and final (right) configurations at T2, (f) initial (left) and final (right) configurations at B1, (g) initial (left) and final (right) configurations at H1 for Au_3Pt_3 - H_2S , (h) initial (left) and final (right) configurations of H2, (i) initial (left) and final (right) configurations at T1, (j) initial (left) and final (right) configurations at T2, (k) initial (left) and final (right) configurations at B1 [24]. . .	52

Figure 3.8 Energy levels and charge densities Au_3Pt_3 within NH_3 for GGA; (a) bare Au_3Pt_3 (b) H1, (c) H2, (d) T1, (e) T2, (f) B1 (line shows spin up states. Dashed line shows spin down states) [24].	54
Figure 3.9 $Au_3Pt_3-NH_3$ and $Au_3Pt_3-H_2S$ for LDA, (a) initial (left) and final (right) configurations at T1 (b) initial (left) and final (right) configurations at T2, (c) initial (left) and final (right) configurations at B2, (d) initial (left) and final (right) configurations at H2 for $Au_3Pt_3-H_2S$, (e) initial (left) and final (right) configurations at T1 for $Au_3Pt_3-H_2S$, (f) initial (left) and final (right) configurations at T2 for $Au_3Pt_3-H_2S$, (g) initial (left) and final (right) configurations at B2 for $Au_3Pt_3-H_2S$ [24].	55
Figure 3.10 Energy levels and charge densities within $Au_3Pt_3-NH_3$ and $Au_3Pt_3-H_2S$ for LDA; (a) NH_3 at T1 -site, (b) NH_3 at T2 -site, (c) NH_3 at B2- site, (d) H_2S at H2 -site, (e) H_2S at T1 -site (f) H_2S at T2 -site, (g) H_2S at B2 -site [24].	56
Figure 3.11 Energy levels and charge densities within $Au_3Pt_3-H_2S$ for GGA; (a) H1, (b) H2, (c) T1, (d) T2, (e) B1 [24].	58
Figure 3.12 Energy levels and charge densities within $Au_3Pt_3-H_2S$ for B2 within LDA [24].	59
Figure 4.1 (a) The bulk structure of Si , (b) The band structure of bulk Si , (c) Top view of the ideal surface (Smaller and darker circles show deeper atoms) [160], (d) $p(2\times 1)$ asymmetric surface [160].	64
Figure 4.2 The configuration of Au_8 on $H-Si$ (100) system a) orthorhombic unit cell and stable configurations of Au_8 cluster adsorption on different sites of the H-terminated Si (100) surface [2].	66
Figure 4.3 Electronic energy bands of Au_8 on $H-Si$ (100) system for the Au_8 cluster on the B-, G- sites and for the bare H -terminated Si (100) within LDA [2].	67
Figure 4.4 Electronic energy bands of Au_8 on $H-Si$ (100) system for the Au_8 cluster on the P- and T- sites within LDA [2].	68
Figure 4.5 The charge density of Au_8 on $H-Si$ (100) system for the Au_8 cluster on the G-site site within LDA [2].	69

Figure 4.6 The density of states (DOS) of Au_8 on $H-Si(100)$ and partial density of states (PDOS) for Au_8 cluster for different sites. the Local density of states (LDOS) are given for different layers of the the Au_8 . (the first layer is two Au atoms closest to the surface (as shown in Fig.4.2 (b)) for B-G-P- sites, and it is the five Au atoms for T-site (as shown in Fig.4.2 (b)) (a) DOS and PDOS for B- site (b) LDOS for B-site (c) (DOS) and (PDOS) for G-site (d) LDOS for G-site (e) DOS and PDOS T-site (f) LDOS for T-site (g) DOS and PDOS for P-site (h) LDOS for P-site (i) DOS and PDOS for P-site GGA (j) LDOS for P-site GGA [2]. 70

Figure 4.7 Electronic energy band of Au_8 on $H-Si(100)$ system for the Au_8 cluster on the P-site within GGA [2]. 71

Figure 5.1 Graphene can be wrapped up into 0D fullerenes, rolled into 1D nanotubes or stacked into 3D graphite [35]. 73

Figure 5.2 Band structure of graphene. (The conductance band touches the valence band at the K and K' points) [169]. 74

Figure 5.3 The Au_nPt_n -graphene structures within LDA. B: bridge site, H: hollow site and T: top site (a) the stable configuration of Au -graphene.(b) the stable configuration of Pt -graphene. (c) initial (left) and final (right) configurations of $AuPt$ -graphene. (d) initial (left) and final (right) configurations of Au_2Pt_2 -graphene. (e) initial (left) and final (right) configurations of Au_3Pt_3 -graphene [3]. 79

Figure 5.4 The Au_nPt_n -graphene structures within GGA. (a) the stable configuration of Au -graphene. (b) the stable configuration of Pt -graphene. (c) initial (left) and final (right) configurations of $AuPt$ -graphene. (d) initial (left) and final (right) configurations of Au_2Pt_2 -graphene. (e) initial (left) and final (right) configurations of Au_3Pt_3 -graphene. (f) initial (left) and final (right) configurations of Au_3Pt_3 -graphene [3]. 80

Figure 5.5 The charge differences between adsorbates and the graphene within LDA. The dark regions correspond to decrease in charge. The light regions correspond to increase in charge [3]. 81

Figure 5.6 The charge differences between adsorbates and the graphene within GGA. The dark regions correspond to decrease in charge. The light regions correspond to increase in charge. The charge differences are decomposed into their spin com- ponents [3].	82
Figure 5.7 The Energy band structures within LDA; (Note that spin-up and spin-down bands overlap exactly in LDA)(a) graphene (b) <i>Au</i> -graphene, (c) <i>Pt</i> -graphene, (d) <i>AuPt</i> -graphene, (e) <i>Au₂Pt₂</i> -graphene, (f) <i>Au₃Pt₃</i> -graphene [3].	84
Figure 5.8 The Energy band structures within GGA (a) <i>Au</i> -graphene, (b) <i>Pt</i> -graphene (Note that spin-up and spin-down bands overlap exactly), (c) <i>AuPt</i> -graphene, (d) <i>Au₂Pt₂</i> -graphene, (e) <i>Au₃Pt₃</i> -graphene (line; spin up bands. Dashed line; spin down bands) [3].	85
Figure 5.9 (a) The stable configuration of Bi on graphene within LDA, (b) The sta- ble configuration of <i>Bi₂</i> on graphene within LDA, (c) The stable configuration of substitutional <i>Bi</i> on graphene within GGA (conf1), (d) The stable configura- tion of substitutional <i>Bi₂</i> on graphene within GGA, (e) The charge differences of substitutional <i>Bi</i> on graphene (The dark regions correspond to decrease in charge, the light regions correspond to increase in charge), (f) The charge differences of substitutional <i>Bi₂</i> on graphene within spin up states, (g) The charge differences of substitutional <i>Bi₂</i> on graphene within spin down states, (h) Energy band struc- ture of bare graphene, (i) Energy band structure of graphene with Bi within LDA (line; spin-up bands. Dashed line; spin-down bands), (j) Energy band structure of graphene with <i>Bi₂</i> within LDA, (k) Energy band structure of graphene with substi- tutional <i>Bi</i> within GGA, (l) Energy band structure of graphene with substitutional <i>Bi₂</i> within GGA [43].	89
Figure 5.10 (a) The stable configuration of substitutional <i>Bi</i> on graphene within LDA (conf2), (b) The stable configuration of substitutional <i>Bi₂</i> on graphene within LDA (c) The charge differences of substitutional <i>Bi</i> on graphene (The dark regions cor- respond to decrease in charge, the light regions correspond to increase in charge), (d) The charge differences of substitutional <i>Bi₂</i> on graphene within LDA, (e) En- ergy band structure of graphene with substitutional <i>Bi</i> within LDA, (f) Energy band structure of graphene with substitutional <i>Bi₂</i> within LDA [43].	90

CHAPTER 1

INTRODUCTION

Nanotechnology is interested in small structures or small sized materials. The typical dimensions range from subnanometers to several hundred nanometers. Nanomaterials are receiving increasing attention with the development of nanotechnology. Materials in the micrometer scale mostly show physical properties the same as that of the bulk form. However, nanomaterials show unique properties when compared with their bulk counterparts. Nanomaterials have larger surface area to volume ratio than that of bulk materials. These properties turn out to be advantageous in many cases. For example; a crystal in the nanometer scale exhibits a low melting point and decreased lattice constants, due to the fact that surface atoms or ions form considerable fraction of the total number of atoms or ions. For the same reason the surface energy plays an important role in the thermal stability. In nanometer sizes, crystal structures become stable at much lower temperatures when compared with the bulk counterpart, for this reason ferroelectric and ferromagnetic materials may lose their ferroelectricity and ferromagnetism if their size is in nanometer scale. A bulk semiconductor turns into an insulator if the characteristic dimension is in nanometer range. Moreover, nanostructures show better catalytic activity. For example, while bulk gold does not show catalytic properties, *Au* nanocrystal have unique catalytic activity at low temperatures [1].

In this work, we are interested in new materials like as graphene. Moreover we are also interested in studying nanostructures such as clusters and their adsorption on surfaces. The quantum effects are rather effective in these nano structures. It is possi-

ble to change optical, electrical and magnetic behavior of materials [2, 3]. There are three important tools in investigating nanostructures; experimental tools, and theoretical and computational methods [4].

There are many experimental methods developed for studying the physical and chemical properties of nanostructures. Before we investigate the electronic properties, materials must be grown. One important aspect of these materials is their growth and characterization. This is a must for any experimental work. Spontaneous growth, template-based synthesis, electro -spinning and lithography are widely used for synthesis and formation of nanostructures.

The nanomaterials grown by the techniques summarized above should be characterized for their physical properties. One piece of information which is important for testing the theoretical results is the atomic positions in the system studied. The experimental characterization of nanomaterials largely depend on the surface analysis techniques and conventional characterization methods developed for bulk materials. One of them, XRD (X-ray diffraction) has long been used for crystal structures of solids, including lattice constant and geometry, description of unknown materials, orientation of single crystals, preferred orientation of polycrystals, defects, stress, determination of crystallinity, etc. In the characterization of nanoparticles, SEM (Scanning electron microscopy) and TEM (Transmission electron microscopy) together with electron diffraction is widely used. Optical spectroscopy is used for the determination of the size of semiconductor nanostructures. The resolution of the SEM is close to a few nanometers, and the instruments work at magnifications that are easily adjusted from 10 to over 300.000. In TEM, electrons are accelerated to approximately 1000keV and reflected onto a thin specimen by means of the condenser lens system. So, It is possible to obtain the information about the image and diffraction. SPM (Scanning probe microscopy) gives information about three-dimensional (3-D) real-space images. There are two major members of the SPM family, scanning tunnelling microscopy (STM) and atomic force microscopy (AFM)[1].

We have a variety of methods to use for studying the physical properties of these systems. The theoretical methods are so well developed that nowadays designing ma-

materials with desirable physical properties is possible. The electronic and ionic problems can be studied together in a truly first-principles approach, such as the well known Car-Parrinello method. There are also methods developed for studying these problems separately. For example, the tight-binding approximation and linear combination of atomic orbitals. Tight-Binding (TB) approximation is the simplest method that is used for calculating band structures, both theoretically and computationally [5]. It is based on simplifying the calculation of Hamiltonian matrix elements in atom-centered basis sets. The starting point of this approach is that electrons are localized in a single atom, but they can jump to neighboring atoms. TB methods are used widely from very basic empirical models to the most sophisticated ab-initio schemes, where the Hamiltonian matrix is derived from DFT and an orthogonal basis set of localized orbitals is built from atom-centered basis functions by means of an appropriate linear transformation [6].

The other efficient approach is the computational method. The approach includes broad methods such as Monte Carlo (MC), Molecular Dynamics (MD) and Car - Parrinello method.

MC method creates configurations randomly, and uses a special set of criteria for deciding whether or not to approve each configuration. These criteria satisfy the that probability of obtaining a given configuration is equal to its Boltzman factor, $\exp(-\vartheta(\mathbf{r}^N)/k_B T)$ where $\vartheta(\mathbf{r}^N)$ is found using the potential energy function. In this method, each new configuration of the system can be created by randomly moving a single atom or molecule. The potential energy function is used for calculating the energy of the new configuration of the system. In the case that the energy of the new configuration is lower than the energy of its predecessor, the new configuration is accepted. Otherwise, a random number is created between 0 and 1 and compared with this Boltzman factor. In the case that the random number is lower then the move is accepted and then new configuration becomes the next state.

Molecular Dynamics is based on Newton's mechanics. This means that it computes the 'real' dynamics of the system, from which time averages of properties can be computed. Sets of atomic positions are calculated by using Newton's equation of motion.

MD is a deterministic method, so it is possible to predict the state of the system from its current state. Very simple potentials, such as hard-sphere potential are used in the calculation on the first molecular dynamics simulation. Although hard-sphere model provides useful results, it is not ideal for simulating atomic or molecular systems. The force between two atoms or molecules alters continuously with their separation in the Lennard-Jones potential but there does not exist force between them until they collide if the collision is modelled by hard sphere potentials. The continuous nature of the more realistic potentials needs the equation of motion to be integrated by breaking the calculation into a series of very short time steps. The force on the atoms are calculated at each step, then merged with current positions and velocities for creating new positions and velocities a short time ahead. It is supposed that the force on each atom is constant during the time interval. MD creates a trajectory which describes how the dynamic variables change with time [8]. MD is based on statistical mechanics. The ergodic hypothesis relates the ensemble averages to measurements carried out for a single equilibrium system during the course of its natural evolution. MD follows the dynamics of the single system and generates averages [7].

There are some differences between MD and MC simulation. To most important differences, MD gives information about the time dependence of the properties of the system [8].

On the other hand, a first principles method is important when the chemistry of the system plays an important role [6]. Using the ab-initio total-energy calculation is economical since many physical properties are related to the total energy. One piece of theoretical apparatus is enough for calculating all physical properties that are related to total energies, on the other hand, completely different sets of experimental apparatus are needed for measuring these properties [9]. Quantum mechanical modelling has some advantages over experimental measurement in some cases, such as establishing and breaking of chemical bonds, changing environments, variable coordination etc.

A first-principles self-consistent MD approach is widely used. It can be performed by solving the electronic problem for the ground state within the Kohn-Sham approach to density functional theory [6]. DFT became very popular in quantum chemistry in

the 1990's. It is possible to study much larger system than those treated by traditional ab-initio methods by using DFT. Nowadays, traditional wave function methods, either variational or perturbative, can be used to obtain highly accurate results on smaller systems [10].

Another method is developed by Car and Parrinello (1985) [11]. This method is based on the minimization a single function through simulated annealing. However, several difficulties occur on much larger systems. Conjugate-gradient methods was developed to overcome these difficulties [12, 13, 9]. This method is based on the total -energy pseudo potential calculations instead of simulated annealing minimization [9]. In contrast to Born-Oppenheimer molecular dynamics, Car- Parrinello method solves the interacting electron and ion problem. In this approach, the total Kohn-Sham energy is described as a potential energy for electrons as a function of the position of the nuclei. The interesting property of this method is that it solves the problem by using both DFT and the MD method together. This is done by adding a fictitious kinetic energy for electronic states, which results in fictitious lagrangian for nuclei and electrons [14, 6]. Since the electronic and the ionic problems are solved simultaneously the method requires very large computing power.

Considering the available computing power, we prefer the DFT pseudo potential approach using the planewave-self-consistent field package (PWSCF)[15] and Vienna ab-initio simulation package (VASP) [16, 17] in our calculations.

We concentrate on nanostructures in this thesis, such as, clusters, the adsorption properties of *Si* surface and graphene using the computational method based on the DFT method. Metallic clusters are technologically important because of their catalytic activity and the metals such as *Au*, *Ag*, *Cu* and *Pt* play a major role in catalysis, colloidal chemistry, and medical science. The surface of clusters can completely change their physical properties [18]. From the scientific point of view, it is important to understand the atomic structure of clusters starting from the interactions between atoms [19].

The electronic properties and atomic structures of gold and silver clusters have been

theoretically investigated by several research groups [20, 21, 22, 23]. On the other hand, there is no detailed reported work on the electronic properties of them up to now, such as phonon modes and STM properties. So, we deal with the phonon modes and STM properties of *Au* and *Ag* clusters. Generally, *Au* and *Ag* clusters stay in two dimension (2D) up to a specific number. We see that our results are in agreement with the literature [22]. We studied vibrational modes in small Ag_n , Au_n clusters up to eight atoms. We have also calculated the normal mode and also scanning tunnelling microscope (STM) images for small clusters [19].

Bimetallic clusters and alloys show interesting properties such as catalysts with wide applications [24, 25]. The interactions between the two components in bimetallic clusters present a mutual influence on the neighboring atoms, such as *AuPt* alloy clusters. *AuPt* clusters may have better electronic properties of bare clusters. The interaction between *AuPt* clusters and molecules is important for technology. There exist several investigations on *AuPt* alloy clusters adsorption molecules [24]. On the other hand, there is no reported work on NH_3 and H_2S molecules on Au_3Pt_3 cluster, so we studied the adsorption of NH_3 and H_2S molecules on Au_3Pt_3 cluster [24]. The energy levels and the corresponding charge densities, adsorption energies, charge transfer and magnetization are calculated for different adsorption sites. We find that the adsorption generally modifies the structure of the Au_3Pt_3 cluster and the adsorbate [24].

In recent years, metallic cluster adsorption on silicon substrates is receiving increasing attention. The research in this field is important both from technological and purely scientific points of view [2, 26, 27, 28, 29, 30]. Moreover it is found that Au_8 cluster is the smallest clusters which show high catalytic property [31]. Recently, B.Yoon et al., [31] have studied catalytic properties of Au_8 cluster. They have investigated the charging effects on bonding and catalyzed oxidation of CO on Au_8 clusters on MgO . There exist materials which are widely used in technology and show unique properties. For example, silicon and carbon-based materials. The study on silicon surface is important for technology. It is widely used in the integrated circuit production. It is possible to change its electronic properties by doping. We studied Au_8

cluster adsorption on H -terminated $Si(100):2\times 1$ asymmetric surface. We find that the electronic properties of H -terminated $Si(100):2\times 1$ asymmetric surface change with the adsorption site [2].

Carbon, fundamental of all organic chemistry, is the most important element for life. Since it has flexibility of its bonding, an unlimited number of different structures with an equally large variety of physical properties exists [32]. Graphene is becoming the center of increasing attention because of its unusual transport and electronic properties [33, 3]. It is the two-dimensional 2D form of carbon densely packed in a honeycomb crystal lattice and it has high structural quality [3, 34, 35, 36, 37, 38, 39]. Graphene is therefore finding applications in many areas. There are several investigations on metal atom adsorption and impurities on graphene [3]. Metal-graphene interface is important in understanding the electronic transport through a graphene sheet [40, 41, 3].

The development of graphene-based nano-electronics depends on our ability to dope this material. The chemical doping of graphene is usually done by adsorbing atoms and/or molecules on its surface. n-type doping results if electrons are donated by the adsorbate to graphene. The alkali atoms, for example, are shown to release their valence electrons rather easily and act as agents for n-doping of graphene. p-type doping of graphene has turned out to be a real challenge. For p-type doping, it is the graphene that has to donate electrons to the adsorbate. This is shown to be the case for heavier atoms such as antimony and gold and molecules like N_2O_4 [3, 42, 43].

In a theoretical effort to understand the doping of graphene, we have discovered an interesting doping behavior of the Au_nPt_n clusters [3]. The type of doping depends on the number of Au and Pt -atoms in the cluster. Recently, I.Gierz et al., [42], have shown by angle-resolved photoemission spectroscopy that p-doping of epitaxial graphene on 4H-SiC (0001) is possible by the adsorption of Bi , Sb and Au . We investigate the adsorption of Bi and Bi_2 on free-standing graphene in more detail. We investigate also the substitutional doping of graphene by Bi [43]. We have shown that bismuth causes a weak p-type doping for the adsorption case, but it n-dopes graphene when it is substitutional. The organization of the thesis is as follows.

In chapter 2, We present the basic principles of DFT, Born-Oppenheimer and Hartree-Fock approximations, Thomas-Fermi and The Hohenberg-Kohn and The Kohn-Sham theorems. We give the brief description of GGA and LDA methods and the description of pseudopotential approach.

In the chapter 3, We present the equilibrium atomic structures, such as *Au*, *Ag*, *Cu* and *Pt* clusters and the vibrational modes of *Au* and *Ag* clusters. In this chapter, we investigate the electronic properties of these clusters. We find the stable configuration of these clusters. The vibrational modes of *Au* and *Ag* clusters are studied [19].

In chapter 4, we investigate the adsorption of Au_8 cluster onto H-terminated *Si*(100) : 2×1 asymmetric surface by density functional theory within local density and generalized gradient approximations. The site-dependent shape of Au_8 cluster, adsorption energies, band structures and the corresponding charge distribution are studied. We show that the electronic properties of the cluster and substrate complex change with the location of the cluster on the surface [2].

In the chapter 5, we present the adsorption of Au_nPt_n clusters on graphene surface. We give the electronic properties of the Au_nPt_n clusters on graphene surface [3]. We study bismuth both as an adsorbate and in-plane dopant in graphene [43].

The main body of this thesis depends on five published papers;

1. O. Üzengi Aktürk , O.Gülseren and M.Tomak, Int. J. Modern Phys. B, **23**,31, (2009), 5819.
2. Olcay Üzengi Aktürk and Mehmet Tomak, to be published in Thin Solid Films
3. Olcay Üzengi Aktürk and Mehmet Tomak, Phys. Rev. **B80**, (2009), 085417.
4. Olcay Üzengi Aktürk and Mehmet Tomak, submitted to Thin Solid Films
5. Olcay Üzengi Aktürk and Mehmet Tomak, submitted to Apl.Phys.Lett.

CHAPTER 2

DENSITY FUNCTIONAL THEORY

A theoretical approach concentrating on the particle density instead of the wave-function has many advantages. The physical properties of materials are mainly determined by the density distribution of electrons. An early approach in this area is the famous Thomas-Fermi approximation. L.H.Thomas and E.Fermi suggested that the full electronic density was the essential variable of the many-body problem at about the same time as Hartree (1927-1928) [6]. From this idea, it was derived a differential equation for the density without resorting to the one-electron orbital [44, 45]. The original Thomas-Fermi approximation was actually too rough, since the approximation used for kinetic energy of electron did not support the bound states. But, it establishes a fundamental platform for the later development of the DFT [6]. Density functional theory (DFT) is used to describe correlated many-body systems and based on independent-particle methods. DFT is a fundamental theory for calculation of electronic structures in condensed matter, and is getting increasing importance for quantitative studies of molecules and other finite system. The local density approximation (LDA) and generalized gradient approximation (GGA) within the Kohn-Sham approach give rise to widespread interest in DFT as the most promising approach for accurate, practical method in the theory of materials [14]. A famous paper written by P. Hohenberg and W. Kohn [46] in 1964 is the source of the modern formulation of DFT. They showed that the density can be considered as the "basic variable", that is, that all properties of the system can be taken as a unique functional of the ground state density. Hohenberg-Kohn argument is extended to finite temperature canonical and grand canonical ensembles by Mermin [47]. W. Kohn and L.J.Sham [48]

proposed formulation of DFT which has become the basis of much of present-day methods for treating electrons in atoms, molecules, and condensed matter [14]. DFT is based on some approximations. We give a brief description of these approximations below.

Before embarking on these approximations, it will be useful to give a brief description of the basic Born-Oppenheimer approximation which is crucial in separating the electron and the ionic problems.

2.1 Born-Oppenheimer Approximation

A condensed system is considered as a system consisting of interacting nuclei and electrons. It is known that motion of nuclei is usually much slower than electrons. The mass of electron is much less than nuclei. As a result of this, the velocity of electron is much larger than that of nuclei. Born and Oppenheimer (1927) recommend a scheme that considers heavy nuclei as more or less fixed [6]. In general, the Hamiltonian of the system will depend upon nuclear coordinates, R_μ , and upon all electronic coordinates, r_i . For a system of n electrons under the field of N nuclei with charge Z_μ , Schrödinger equation is given as for such system;

$$(T_I + V_{II} + V_{el} + T_e + V_{ee})\psi(R_\mu, r_i) = E\psi(R_\mu, r_i). \quad (2.1)$$

where, T_I , V_{II} , V_{el} , T_e , V_{ee} is the kinetic energy of the nuclei, the Coulomb repulsion between nuclei, the Coulomb interaction between nuclei and electrons, the kinetic energy of electrons, and the Coulomb repulsion between electrons, respectively.

$$\begin{aligned}
T_I &= -\frac{\hbar^2}{2M_\mu} \sum_{\mu=1}^N \nabla_\mu^2, \\
T_e &= -\frac{\hbar^2}{2M_\mu} \sum_{i=1}^n \nabla_i^2, \\
V_{II} &= \frac{e^2}{2} \sum_{\mu \neq \nu}^n \frac{Z_\mu Z_\nu}{|R_\mu - R_\nu|}, \\
V_{ee} &= \frac{e^2}{2} \sum_{i \neq j}^N \frac{1}{|r_i - r_j|}, \\
V_{el} &= -e^2 \sum_{\mu=1}^N \sum_{i=1}^n \frac{Z_\mu}{|R_\mu - r_i|}.
\end{aligned} \tag{2.2}$$

The problem is separated into two parts ; electronic problem at fixed nuclei and nuclear problem under an effective potential which produced by the electrons [49]. Born-Oppenheimer approximation gives good results for many cases, e.g. the calculation of nuclear vibration modes in solids and also is starting point for perturbation theory in electron-phonon interaction , which is the fundamental for understanding electrical transport in metals, certain metal-insulator transitions, and the BCS theory of superconductivity [14].

It is known that electron moves much faster than nuclei. It is supposed that at any time the electrons "follow" the nuclear motion, while nuclei at any time "see" an effective potential that is produced by the electrons. To express the what is neglected and perform such a procedure , It is supposed that the wave function has the form of a product between a nuclear and an electronic wave function

$$\psi(\mathbf{R}_\mu, \mathbf{r}_i) = \phi(\mathbf{R}_\mu) \psi_R^l(\mathbf{r}_i). \tag{2.3}$$

index l shows the electronic states. If the Eq. (2.3) is substituted in Eq. (2.1), one obtains the following equation;

$$(T_I + V_{II} + E_R^l) \phi(R_\mu) \psi_R^l(r_i) = E \phi(R_\mu) \psi_R^l(r_i), \tag{2.4}$$

If \mathbf{R} dependency of the electronic wave function in the kinetic term is neglected;

$$T_I(\phi(\mathbf{R}_\mu)\psi_R^l(r_i)) \simeq \psi_R^l(r_i)(T_I\phi(\mathbf{R}_\mu)). \quad (2.5)$$

Schrödinger equation for the nuclear coordinates alone is written as follows;

$$(T_I + V_{II} + E_R^l)\psi(R_\mu) = E\psi(R_\mu). \quad (2.6)$$

The term $E_R^l + V_{II}$ is described as effective interaction potential among the nuclei. The leading error in the approximate expression of Eq. (2.5) is the neglect of the term;

$$\sum_{\mu} \frac{\hbar^2}{M_{\mu}} (\nabla_{\mu}\phi(R_{\mu})(\nabla_{\mu}\psi_R^l(r_i))). \quad (2.7)$$

If it is required, it can be added as a perturbation to study non-adiabatic effects [14, 49]. Now, we are ready to discuss the separated electronic part of the problem. This certainly is a many-body problem including the particle-particle interaction which is still too difficult to solve. The Hartree-Fock approximation was proposed to solve many-electron problem in the beginning of the age of quantum mechanics by Hartree-Fock [6].

2.2 The Hartree-Fock Approximation

The electrons are considered as distinguishable particles in the Hartree approximation. But electrons are indistinguishable and obey the Pauli's exclusion principle. This means that Hartree approximation does not include the fact that electrons have antisymmetric wave functions [6]. The Hartree approximation is improved by including the Pauli's exclusion principle [50, 51]. It is done by proposing an anti-

symmetrized many-electron wave function in the form of a Slater determinant.

$$\begin{aligned}\phi_{HF}(x_1, x_2, \dots, x_n) &= \frac{1}{\sqrt{N!}} \begin{vmatrix} \varphi_1(1) & \varphi_2(1) & \cdots & \varphi_N(1) \\ \varphi_1(2) & \varphi_2(2) & \cdots & \varphi_N(2) \\ \vdots & \vdots & \ddots & \vdots \\ \varphi_1(N) & \varphi_2(N) & \cdots & \varphi_N(N) \end{vmatrix} \\ &= S D \varphi_1(1) \varphi_2(2) \dots \varphi_N(N).\end{aligned}\quad (2.8)$$

Where $\varphi_i(j)$ indicates the i th one-electron spin orbital. i.e. composed of spatial and spin components, and j shows the spatial and spin coordinates of electron j condensed in a single variable $\mathbf{x}_j = (r_i, \sigma_j)$ [6]. It is known that the wave function alters sign when exchanging the coordinates of two of the electrons [50, 51]. This approximation is Hartree-Fock (HF) and used to calculating electronic structure of molecular system [6].

HF method was first applied to atoms in 1930 by Fock [50]. The total energy with respect to all degrees of freedom in the wave function is minimized in the HF approach with the restriction that it has the form Eq. (2.8). The HF equation can be solved in special cases such as spherical symmetric atoms and the homogeneous electron gas [6, 14].

It is assumed that a system of N free electrons in a volume V with homogeneous density $n = N/V$, with a neutralizing background of positive charge. If r_s is defined via the average volume per electron:

$$\frac{4\pi}{3} r_s^3 = \frac{V}{N} \rightarrow r_s = \left(\frac{3}{4\pi n}\right)^{\frac{1}{3}}. \quad (2.9)$$

The simplest approximation is to suppose the independent electrons. The solutions gives the plane waves with wavevector k :

$$\psi_k(\mathbf{r}) = \frac{1}{\sqrt{V}} \exp(i\mathbf{k}\mathbf{r}). \quad (2.10)$$

The box of volume V is restricted by the periodic boundary condition. The states are

completed up to a the sphere of radius k_F at zero temperature. The number of states are identical the volume of the sphere of radius k_F divided by the density of k states, that is, $8\pi^3/V$:

$$N = 2 \frac{4\pi}{3} k_F^3 \frac{V}{8\pi^3}, \quad (2.11)$$

That is

$$k_F = (3\pi^2 n)^{\frac{1}{3}} = \left(\frac{9\pi}{4}\right)^{\frac{1}{3}} \frac{1}{r_s}, \quad (2.12)$$

and the Fermi energy:

$$\varepsilon_F = \frac{\hbar^2 k_F^2}{2m} = \frac{\hbar^2}{2m} \left(\frac{9\pi}{4}\right)^{\frac{2}{3}} \frac{1}{r_s^2}. \quad (2.13)$$

The energy is only kinetic:

$$E = 2 \sum_{\mathbf{k}, k \leq k_F} \frac{\hbar^2 k^2}{2m} = 2 \frac{V}{8\pi^3} \int_{k \leq k_F} \frac{\hbar^2 k^2}{2m} dk, \quad (2.14)$$

yielding

$$E = N \frac{3}{5} \frac{\hbar^2 k_F^2}{2m}. \quad (2.15)$$

The electron gas is solved by using the HF approximation. The external potential term, coming from the neutralizing background taken into account in the Hartree potential term.

$$-\frac{\hbar^2}{2m} \nabla^2 \psi_k(\mathbf{r}) - \sum_{k'} \int \psi_{k'}(\mathbf{r}) \psi_{k'}^*(\mathbf{r}') \frac{e^2}{|\mathbf{r} - \mathbf{r}'|} \psi_k(\mathbf{r}') d\mathbf{r}' = E \psi_k(\mathbf{r}). \quad (2.16)$$

The plane waves solution Eq. (2.10) is used to solve HF equation for independent electrons. The exchange term can be rewritten as bellows,

$$(V_x \psi_k)(\mathbf{r}) = -\psi_k(\mathbf{r}) \frac{1}{V} \sum_{k', k' < k_F} \frac{4\pi e^2}{|\mathbf{k} - \mathbf{k}'|^2}, \quad (2.17)$$

If the sum is done,

$$(V_x \psi_k)(\mathbf{r}) = -\frac{2e^2 k_F}{\pi} F\left(\frac{k}{k_F}\right) \psi_k(r), \quad (2.18)$$

where

$$F(x) = \frac{1}{2} + \frac{1-x^2}{4x} \log \left| \frac{1+x}{1-x} \right|. \quad (2.19)$$

The energy eigen values is obtained as follows [49]

$$\varepsilon(\mathbf{k}) = \frac{\hbar^2 k^2}{2m} - \frac{2e^2 k_F}{\pi} F\left(\frac{k}{k_F}\right). \quad (2.20)$$

The derivative of $\varepsilon(\mathbf{k})$ gives unphysical logarithmic divergence at $k = k_F$. This gives rise to vanishing density of states at $\varepsilon \sim \varepsilon_F$. Because of this reason, HF approximation does not give good results for the homogenous electron gas. However, if there is a finite gap (i.e. in an insulator), HF gives good results [6, 49, 14]. It is possible to obtain the total energy by summing the eigenvalues in Eq. (2.20). One half of the exchange term is taken to prevent double summation

$$E = \sum_{k, k \leq k_F} \left[\frac{\hbar^2 k^2}{2m} - \frac{e^2 k_F}{\pi} F\left(\frac{k}{k_F}\right) \right]. \quad (2.21)$$

The first term gives rise to the noninteracting term, Eq. (2.14). If the second term can be obtained analytically, energy is obtained as;

$$E = N \left[\frac{3}{5} \frac{\hbar^2 k_F^2}{2m} - \frac{3}{4} \frac{e^2 k_F}{\pi} \right]. \quad (2.22)$$

The energy can be written as follows by substituting r_s in atomic units(Bohr radii)

$$\frac{E}{N} = \frac{2.21}{r_s^2} - \frac{0.916}{r_s} \text{ in Rydberg}. \quad (2.23)$$

where the first term corresponds to the kinetic energy and the second corresponds to the exchange energy. For typical values of r_s in metals ($r_s = 2/6$) the exchange energy makes an important contribution to the binding energy, while at high density (small r_s) the kinetic energy becomes effective [49].

The limitation of the HF approximation is that a single Slater determinant is not sufficient to represent the many-body wave function. There exists many other possible antisymmetric wave functions which can not be written in that way. The quality of description can be improved by several ways: i) combination of several Slater determinants can be used, ii) correlation perturbation above the HF solution is introduced, and iii) correlated wave functions can be used [6].

L.H. Thomas and E.Fermi proposed Thomas-Fermi theory at the same time as Hartree(1927-1928)

2.3 Thomas-Fermi Theory

In the Thomas-Fermi theory, the total energy is described by the local approximation for the (non-interacting) kinetic energy of a uniform gas which is described by explicit functional of density, plus Hartree energy [10, 14]. Both Thomas and Fermi did not take into account the exchange and correlation among the electrons; however, Dirac extend in 1930 [52]. This extension give rise to the energy functional for electrons in an external potential $V_{ext}(r)$ [14]. Energy is described as

$$E_\alpha[n] = \int n(\mathbf{r})\varepsilon_\alpha[n(\mathbf{r})]d\mathbf{r}. \quad (2.24)$$

where $\varepsilon_\alpha[n(\mathbf{r})]$ is the energy density of contribution α (kinetic, exchange and correlation). The local density approximation (LDA) was suggested for the first time.

For a homogenous electron gas, the electronic density is written in terms of the Fermi energy E_F

$$n = \frac{1}{3\pi^2} \left(\frac{2m}{\hbar^2} \right)^{\frac{3}{2}} E_F^{\frac{3}{2}}, \quad (2.25)$$

And the kinetic energy is ;

$$T = 3nE_F/5, \quad (2.26)$$

So that the kinetic energy density is ;

$$t(n) = \frac{3}{5} \frac{\hbar^2}{2m} (3\pi^2)^{2/3} n^{5/3}. \quad (2.27)$$

The LDA kinetic energy is given

$$T_{TF} = C_k \int n(\mathbf{r})^{5/3} d\mathbf{r}. \quad (2.28)$$

where $C_k = 3(3\pi^2)^{2/3}/10$ hartree. Exchange can be taken into account by considering Slater's expression for the homogenous electron gas [6, 52, 53].

$$E_x[n] = -C_x \int n(r)^{4/3} dr. \quad (2.29)$$

Where $C_x = 3(3\pi)^{1/3}/4 = (0.0739)$ hartree. If the exchange term is taken into account, the theory is called Thomas-Fermi-Dirac(TFD). Correlation can also be taken into account by using any local approximation to homogenous electron gas, for instance the one proposed by Wigner [54].

$$E_c[n] = -0.0056 \int \frac{n(\mathbf{r})^{4/3}}{0.0079 + n(\mathbf{r})^{1/3}} dr. \quad (2.30)$$

Where all the numerical constants are described in terms of atomic units. If the Eq. (2.30) is substituted into the total energy, TFD energy is obtained;

$$\begin{aligned} E_{TFD} = & C_k \int n(\mathbf{r})^{5/3} d\mathbf{r} + \int n(\mathbf{r}) V_{ext}(\mathbf{r}) d\mathbf{r} \\ & + \frac{1}{2} \int \int \frac{n(\mathbf{r})n(\mathbf{r}')}{|\mathbf{r} - \mathbf{r}'|} d\mathbf{r} d\mathbf{r}' - C_x \int n^{4/3} dr + E_c[n]. \end{aligned} \quad (2.31)$$

It is seen that TFD energy depends on electronic density [6]. It is possible to include the effect of inhomogeneity.

But, TFD approximation is rough and missing the fundamental physics and chemistry, such as shell structure of atoms and binding of molecules [55, 14]. However, TFD generated the basic principles of later development of the DFT [6, 14].

2.4 Basis of The Density Functional Theory

2.4.1 The Hohenberg-Kohn Theorem

DFT is based on two theorems. First theorem is proposed by Hohenberg and Kohn [46]. The approach of Hohenberg and Kohn is used to formulate the density functional theory as an exact theory of many-body systems and used for any system of interacting particles an external potential $V_{ext}(r)$ [14].

The first Hohenberg-Kohn theorem shows that the density can be used in place of the potential as the basic function describing the system. The potential, up to an arbitrary constant is determined by the ground-state density $n(r)$. In the original Hohenberg-Kohn paper, this theorem is confirmed for densities with nondegenerate ground states [10].

Theorem 1: External potential is established uniquely by the electronic density , in addition to additive constant.

Proof: Firstly, it is assumed that external potential is not uniquely determined by the density. In this case, it is expected to find two potentials V and V' such that their ground state density n is the same. Let ψ and $E_0 = \langle \psi | H | \psi \rangle$ be ground state wave function and ground state energy of the Hamiltonian $H = T + V_{ext} + U_{ee}$. Let also ψ' and $E'_0 = \langle \psi' | H' | \psi' \rangle$ be ground state wave function and ground state energy of the Hamiltonian $H' = T + V'_{ext} + U_{ee}$. According to Rayleigh-Ritz variational principle we have:

$$\begin{aligned}
E_0 < \langle \psi' | H' | \psi \rangle &= \langle \psi' | H' | \psi' \rangle + \langle \psi' | H - H' | \psi' \rangle \\
&= E'_0 + \int n(\mathbf{r}) [V_{ext}(\mathbf{r}) - V'_{ext}(\mathbf{r})] d\mathbf{r}.
\end{aligned} \tag{2.32}$$

Where, the fact that different Hamiltonians necessarily correspond to different ground states $\psi \neq \psi'$ is exchanged is used and is obtained:

$$\begin{aligned}
E'_0 < \langle \psi | H' | \psi \rangle &= \langle \psi | H' | \psi \rangle + \langle \psi | H' - H | \psi \rangle \\
&= E_0 - \int n(\mathbf{r}) [V_{ext}(\mathbf{r}) - V'_{ext}(\mathbf{r})] d\mathbf{r}.
\end{aligned} \tag{2.33}$$

Adding these two inequalities, gives $E_0 + E'_0 < E'_0 + E$, which is not possible. Therefore, It is not possible to obtain two different potential that corresponds to the same electronic density for the ground state, unless they differ by a trivial additive constant [6, 14]. External potential is established uniquely by density within constant.

Theorem 2: A universal functional for the energy $E[n]$ can be written in terms of density $n(\mathbf{r})$, valid for any external potential. For any particular $V_{ext}(\mathbf{r})$, the exact ground state energy of the system is defined as the global minimum value of this functional, and the exact ground state density $n_0(r)$ is defined as a density $n(r)$ which minimizes the functional.

The exact ground state energy and density are determined by the functional $E[n]$. All properties such as kinetic energy, are written in terms of $n(r)$ is specified, then,

$$\begin{aligned}
E_{HK}[n] &= T[n] + E_{int}[n] + \int d^3r V_{ext}(\mathbf{r}) n(\mathbf{r}) + E_{II} \\
&= F_{HK}[n] + \int d^3r V_{ext}(\mathbf{r}) n(\mathbf{r}) + E_{II},
\end{aligned} \tag{2.34}$$

Where E_{II} is the energy of the nuclei. $F_{HK}[n]$ is given,

$$F_{HK}[n] = T[n] + E_{int}[n]. \tag{2.35}$$

Now, If $n^{(1)}(\mathbf{r})$ is given as ground state density corresponding to external potential $V_{ext}^{(1)}(\mathbf{r})$. The Hohenberg-Kohn functional is identical to the expectation value of the Hamiltonian, which has the wave function $\psi^{(1)}$

$$E^{(1)} = E_{HK}[n^{(1)}] = \langle \psi^{(1)} | H^{(1)} | \psi^{(1)} \rangle. \quad (2.36)$$

If different density $n^{(2)}(\mathbf{r})$ which corresponds to a different wavefunction $\psi^{(2)}$. Then, the energy $E^{(2)}$ of this state is greater than $E^{(1)}$, because

$$E^{(1)} = E_{HK}[n^{(1)}] = \langle \psi^{(1)} | H^{(1)} | \psi^{(1)} \rangle < \langle \psi^{(2)} | H^{(1)} | \psi^{(2)} \rangle = E^{(2)}. \quad (2.37)$$

So, the energy described by Eq. (2.34) in terms of the Hohenberg-Kohn functional calculated for the correct ground state density $n_0(\mathbf{r})$ is smaller than the value of this expression for any other density $n(\mathbf{r})$.

If the functional $F_{HK}[n]$ was identified, then by minimizing the total energy of the system Eq. (2.34), with respect to variations in density function $n(\mathbf{r})$, the exact ground state density and energy would be expected to be found [14]. There exists some limitations. It is stated that the electronic density decides the external potential in this theorem. But, the density must correspond to some ground state antisymmetric wave function. While this condition is required condition for the true density, $n(\mathbf{r})$, it may not be suitable for other trial densities [6].

2.4.2 The Kohn-Sham Equation

Kohn-Sham (KS) recreate the problem of calculating the total electronic energy E as a functional of the electron density $n(r)$ [56]. The system of interacting electrons is described as an auxiliary system of non-interacting electrons. The ground-state charge density is defined as a sum over one-electron orbitals (the KS orbitals) for a system of non-interacting electrons $\psi_i(\mathbf{r})$

$$\left(-\frac{\hbar^2}{2m}\nabla^2 + V_{KS}(\mathbf{r})\right)\psi_i(\mathbf{r}) = \varepsilon_i\psi_i(\mathbf{r}). \quad (2.38)$$

obeying orthonormality constraints:

$$\int \psi_i^*(\mathbf{r})\psi_j(\mathbf{r})d\mathbf{r} = \delta_{ij}. \quad (2.39)$$

$V_{KS}(\mathbf{r})$ for a given $n(\mathbf{r})$ is defined. It is possible to solve this problem by applying the variational property of the energy [49]. Total energy is written

$$E[n] = \min_{\psi|n} \langle \psi | H | \psi \rangle. \quad (2.40)$$

The minimization of the functional $E[n]$ with respect to density gives the ground state of the many-electron Hamiltonian. Constraint is given as;

$$\int d^3r n(r) = N. \quad (2.41)$$

where N is the total number of electrons. If the Hamiltonian is separated into two terms: H_0 is the homogenous electron gas (with $V_{ext} = 0$), and the external potential:

$$H = H_0 + V_{ext}(\mathbf{r}), \quad (2.42)$$

If the Eq. (2.42) is substituted into equation Eq. (2.40);

$$E[n] = \min_{\psi|n} [\langle \psi | H_0 | \psi \rangle + \int d^3\mathbf{r} V_{ext}(\mathbf{r})n(\mathbf{r})]. \quad (2.43)$$

The term which is in square brackets is minimized for a given density, the second term becomes constant [57]

$$E[n] = F[n] + \int d^3r V_{ext}(\mathbf{r})n(\mathbf{r}), \quad (2.44)$$

where $F[n]$ is

$$F[n] = \min_{\psi|n} [\langle \psi | H_0 | \psi \rangle]. \quad (2.45)$$

To solve interacting electron problems, ground state energy for non interacting electrons can be solved, in the noninteracting case, $E[n]$ includes two terms; kinetic energy and the external potential $V_{ext}(\mathbf{r})$:

$$E[n] = T[n] + \int d^3(r)n(\mathbf{r})V_{ext}(\mathbf{r}). \quad (2.46)$$

Variation of E with respect to the density gives the following equation:

$$\frac{\delta T}{\delta n(\mathbf{r})} + V_{ext}(\mathbf{r}) = \lambda n(\mathbf{r}). \quad (2.47)$$

where λ is the Lagrange parameter related to the restriction of the density to yield the correct total number of electrons, N .

As seen in the above equations, $T[n]$ is taken as $F[n]$. The energy functional for a many-electron system with electronic interactions included can be written in the form [57].

$$E[n] = T[n] + E_H[n] + E_{xc}[n] + \int d\mathbf{r}n(\mathbf{r})V_{ext}(\mathbf{r}). \quad (2.48)$$

Where $T[n]$ is defined as follows;

$$T[n] = -\frac{\hbar^2}{2m}2 \sum_i \psi_i^* \nabla^2 \psi_i(\mathbf{r}). \quad (2.49)$$

The second term is the Hartree energy included the electrostatic interactions between clouds of charge:

$$E_H[n(\mathbf{r})] = \frac{e^2}{2} \int \frac{n(\mathbf{r})n(\mathbf{r}')}{|\mathbf{r} - \mathbf{r}'|} d\mathbf{r}d\mathbf{r}'. \quad (2.50)$$

Using the variational procedure;

$$\frac{\delta n(r)}{\delta \psi_i^*}(\mathbf{r}') = \psi_i(\mathbf{r})\delta(\mathbf{r} - \mathbf{r}'), \quad (2.51)$$

$$\frac{\delta T}{\delta \psi_i^*(\mathbf{r})} = -\frac{\hbar^2}{2m}2 \sum \nabla^2 \psi_i(\mathbf{r}), \quad (2.52)$$

$$\frac{\delta E_H}{\delta \psi_{\mathbf{r}}^*} = e^2 \int \frac{n(\mathbf{r}')}{|\mathbf{r} - \mathbf{r}'|} d\mathbf{r}' \psi_i(\mathbf{r}). \quad (2.53)$$

Finally; following equation is obtained;

$$\left(-\frac{\hbar^2}{2m}\right)\nabla^2 + V_H(\mathbf{r}) + V_{xc}(n) + V(\mathbf{r})\psi_i(\mathbf{r}) = \sum_j \lambda_{ij}\psi_j(\mathbf{r}). \quad (2.54)$$

The third term is the exchange-correlation term which includes all the remaining terms. Exchange correlation potential is defined as follows;

$$V_{xc}(n) = \frac{\delta E_{xc}}{\delta n(\mathbf{r})}. \quad (2.55)$$

The Lagrange multiplier λ_{ij} is found by multiplying both sides of equation Eq (2.54) by $\psi_k^*(\mathbf{r})$ and integrating:

$$\lambda_{ik} = \int \psi_k^*(\mathbf{r}) \left(-\frac{\hbar^2}{2m}\nabla^2 + V_H(\mathbf{r}) + V_{xc}(n) + V_{ext}(\mathbf{r})\right) \psi_i(\mathbf{r}) d\mathbf{r}. \quad (2.56)$$

Finally, KS equation is written as follows;

$$(H_{KS} - \varepsilon_i)\psi_i(\mathbf{r}) = 0. \quad (2.57)$$

where $\lambda_{ij} = \delta_{ij}\varepsilon_j$ and the operator H_{KS} , called KS Hamiltonian is described as;

$$H_{KS} = -\frac{\hbar^2}{2m}\nabla^2 + V_H(\mathbf{r}) + V_{xc}(\mathbf{r}) + V(\mathbf{r}) = -\frac{\hbar^2}{2m}\nabla^2 + V_{KS}(\mathbf{r}). \quad (2.58)$$

and is related to the functional derivative of the energy [49]:

$$\frac{\delta E}{\delta \psi_i^*}(\mathbf{r}) = H_{KS}(\mathbf{r}). \quad (2.59)$$

Solution of the KS equation is summarized in the Fig. 2.1.

To determine the Energy cut off parameters is important before performing calculation. The wave function in a periodic potential can be expanded in a plane-wave basis set. The \mathbf{G} vectors allowed in the plane wave (PW) expansion are identified as the reciprocal lattice vectors. An infinite number of such vectors is needed to describe

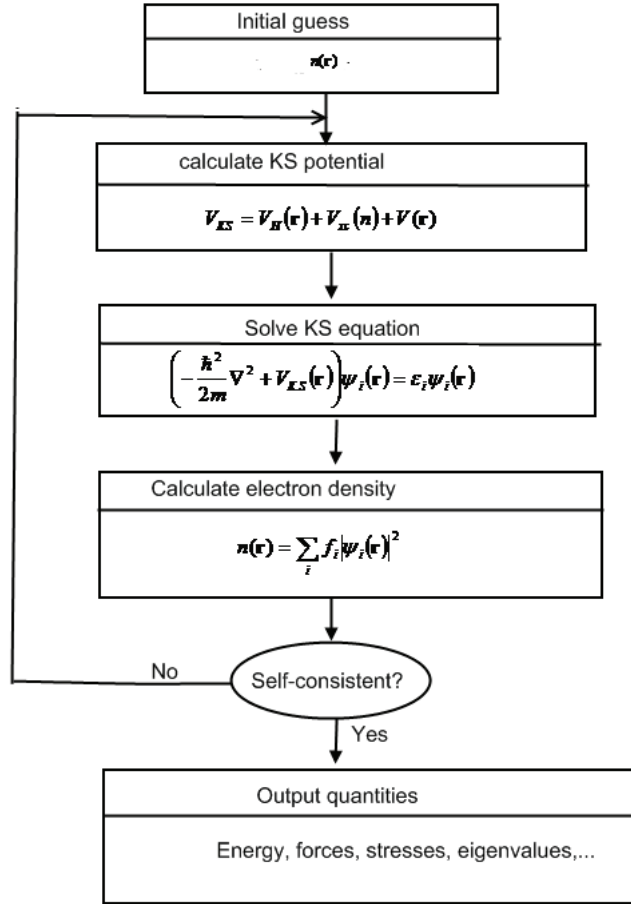


Figure 2.1: KS-chart [6, 14]

the wave functions with high accuracy. On the other hand, the Fourier coefficients $C_k(\mathbf{G})$ of the wave functions decrease with increasing $|\mathbf{k} + \mathbf{G}|$, so that the PW expansion can be shortened at a finite number of terms, i.e. restricted to all waves with kinetic energy lower than some energy cutoff E_{cut} [6]:

$$\frac{\hbar^2}{2m}|\mathbf{k}^2 + \mathbf{G}^2| < E_{cut}. \quad (2.60)$$

Generally, two typical approximations are widely used, which are Local density(LDA) and generalized gradient (GGA)approximations, for describing the electron distribution.

2.4.3 Local Density Approximation (LDA)

KS and HF equations are derived from a variational principle and are also self-consistent equations for one-electron wavefunctions. The only difference between KS and HF equations is the form of the exchange-correlation.

The local approximation describes the inhomogeneous system as a special case of uniform electronic system [6, 10]. This approximation uses the exchange -correlation hole corresponding to the homogenous electron gas. The energy terms local in density are obtained by integrating the energy density calculated at the values assumed by the electronic density $n(r)$ [6].

Exchange-correlation energy is not accurately predicted. Kohn and Sham proposed, the Local Density Approximation (LDA): the functional is approximated the functional by a function of the local density $n(r)$. The exchange correlation potential is a functional derivative of the exchange correlation energy with respect to the local density and this depends on the value of the electron density for a homogenous electron gas.

$$E_{xc}[n(\mathbf{r})] = \int \varepsilon_{xc}(n(\mathbf{r}))n(\mathbf{r})d\mathbf{r},$$

$$\frac{\delta E_{xc}}{\delta n(\mathbf{r})} = \mu_{xc}[n(\mathbf{r})] = (\varepsilon_{xc}(n) + n \frac{d\varepsilon_{xc}(n)}{dn})_{n=n(\mathbf{r})}. \quad (2.61)$$

Ceperley and Alder found accurate results from Quantum Monte-Carlo techniques and Perdew and Zunger parametrized it with a simple form

$$\begin{aligned} \varepsilon_{xc}(n) &= -0.9164/r_b - 0.2846/(1 + 1.0529 \sqrt{r_b} + 0.3334r_s), r_b \geq 1 \\ &= -0.9164/r_b - 0.00960 + 0.00622 \ln r_b - 0.0232r_s \\ &+ 0.0040r_b \ln r_b, r_b \leq 1. \end{aligned} \quad (2.62)$$

Where r_b is the Bohr radii and ε_{xc} is given in Ry. The first term gives the HF exchange contribution in Eq.(1.26). The remaining terms give the correlation energy [49, 57];

The main limitations LDA are; i) Inhomogeneities in the density are not included. ii) the LDA exchange- correlation term does not ignore completely the self-interaction present in the Hartree term. iii) non-local exchange and correlation effect are not taken into account; iv) strong local correlation effects cannot be recreated because of the correlation functional [6]. The generalize gradient approximation (GGA) may be used to overcome this limitation. LDA may not be enough to describe some systems. GGA may overcome this limitation for many systems.

2.4.4 Generalized Gradient Approximation (GGA)

To solve the issue of inhomogeneities in the electronic density, an expansion of the density in terms of the gradient and higher order derivatives is carried out [6]. In general, the exchange-correlation energy can be defined in the following form:

$$E_{xc}[n] = \int n(\mathbf{r})\varepsilon_{xc}[n(\mathbf{r})]d\mathbf{r} = \int n(\mathbf{r})\varepsilon_{xc}[n(\mathbf{r})]F_{xc}[n(\mathbf{r}), \nabla n(\mathbf{r}), \nabla^2 n(\mathbf{r}), \dots]d\mathbf{r}. \quad (2.63)$$

Where the function F_{xc} is an enhancement factor which modifies the LDA expression. The second order gradient expansion equals to an expression of the type

$$E_{xc}[n] = \int A_{xc}[n]n(\mathbf{r}^{4/3})d\mathbf{r} + \int C_x[n]|\nabla n(\mathbf{r})|^2/n(\mathbf{r})^{4/3}d\mathbf{r}. \quad (2.64)$$

this equation is asymptotically valid for densities that vary slowly in space [6]. Isotropy condition is taken into account, in addition, to exchange and the correlation hole satisfy their respective normalization conditions. This scheme has been introduced by several groups and some well known functional are those of Perdew and Wang 1986 [58, 59] and 1991 [60] (respectively PW86 and PW91) and of Becke [61], Lee, Yang and Parr [62] (LYP) and Perdew, Burke and Enzerhof [63, 64]. These exchange correlation functional go by the name of generalized gradient approximations (GGAs). A number of modified gradient expansion have been offered between 1986 and 1996 [6, 57].

2.4.4.1 Langreth-Mehl Functional

Langreth and Mehl (1981) offered the first GGA and assumed the following form;

$$\varepsilon_{xc} = \varepsilon_{xc}^{LDA} - a \frac{|\delta n(\mathbf{r})|^2}{n(\mathbf{r})^{4/3}} \left(\frac{7}{9} + 18f^2 \right) \quad (2.65)$$

$$\varepsilon_{xc} = \varepsilon_{xc}^{RPA} + a \frac{|\delta n(\mathbf{r})|^2}{n(\mathbf{r})^{4/3}} (2e^F + 18f_2). \quad (2.66)$$

where $F = b|\nabla n(\mathbf{r})|/n(\mathbf{r})^{7/6}$, $b = (9\pi)^{1/6}f$, $a = \pi/(16(3\pi^2)^{4/3})$ and $f = 0.15$ [6].

2.4.4.2 BLYP Functional

Becke [61] suggested an exchange functional where the parameters were fitted to experimental molecular data

$$\varepsilon_{xc} = \varepsilon_{xc}^{LDA} \left(1 - \frac{\beta}{2^{1/3}} A_x \frac{x^2}{1 + 6\beta x \sinh^{-1}(\mathbf{x})} \right). \quad (2.67)$$

For $x = 2(6\pi^2)^{1/3}s = 2^{1/3}|\nabla n(\mathbf{r})|/n(\mathbf{r})^{4/3}$, $A_x = (3/4)(3/\pi)^{1/3}$ and $\beta = 0.0042$

This was repaired by a correlation functional which is derived also in 1988 by Lee, Yang and Parr (LYP), thus, this is named BLYP functional [65].

$$\varepsilon_c = -\frac{a}{1 + dn^{-1/3}} \{ n + bn^{-2/3} [C_F n^{5/3} - 2t_w + \frac{1}{9}(t_w + \frac{1}{2}\nabla^2 n)e^{cn^{-1/3}}] \}. \quad (2.68)$$

where

$$t_w = \frac{1}{8} \left(\frac{|\nabla n|^2}{n} - \nabla^2 n \right). \quad (2.69)$$

$C_F = 3/10(3\pi^2)^{2/3}$, $a = 0.04918$, $b = 0.132$, $c = 0.2533$, $d = 0.349$. This correlation functional is not based on the LDA and has been obtained as an extension to other closed-shell systems of the Colle-Salvetti expression for the electronic correlation in helium [66, 6].

2.4.4.3 PBE Functional and Its Revisions

Perdew, Burke and Ernzerhof (PBE) [63] suggested an exchange and correlation functional that satisfies as many formal properties.

The enhancement factor $F_{xc}(n, \zeta, s)$ over the local exchange given in Eq.(2.63) depends on the local density n , magnetization density ζ (in the spin dependent case), and the dimensionless density gradient $s = |\nabla n(\mathbf{r})|/(2k_F n)$. The chosen expression is

$$F_x(s) = 1 + \kappa - \frac{\kappa}{1 + \mu s^2/\kappa}. \quad (2.70)$$

where $\mu = \beta(\pi^2/3) = 0.21951$ and $\beta = 0.066725$ is associated with the second order gradient expansion and also is the same for the exchange term [67]. PBE takes the the largest allowed value, $\kappa = 0.804$. The correlation energy is described as follows in an form similar to an earlier proposal of Perdew and Wang [68].

$$E_{xc}^{GGA} = \int n(\mathbf{r})[\varepsilon_{xc}^{LDA}(n, \zeta) + H[n, \zeta, t]]dr. \quad (2.71)$$

with

$$H[n, \zeta, t] = (e^2/a_0)\gamma\phi^3 \ln\{1 + \frac{\beta}{\gamma}t^2[\frac{1 + At^2}{1 + At_2 + A_2t^4}]\}. \quad (2.72)$$

Here, $t = |\nabla n(\mathbf{r})|/(2\phi k_s n)$ is a dimensionless density gradient, with k_s the Thomas-Fermi screening wave number, and $\phi(\zeta) = [(1 + \zeta)^{2/3} + (1 - \zeta)^{2/3}]/2$ is a spin-scaling factor. The γ is defined as; $\gamma = (1 - \ln 2)/\pi^2 = 0.031091$. The function A is described as the following form [6];

$$A = \frac{\beta}{\gamma}[\exp(-\varepsilon_{xc}^{LDA}n/(\gamma\phi^3 e^2/a_0) - 1)]^{-1}. \quad (2.73)$$

Before investigating electronic propertied of any system, pseudopotential is needed. So it is very important. We give description of pseudopotential and mentioned about ultrasoft and norm conserving pseudopotentials.

2.4.5 Pseudopotentials

Pseudopotentials (PP's) have been of great importance in solid state physics and used since 1960. In earlier approaches PP's were developed to reproduce some known experimental solid-state or atomic properties such as energy gaps or ionization potentials [49].

The basic description of pseudopotential figure is given in Fig.2.2 [219].

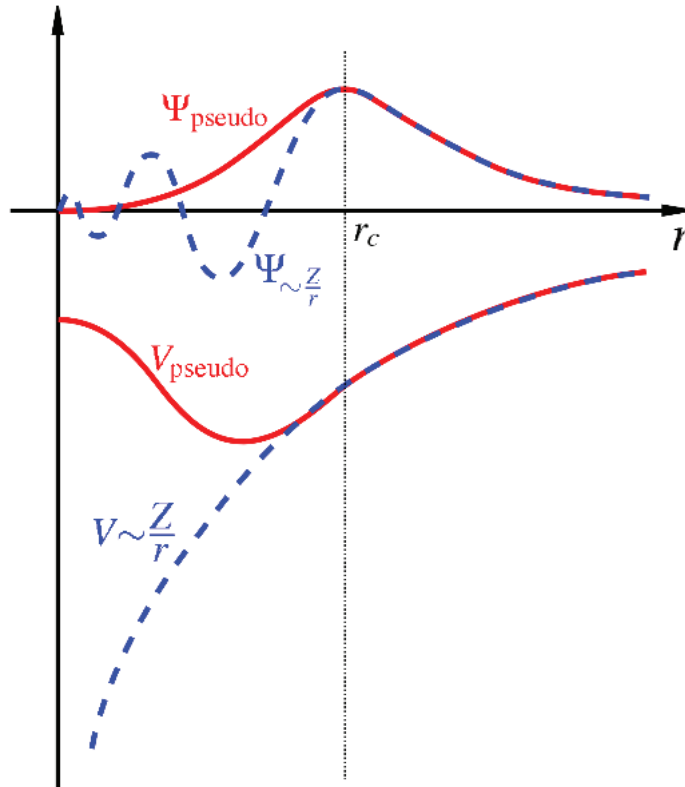


Figure 2.2: The real and the pseudo wavefunction and potentials match above a certain cutoff radius r_c [219]

It is known that the wave function for free electrons in a periodic crystal can be written in terms of plane waves (Pw's). If the potential due to the atoms is not taken into account, then PW's gives the exact solution. In the case that, the potential is smooth, it can be considered as a perturbation. On the other hand, the potential originated in the atomic nuclei is away from being the smooth. For heavier atoms the wave functions associated with the core states have a big peak. Therefore, a PW expansion of

the wave function in a real crystal may not be enough since the number of PW components which are needed to show such steep wave functions is huge. Slater (1937) proposed a possible solution to the atomic problem in spherical regions around the atoms, and the potential was assumed to be spherically symmetric inside the spheres, and zero outside (APW). Herring (1940) suggested an alternative method including of constructing the valence wave function as a linear combination of PW and core wave functions. This method is called as OPW (orthogonalized PW). By choosing appropriately the coefficient of the expansion, this wave function becomes orthogonal to the core states. As a result of this, a smaller number of PW components is needed to reproduce the valence states. Beyond the OPW approach, core states are reduced altogether by replacing their action with an effective potential, or a pseudopotential [6].

Core states do not allow to the use of PW's [49]. The basic idea of a pseudopotential is based on the using the instead of one problem with another. The fundamental application in electronic structure is that an effective ionic potential acting on the valence electron is to be used instead of the strong Coulomb potential of the nucleus and the effects of tightly bound core electrons. A pseudopotential can be produced in an atomic calculation and then used to calculate properties of valence electrons in molecules or solids [14]. Since the core electrons do not take part in chemical binding, it is possible to eliminate changes in core states (frozen core approximation). Only outer (valence) electrons contribute to chemical binding, while core electrons are "frozen" in their atomic state [6, 49]. However, Janak shows that large variations in the energy of core states can be produced by changes in the chemical environment. The problem was solved in 1980 by Von Barth and Gelatt. Their arguments are briefly summarized in here. n_c and n_v are the true selfconsistent core and valence charge; n_c^0 and n_v^* are the frozen-core charge and the corresponding valence charge. The frozen core error is given as ;

$$\delta = E[n_c^0, n_v^*] - E[n_c, n_v], \quad (2.74)$$

where $E[n_c, n_v]$ is the frozen-core functional. By expanding n_c and n_v ;

$$\delta \simeq \int \frac{\delta E}{\delta n_c} (n_c^0 - n_c) d\mathbf{r} + \int \frac{\delta E}{\delta n_c} (n_v^* - n_c) d\mathbf{r} + 2nd \text{ order terms.} \quad (2.75)$$

The important point is that the following stationary condition is kept

$$\frac{\delta E}{\delta n_c} = \mu_c, \frac{\delta E}{\delta n_v} = \mu_v. \quad (2.76)$$

where μ_c and μ_v are constants, since the first-order terms in the error vanish [49].

Modern PP's are named norm-conserving. The concept of 'norm-conservation' has great importance in the development of ab -initio pseudopotentials and it makes them more precise and transferable. Norm -conserving pseudofunctions $\psi_i^{PS}(\mathbf{r})$ are normalized and are solutions of model potential which selected to reproduce the valance properties of an all electron calculation. There exists several applications of the pseudo potential method to complex systems, such as clusters, molecules, solids, etc., the valance pseudofunctions satisfy the orthonormality conditions.

$$\langle \psi_i^{\sigma, PS} | \psi_j^{\sigma', PS} \rangle = \delta_{i,j} \delta_{\sigma, \sigma'}. \quad (2.77)$$

The norm -conserving potential must satisfy some condition which is given by Hamann, Schluter, and Chiang [70](HSC):

1. The eigenvalues of the pseudo-wave function are in agreement with those of the all -electron wavefunctions for a chosen electronic configuration of the atom.
2. All -electron and pseudo valance wavefunctions are identical outside a chosen core radius R_c .
3. The logarithmic derivatives of the all-electron and psedo wavefunctions approve at R_c .

The wavefunction $\psi_l(r)$ and its radial derivative $\psi'_l(r)$ have to be continuous at R_c for

any smooth potential. The dimensionless logarithmic derivative D is given by

$$D_l(\varepsilon, r) \equiv r\psi'_l(\varepsilon, r) = r\frac{d}{dr} \ln \psi_l(\varepsilon, r). \quad (2.78)$$

4. The integrated charge inside R_c for each wavefunction are identical (norm-conservation). It is known that the pseudopotential and radial pseudo-orbital ψ_l^{PS} differ from their all-electron counter parts inside the R_c . But, it is needed that the integrated charge,

$$Q_l = \int_0^{R_c} dr r^2 |\psi_l(r)|^2 = \int_0^{R_c} dr \phi_l(\mathbf{r})^2. \quad (2.79)$$

is the equivalent to ψ_l^{PS} (or ϕ_l^{PS}) as for the all electron radial orbital ψ_l (or ϕ_l) for a valence state.

5. The first derivative of the logarithmic derivatives of the all -electron and pseudo wavefunctions approve at R_c , and therefore for all $r \geq R_c$ [6, 14].

Norm-conserving PP's are still "hard" to use that is, they include a significant amount of Fourier components for a number of atoms and the first row of transition metals. More complex Ultrasoft PP's have been improved that are much softer than ordinary normconserving PP's, at the price of a considerable additional complexity [49].

2.4.5.1 Ultrasoft Pseudopotentials

The norm-conservation constraint is the main reason responsible for the hardness of some pseudopotentials, such as p states in first-row elements and d states in second-row transition metals, e.g. $O 2p$ or $Cu 3d$. There does not exist a core state of the same angular momentum to which they have to be orthogonal. Because of that reason, all-electron wave function becomes passive and quite compressed compared to the other valence states, thus needing a large number of PWs to be defined accurately. The main problem for the norm -conserving potential is that it has big PW cut off. The main advantage is that for ultrasoft pseudo potential, PW cut off is decreased [6]. Vanderbilt [71] improved to the norm conservation condition by relaxing the norm-conservation

condition and showed that much smoother, but it is still highly transferable.

The relativistic correction for heavy atoms is needed since the core electrons in the lower shells have high energy. Dirac's expression has to be used instead of the kinetic energy operator in Schrödinger equation [6].

We use the PWSCF and VASP package programs. The steps followed by the PWSCF program are described briefly in the following.

Firstly, to solve Kohn-Sham equations, initial guess for the electronic charge density is needed. In the second step, Hartree potential and exchange correlation potential are calculated. While Hartree potential is calculated by means of the Poisson equation, exchange-correlation is calculated by using various analytical calculations such as LDA and GGA. In this part of the calculation, one needs the pseudopotential for investigated atoms and the sample data for atoms in the crystal structure. One will also needs to provide the following input: i) atom name, atomic mass, pseudopotential name, ii) atomic position and number of k-points in the Irreducible Brillouin zone of the crystal k-points. In step III, the effective Kohn-Sham potential, V_{eff} , is constructed. The Hamiltonian matrices for each of the k points included in the calculation must be constructed by using plane waves and to be diagonalized to obtain the Kohn-Sham eigenstates. We then use the well-established techniques for iterative minimization by searching in the space solutions such as Conjugate gradient and another popular iterative diagonalization technique which is called Davidson algorithm. Resulting eigenstates will normally generate a different charge density from the one originally used to construct the electronic potentials, and hence a new set of Hamiltonian matrices must be constructed using the new electronic potential. The eigenstates of the new Hamiltonian is obtained, and the process is repeated until the solutions are self consistent. VASP package program follows similar steps.

If we want to calculate the band structure of any crystal system, we follow the following steps: In the first step of a band structure calculation, we need to do a self consistent calculation at a given energy cutoff and lattice parameter. Secondly, we calculate a non self-consistent calculation at the same energy cutoff and lattice pa-

parameter. We define the number of Kohn-Sham orbitals we want to compute and list of k-points. Finally, it is possible to plot the bands [49].

CHAPTER 3

LOW DIMENSIONAL SYSTEMS BASED ON CLUSTERS

Clusters consist of a few tens to a few thousands of atoms. A change in size is negligible for the properties of a macroscopic solid, but the properties of cluster is affected drastically. They show different physical and chemical properties from the bulk counterparts. Clusters, consisting of either metallic or covalent elements, have been investigated extensively since the 1980s and are even being considered as possible building blocks for new types of solids with the development the nanotechnology [5].

Transition metal clusters have great importance due to that the free atoms of the transition metals have an incomplete d shell in the ground state or in excited states of small energy. They show the most interesting properties of these elements as free atoms or in the metallic bulk phase due to these d electrons. The electronic configurations of Cu , Ag and Au have a closed d shell and a single s valence electron, so they show unique properties [72]. Small clusters are the active components of dispersed metal catalysis, because of their surface to volume ratio. Other application of metal clusters are that they are used as basic materials in photographic process. The special features of metal clusters, such as metal-insulator transition may be used in designing of novel sensors [73]. The transition metal clusters have great importance both theoretically and experimentally, since they can be used for hight density magnetic data storage. Pt clusters are used as catalysis automotive catalytic converters to reduce toxic pollutants, such as CO , NO_x , and hydrocarbons. It is also an important material for the heterogeneous catalysis of hydrogenation [74].

In this chapter, we investigate small metallic clusters, such as Pt , Cu , Ag and Au and

AuPt.

The electronic properties of *Cu* and *Pt* clusters are investigated by some research groups [73, 75, 76, 77, 78]. K.A.Jackson [75] investigated the structural and electronic properties of small ($n \leq 5$) *Cu* clusters using the first principles calculations based on the local -spin- density approximation, using an all electron, Gaussian orbital formalism. They observed that there is significant hybridization between the $3d$ and $4s$ in the cluster bonding states. This hybridization results in strong bond-length preference in the clusters. They find that the stable structures of neutral *Cu* clusters are the two dimensional (2D). H.Gröbeck and P.Broqvist [76] worked on octomer isomers of gold and compared with results for copper by using DFT. They observed that the stable isomers for gold stay two dimensional, while it is three dimensional for copper. They show that *Cu*₈ clusters are both two (2D) and three dimension (3D) and shows strong hybridization. There exists several research on *Pt* clusters [74, 79, 80]. L.Xio and L.Wang [74] investigated *Pt* clusters of up to 55 atoms using DFT with a plane wave basis set. They observe that planar *Pt* clusters up to nine atoms are as stable as their three-dimensional isomers and the six-atom planar cluster is more stable than its three-dimensional isomers. The structure and energetics of small *Pt* clusters are investigated by S.H.Yang and et al., [79] by using a method based on non-selfconsistent Harris functional version of LDA. The clusters are shown to be planar between $n = 4$ and $n = 6$. In our study, we obtain the stable structures of *Pt* and *Cu* clusters up to eight atom. We present the stable structures of them.

The electronic properties and atomic structures of gold and silver clusters have been theoretically investigated by several research groups [19, 81, 82, 83, 84, 85, 86, 87, 88, 89, 90]. Koutecky and co-workers [81] investigated small neutral and anionic silver clusters, up to a monomer, using Hartree-Fock and correlated ab-initio method. Fournier studied the silver clusters using DFT (VWN), sum of square-roots of atomic coordinates (SSAC), and extended Hückel molecular orbital (EHMO) theory [82]. G. Bravo-Pérez et al., [83] investigated small *Au*_{*n*} where $n = 2 - 6$; clusters by using ab initio methods. H.M.Lee and co-workers [84] have investigated the structures of pure gold and silver clusters (*Au*_{*k*} and *Ag*_{*k*}, $k = 1 - 13$) and neutral and anionic gold-

silver binary clusters ($Au_mAg_n, 2 \leq k = m + n \leq 7$) by using the density functional theory with generalized gradient approximation (GGA) and ab initio calculations including coupled cluster theory with relativistic ab initio pseudo potentials. Wilson and Johnson [85] worked on neutral Au_8 clusters theoretically. It is predicted, using Murrell-Mottram model, that the lowest energy isomer is a D_{2d} dodecahedron, while Häkkinen and Landman [86] used the GGA DFT method with and RECP to predict a T_d capped tetrahedron. Different functionals with LDA/DFT/RECP is used by Wang, Wang and Zhao [87] to determine the stable structure of Au_8 clusters [88]. Recently, B.Yoon and co-workers [31] have studied catalytic properties of Au_8 cluster. They have investigated the charging effects on bonding and catalyzed oxidation of CO on Au_8 clusters on MgO . Although much of the experimental and theoretical work so far has been done on pure gold and silver clusters and nanoparticles [84], there exists less information about the normal modes. The only information available is that of experimental data on dimers [91, 89]. Therefore, the present work provides the much needed information on phonons. Before studying physical and electronic properties of Au and Ag clusters, we determine their stable structures [19].

Gold-platinum bimetallic nanoparticles on the other hand, are investigated for their role in CO adsorption and oxidation [92, 93, 94, 95, 96, 97], NO adsorption and reduction [98], CH_3OH oxidation [99, 100]. It is established that bimetallic systems are better catalysts than pure metal clusters [101, 102, 103, 104, 105]. This increase in catalytic activity is determined by controllable factors such as composition, temperature and the method of preparation.

A.Cruz et al [106] investigated H_2 adsorption on $AuPt_n$ clusters using ab initio multi-configuration self-consistent field calculations. They show that gold has an electronic effect which poisons Pt activity to dissociate H_2 .

A. M. Joshi et al. [94] studied CO adsorption on binary Au -alloys (Au_nM_m clusters: $n=0-3$, $m=0-3$, and $m+n=2$ (dimers) or 3 (trimers), $M = Cu/Ag/Pd/Pt$.) They observed that CO binds on Au_nM_m except Pd_2 , Pt_2 and Pt_3 .

Effect of adsorption site, size and composition of bimetallic Pt/Au bimetallic clus-

ters on the adsorbed CO frequency is studied by Sadek and Wang using the density functional theory (DFT) calculations [95].

H. Tada et al. [107] investigated experimentally the preparation of Au/Pt core/shell bimetallic clusters on TiO_2 surfaces. They also did calculations on the model clusters by using DFT to understand the surface bonding between the sulfur and metal clusters. They observe that the adsorption of sulfur-containing compounds on the substrate can be controlled and the adsorption energy changes with Pt/Au atomic ratio.

L. Wang [96] showed by a DFT calculation that CO adsorbs upside-down on small Pt_mAu_n clusters, $Pt(111)$, $Au(111)$, and $Pt_{0.25}Au_{0.75}(111)$ surfaces.

O.O.Neria et al. [108] studied H_2 adsorption on $AuPt_3$ by using Hartree-Fock self-consistent field calculations. They find that $AuPt_3$ cluster can capture and dissociate the H_2 molecule.

3.1 Computational Details

PWSCF package program [15] is used. We have used two different approximations: GGA and LDA. We determine the pseudopotential and tested it by comparing with the experimental data. We used ultrasoft pseudopotentials [63, 109] for Pt , Cu , Au , Ag and Pt . We include the spin polarize effect in our calculation for Pt clusters.

We tested the cutoff energy. A cutoff energy of 408 eV is used with the plane wave basis. We carry out our calculations in the supercell because of the lack of periodicity. The binding energy per atom (E_B) is calculated by using

$$E_B = E_{cluster}/N - E_{atom}. \quad (3.1)$$

where E_{atom} and $E_{cluster}$ denote the energy of a single atom and the total energy of an atom in the cluster respectively and N is the number of atoms in the cluster [19].

The equilibrium structure is found using Hellmann-Feynman forces. We calculate the

scanning tunnelling microscope (STM) images using the PWSCF package program [15] based on theory of J.Tersoff and D.R.Hamann [110]. We calculated the normal mode frequency using the Density Functional Perturbation Theory (DFPT)[111]. Harmonic frequencies and displacement patterns of normal modes on the electronic ground state are calculated from the diagonalization of the dynamical matrix. Vibrational and dielectric properties are calculated using the linear response theory [112, 113]. Displacements and frequencies of the normal vibrational modes at the Brillouin zone center are calculated in a harmonic approximation. They are the eigenvectors and square roots of the eigenvalues of the dynamical matrix, respectively. Calculations are performed in a zero macroscopic electric field. Thus, the derived displacements and frequencies are those of the transverse optical (TO) modes. In this study, we have calculated the normal modes of Au_n , Ag_n at the Γ point [19].

3.2 The Stable Configuration of Pt,Cu, Clusters

We obtain the stable structures of *Pt* and *Cu* clusters up to eight atom. The binding energies and bond lengths are given in Table. 3.1 for Pt_2 and Cu_2 . Our results are in agreement with the available experimental data [114, 74, 90, 115].

Table 3.1: The Bond length and binding energies of *Pt* and *Cu* clusters.

Atom/xc	Bond length(\AA)	Binding Energy(eV)
Cu/GGA	2.24	1.13
Cu/LDA	2.17	1.34
Cu/exp.	2.22	2.01
Pt/GGA	2.35	1.83
Pt/LDA	2.31	2.15
Pt/exp.	2.34	1.83

The stable structures and the binding energies are given in Fig. 3.1 for *Pt* and *Cu* clusters within GGA and LDA. We observe that GGA results are in agreement with that of LDA up to $n = 7$ for *Cu* clusters. It is seen in Fig. 3.1(a) that Cu_8 clusters have both 2D form and 3D form within GGA. We see that our results for *Cu* clusters are in agreement with literature [78, 90].

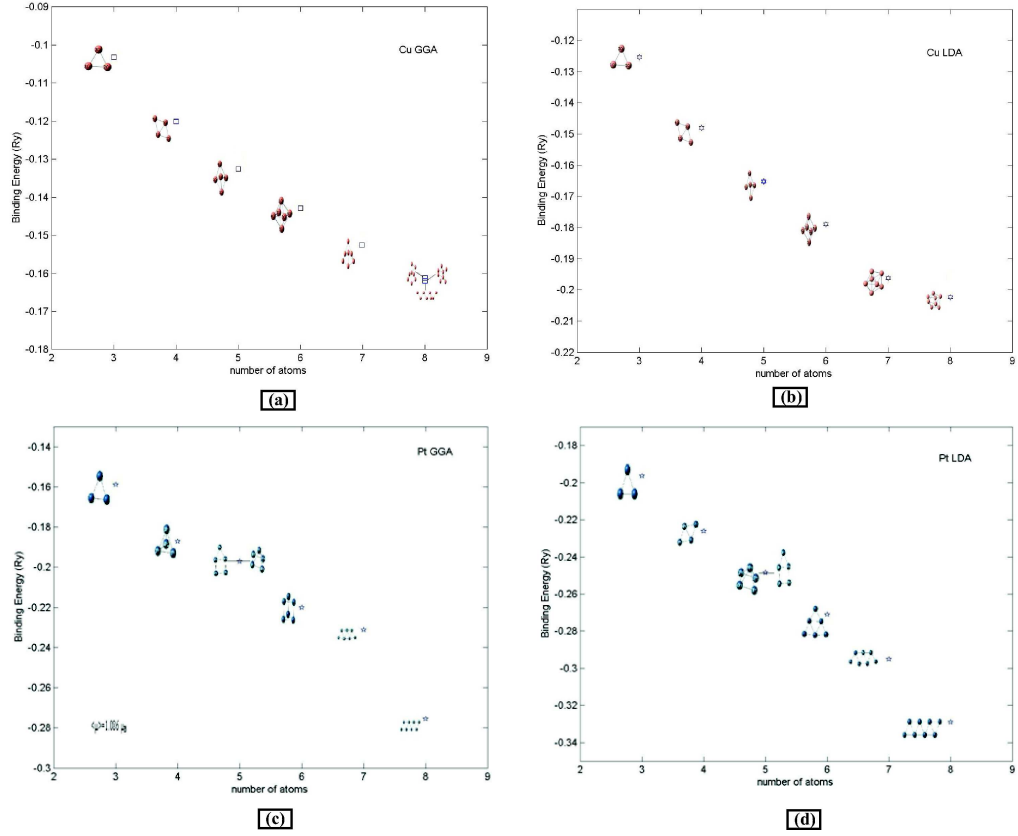


Figure 3.1: The stable structures of *Pt* and *Cu* clusters within GGA and LDA.

We obtain the binding energy and the stable structures of *Pt* clusters up to $n = 8$. We obtain the similar structure to that of LDA. *Pt* clusters have 2D and 3D structures like *Cu* clusters. On the other hand, Pt_7 and Pt_8 have 2D structure in both GGA and LDA. We see that while total magnetization is zero within LDA, it is $1.08 \mu_B/\text{cell}$ within GGA. We observe that our results are in agreement with the literature [74, 79].

3.3 Vibrational Modes and The Stable Configurations of Au Clusters

We tested the stability of our results [19] by comparing with the available experimental data. The available experimental data for Au_2 is given in Table. 3.2 [116, 117]. LDA results for the binding energy and bond length are closer to the experimental data than GGA results.

Table 3.2: The dimer length and binding energy of Au clusters [19].

Au_2	GGA	LDA	experimental
dimer(Å)	2.523	2.432	2.470
binding energy(eV)	2.244	2.954	2.290±0.008

The binding energy per atom shows that Au have planar structures.

The stable configurations of and Au clusters are shown in Fig.3.2 which were drawn by XCrySDEN (Crystalline Structures and Densities) program [118]. The cited works in the literature show that, generally, Au clusters have planar structures(2D). As seen in Fig. Fig.3.2(a), Au clusters favor planar structures within GGA. Au_3 shows a triangular structure. Au_4 favors a parallelepiped. But, Au_5 , Au_6 and Au_7 show two stable structures. Some structures are not symmetrical. Although we tried to test the stable configurations already reported in the literature [18, 119, 23, 86, 87, 120], the stable structures we find turned out to be different. These difference comes from using different methods. These differences are also due to the binding energy. We find that the binding energy of configurations in the literature are smaller than our stable configurations for Au and Ag clusters. Although, the stable configuration of Au_5 is in agreement with G. Bravo-Pérez et al., results [121], we obtain different frequencies from theirs. We also find that the stable configuration of Au_8 . Au_8 and Au_4 have similar shapes.

As seen in Fig.3.2 (b), Au clusters show planar structures with LDA. The same shapes are found with GGA up to four atoms. Au_5 , Au_6 and Au_7 show two stable structures as in GGA. But, Au_5 and Au_6 have different shapes than in GGA. Some structures are not symmetrical like the structures in GGA. Au_7 and Au_8 , show the same structures as in the GGA.

We have calculated the density of states(DOS) and partial density of states (PDOS) of the stable structure of Au for GGA and LDA. GGA result is in agreement with LDA. As an example, Au_8 for LDA is given in Fig.3.2(c). Fig.3.2(c) shows that sp orbital overlap near the Fermi surface in the highest occupied molecular orbital(HOMO) and

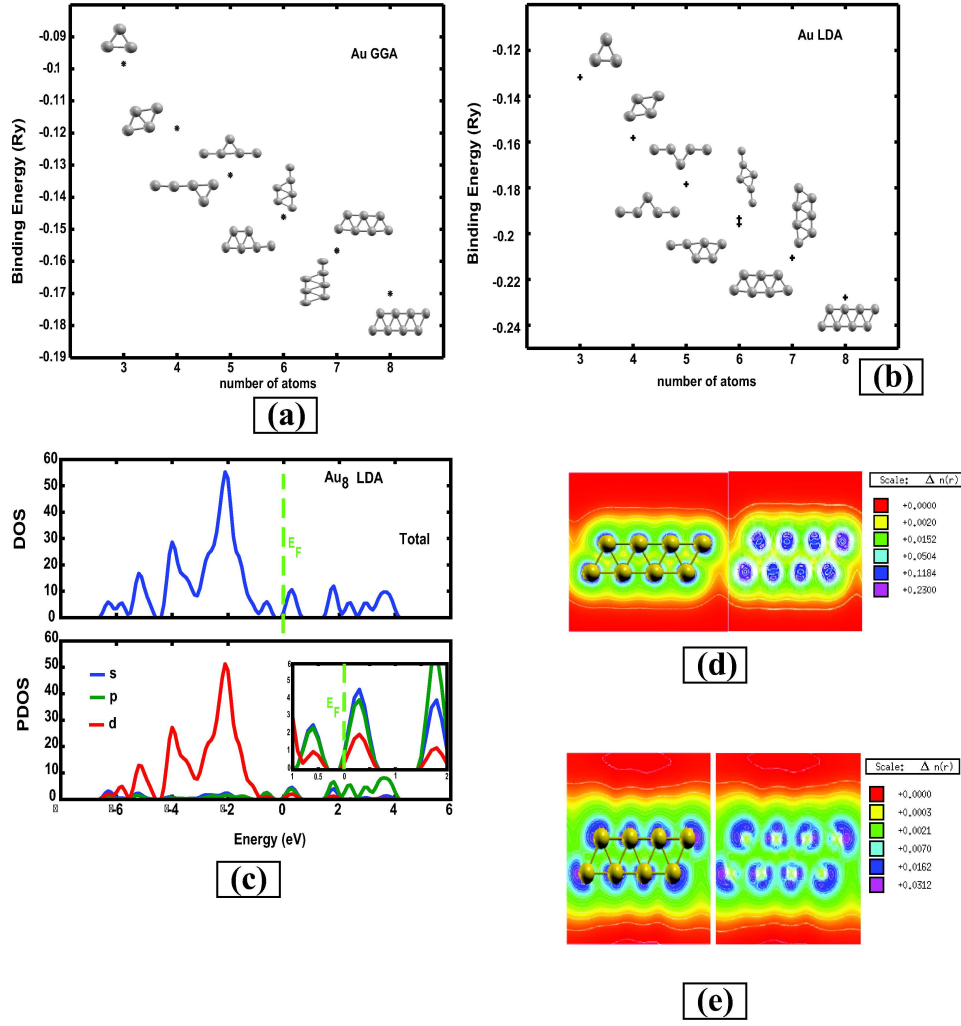


Figure 3.2: The stable structures of Au_n (a) within GGA and (b) LDA, (c) DOS and partial DOS of Au_8 LDA (d) STM image for HOMO of Au_8 GGA, (e) STM image for LUMO of Au_8 GGA [19].

lowest unoccupied molecular orbital(LUMO), This shows that there is s-p hybridization. The effects of d-orbitals are weak. It can be said that s-d hybridization in the LUMO is weaker than that in the HOMO [19]. It is known that the major contribution to the weak s-d hybridization in the non-relativistic calculations, comes from the s orbital[19, 122].

Here, we present for the first time, the STM images for small clusters investigated in this work. STM images are important for investigation of adsorption of molecules on surfaces. Bonding properties and hybridization can be clearly seen in STM im-

ages. We calculated the STM images at constant current and positive and negative bias voltage of 2.45 and -2.45 eV respectively for Au_8 in GGA and LDA.

STM images of Au_8 within LDA are in agreement with GGA. As an example, STM image of Au_8 for HOMO GGA is given in Fig.3.2(d). As seen in the figure, the charge density between atoms is bigger, which results in covalent bonds. The left side of Fig.3.2(d) shows the density in more detail. s-p hybridization is seen in the leftmost bottom atom and the rightmost top atom and also in the atoms at the middle. The strongest binding is in the rightmost bottom and the leftmost top atoms as seen in the charge distribution. Fig.3.2 (e) shows that s- p^2 hybridization occurs between the atoms at the middle in the LUMO. s-p hybridization is seen also in the top and bottom atoms, where the binding is stronger [19].

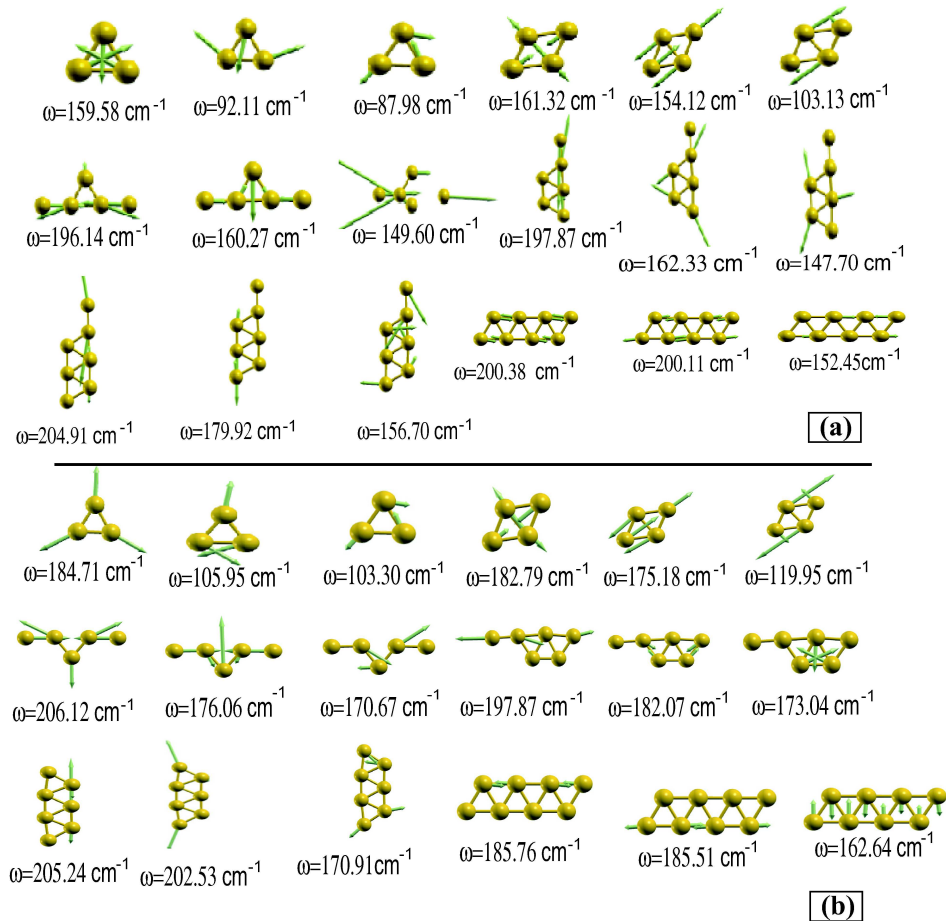


Figure 3.3: Vibration modes of stable configuration of Au_n clusters obtained by using (a) GGA and (b) LDA [19].

Table 3.3: The normal mode frequency of Au_2 [19].

Au2	GGA	LDA	experimental
$\omega(cm^{-1})$	172.99	204.92	191.00

We have also calculated the modes of vibrations of modes of Au for GGA and LDA and these are given Fig.3.3. We give only three highest frequency.

We compare the normal modes of Au_2 with available experimental data in Table.3.3 [91, 89]. The normal mode frequencies of Au_2 with the LDA is closer to the experimental data than with the GGA result. We see that our results are in agreement with the experimental data.

As seen in the Fig.3.3 (a), for GGA, $\omega = 159.58 \text{ cm}^{-1}$ shows the symmetric stretching in Au_3 , the other two frequencies correspond to the antisymmetric stretching. In Au_4 , all frequencies correspond to antisymmetric stretching modes. In Au_5 , $\omega = 196.14 \text{ cm}^{-1}$ shows the combination of scissor and antisymmetric stretching. This frequency is smaller than that in the literature [83]. Other frequencies correspond to antisymmetric stretching. In Au_6 , $\omega = 147.70 \text{ cm}^{-1}$ is for the symmetric stretching, others correspond to the antisymmetric stretching. In Au_7 , $\omega = 179.92 \text{ cm}^{-1}$ is for scissor stretching, all of the other frequencies correspond to antisymmetric stretching. In Au_8 , $\omega = 200.38 \text{ cm}^{-1}$ and $\omega = 200.11 \text{ cm}^{-1}$ correspond to the scissor stretching. As seen in Fig.3.3, all frequencies for Au_4 correspond to the similar modes in both LDA and GGA. While $\omega = 185.76 \text{ cm}^{-1}$, $\omega = 185.51 \text{ cm}^{-1}$ in the Au_8 , $\omega = 182.07 \text{ cm}^{-1}$ in the Au_6 correspond to the scissor stretching, $\omega = 185.51 \text{ cm}^{-1}$ in the Au_8 is for the combination of scissor and symmetric stretching. As $\omega = 184.71 \text{ cm}^{-1}$ in Au_3 and $\omega = 173.04 \text{ cm}^{-1}$ in Au_6 are for the symmetric stretching, others correspond to the antisymmetric stretching [19].

3.4 Vibrational Modes and The Stable Configurations of Ag Clusters

The binding energy per atom shows that Ag clusters have planer structures like Au cluster.

The stable configurations of Ag are shown in Fig.3.4(a) and (b) within GGA and LDA [19]. The cited works in the literature show that, generally, Au clusters have planar structures(2D), while Ag clusters have both 2D and 3D structures.

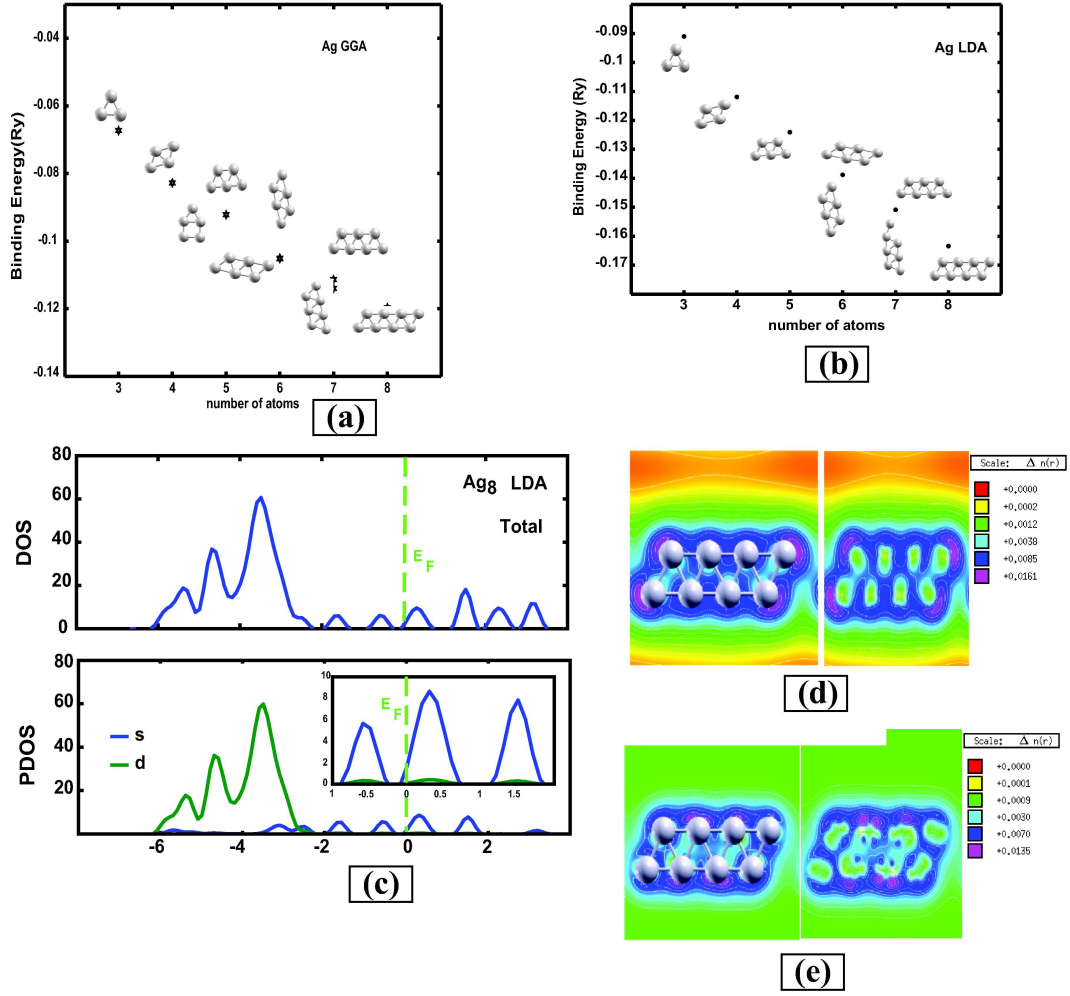


Figure 3.4: The stable structures of Ag_n (a) within GGA and (b) LDA, (c) DOS and partial DOS of Ag_8 LDA (d) STM image for LUMO of Ag_8 GGA, (e) STM image for HOMO of Ag_8 GGA [19].

As seen in Table. 3.4, our results [19] are in general agreement with the experimental data [89, 123]. Fig.3.4 shows that Ag_3 has triangular structure although we begin

with an initially open angle configuration. For Ag_4 , a parallelepiped is the most stable configuration. Ag_5 has two stable configurations [19]. In addition to the shape of Ag_4 , there exists another configuration which is different from that in the literature [18, 20, 21, 122]. Ag_6 , Ag_7 show similar structures to Ag_5 . Ag_8 is like Ag_4 but different from that in the literature [18, 20, 21]. They found that Ag clusters undergo a 2D to 3D geometry transition from Ag_6 to Ag_7 . We do not observe this transition. This may come from using different pseudopotential and wave function basis set. The shapes of the Ag_7 and Ag_8 are similar to Au_7 and Au_8 , respectively. The GGA structures for Ag_3 , Ag_4 , Ag_6 , Ag_7 and Ag_8 are similar to that with LDA as shown in Fig.3.2. But for Ag_5 , we find only one stable structure with LDA.

We have calculated the DOS and PDOS of Ag clusters for GGA and LDA. As an example, Ag_8 is given in Fig.3.4 (c) for LDA. GGA PDOS and DOS are similar to that in LDA. The major contribution comes from the s orbital in both HOMO and LUMO. While s-d hybridization in the HOMO is strong, it is weak in the LUMO.

We have calculated STM images of Ag_8 for GGA and LDA. LDA results are in agreement with GGA. As an example, STM images of Ag_8 in GGA are given in Fig.3.4(d) and (e). charge distribution between atoms is denser, as in Au_8 . In the HOMO and LUMO the s orbital is more effective than d orbital. Binding in the top and bottom atoms is stronger.

We have also calculated the modes of vibrations of Ag for GGA and LDA and these are given Fig.3.5(a) and (b). We give only three highest frequency.

We compare the normal modes of Ag_2 with available experimental data in Table.3.5 [89, 91]. The normal mode frequencies of Ag_2 with the LDA is closer to the experimental data than with the GGA result. We see that our results [19] are in agreement with the experimental data.

R. Fournier [82] calculated the normal mode of some stable configurations of Ag clusters. Fournier found that there is a noticeable jump in the largest frequency from $N=6$ to $N=7$ clearly due to the change from planar to 3D structure. We do not observe

Table 3.4: The dimer length and binding energy of Ag clusters [19].

Ag_2	GGA	LDA	experimental
dimer(\AA)	2.589	2.174	2.53
binding energy(eV)	0.850	1.070	0.83

Table 3.5: The normal mode frequency of Ag_2 [19].

Ag_2	GGA	LDA	experimental
$\omega(cm^{-1})$	138.65	202.49	192.4

this transition.

The vibrational normal modes of Ag are given in the Fig.3.5 (a) for GGA, while $\omega = 155.76 \text{ cm}^{-1}$ in the Ag_7 correspond to the scissor stretching, $\omega = 227.63 \text{ cm}^{-1}$ and $\omega = 203.72 \text{ cm}^{-1}$ in Ag_8 are for the combination of symmetric stretching and scissor stretching. While $\omega = 156.58 \text{ cm}^{-1}$ in the Ag_3 correspond to the symmetric stretching, the others correspond to the antisymmetric stretching.

The vibrational normal modes of Ag are given in Fig.3.5(b) for LDA, $\omega = 202.22 \text{ cm}^{-1}$ in the Ag_4 , $\omega = 197.95 \text{ cm}^{-1}$ in the Ag_6 , $\omega = 215.77 \text{ cm}^{-1}$ and $\omega = 213.99 \text{ cm}^{-1}$ in the Ag_8 are for the scissor, $\omega = 273.83 \text{ cm}^{-1}$ in the Ag_7 correspond to the the stretching. While $\omega = 189.34 \text{ cm}^{-1}$ in the Ag_8 is for the symmetric stretching, the others correspond to the antisymmetric stretching. As a result, the same structure of Au and Ag clusters have different vibrational frequencies, as seen in Au_8 and Ag_8 , because of having different masses. The mass of Au atom is bigger than that of Ag. The frequency and mass are inversely related. Therefore, the vibration frequencies of Ag clusters are greater than that of Au clusters for the same structure. On the other hand, some vibrational modes within Ag_4 and Ag_3 are smaller than that for the same structure of Au clusters due to having different angle and bonding properties.

Finally, we observe that our results are in agreement with experimental data for dimer and both Ag and Au clusters have planar structures.

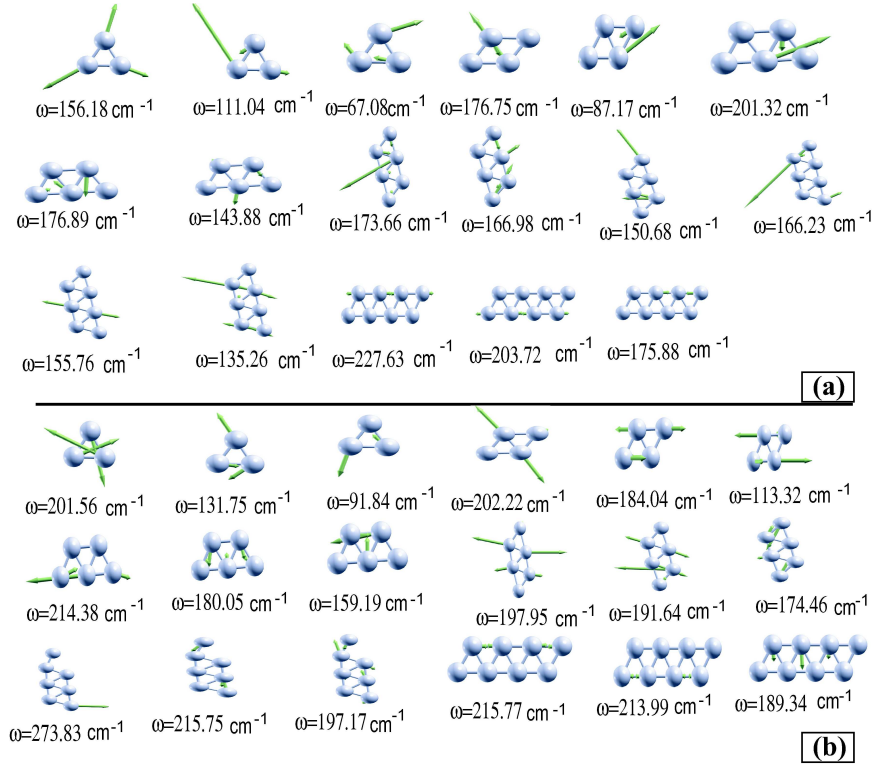


Figure 3.5: Vibration modes of stable configuration of Ag_n clusters obtained by using (a) GGA and (b) LDA [19].

STM images and DOS are calculated for Ag_8 and Au_8 . For Au cluster, We see that there exists a hybridization in both DOS and STM and that covalent binding is more effective. For Ag clusters, s and d orbitals are involved in metallic binding which is more effective than covalent binding [19].

3.5 The Stable Configurations Of Au_nPt_m Clusters

We obtain the same method as above the stable structures of Au_nPt_m up to $m + n = 6$ atom. The bond length of $AuPt$ cluster for GGA , LDA and experimentally respectively, 2.52, 2.43 and 2.60 Å[124]. GGA results are in good agreement with experimental data. The binding energy of $AuPt$ cluster for GGA and LDA are 2.58 eV and 3.22 eV, respectively. Total and absolute magnetization of $AuPt$ are 1.16 Bohr mag/cell and 1.35 Bohr mag/cell for GGA, for LDA, 1.24 Bohr mag/cell and 1.29 Bohr mag/cell, respectively.

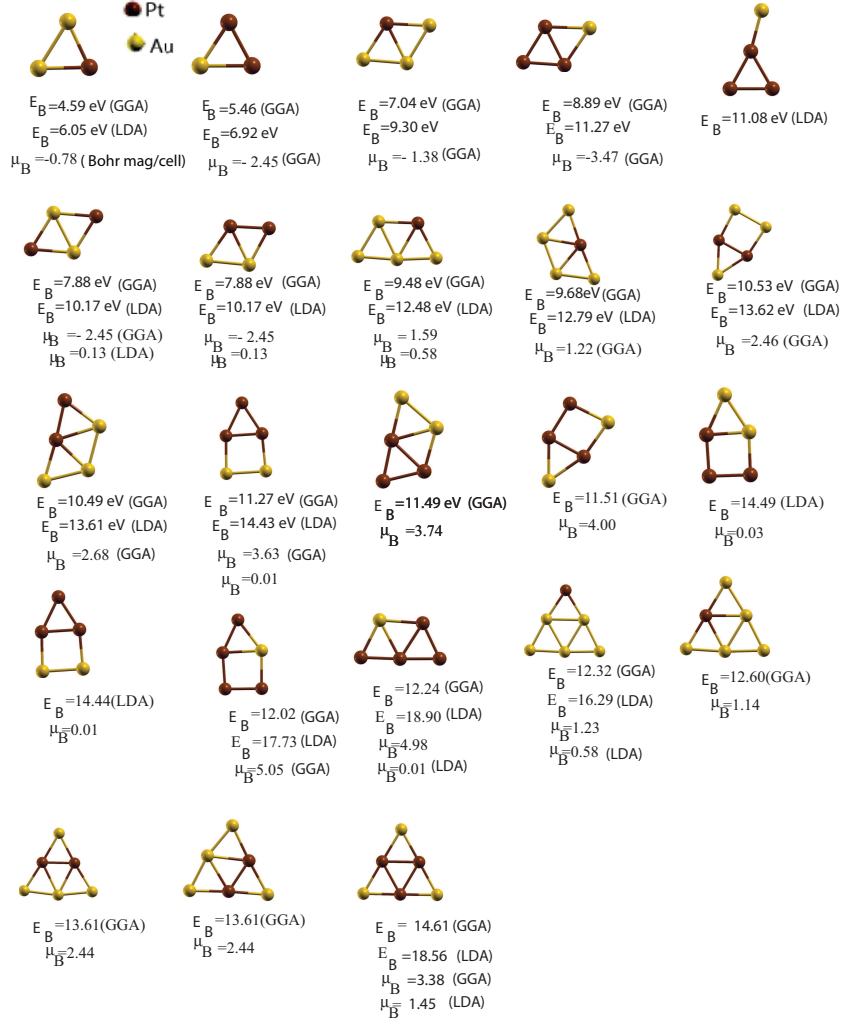


Figure 3.6: The stable structures of Au_nPt_m within GGA and LDA.

We calculated the binding energy as follows;

$$E_B = E_{cluster} - M * E_{Au} - N * E_{Pt}. \quad (3.2)$$

where E_{Au} and E_{Pt} , $E_{cluster}$ denote the energy of a single atom and the total energy of an atom in the cluster respectively and M and N are the number of atoms of Au and Pt respectively.

The binding energy per atom shows that Au_mPt_n clusters have favor planar structures. The stable configurations, binding energy and magnetic moments of Au_mPt_n clusters

are shown in Fig.3.6. We see that GGA results are in agreement with LDA results as seen in Fig.3.6. We find that Au_3Pt_3 have similar shape in both LDA and GGA.

3.6 NH_3 and H_2S Adsorption on Au_3Pt_3 Cluster

Despite of all these investigations, the work on Au_3Pt_3 cluster is really scarce. We therefore consider the adsorption of NH_3 and H_2S on Au_3Pt_3 clusters [24]. Catalytic activity increases as the cluster size is getting smaller. This is why we consider the Au_3Pt_3 cluster. There are different reasons for studying NH_3 . The nitridation of silicon surface is of technological importance. The resulting silicon nitride acts as a dielectric layer in metal-insulator-semiconductor devices [125, 126, 127]. Ammonia dehydrogenation and oxidation have been extensively studied [128, 129, 130, 131, 132, 133]. The adsorption of ammonia on nanostructures is important for controlling the catalytic processes in gas generators. This is also important for oxygen production for electric fuel cells [24, 134, 135]. H_2S , on the other hand, is toxic and corrosive. It presents serious problems to the environment and industry. It is therefore of both scientific and technological importance to develop nanoscale sensors in addition to the more traditional macroscopic scale H_2S sensors [136, 24]. In a part of this chapter, we give information about NH_3 and H_2S adsorption on Au_3Pt_3 .

3.6.1 Computational Details

PWSCF [15] is used in our calculations. We carried out all calculations at the Γ - point. We have used two different approximations: GGA and LDA for establishing the equilibrium structure of Au_nPt_n cluster up to $n=3$ atoms in vacuum. We find similar equilibrium structures for Au_3Pt_3 within GGA and LDA. We have also established the equilibrium structure for NH_3 and H_2S by using the same method.

We have used the ultrasoft pseudopotentials within GGA and LDA [71, 109, 63, 137].

A cutoff energy of 408eV is used with the planewave basis. Hellmann-Feynman forces and conventional minimization techniques are used to determine the equilib-

rium structure.

We calculate the adsorption energy, as follows;

$$E_a = -(E_{total} - E_{cluster} - E_{adsorbate}). \quad (3.3)$$

where $E_{cluster}$ and $E_{adsorbate}$ denote the energy of the isolated Au_3Pt_3 and the adsorbate, respectively.

We have investigated the charge transfer by using the Lowdin analysis [138].

The energy levels and charge densities are calculated for energies around the Fermi level [24].

3.6.2 The Electronic Properties of NH_3 and H_2S Adsorption on Au_3Pt_3 Cluster

We tried six possible configurations for adsorption of NH_3 and H_2S on Au_3Pt_3 cluster, as shown in Fig.3.7.

We see that the relaxed structures for starting B2 and H2 configurations are the same for GGA. The initial and stable configurations are given in Fig.3.7. As seen in Fig.3.7 (b)-(d) and (f), the strong interaction between Pt and N atoms results in the modification of Au_3Pt_3 cluster for H1,H2,T1 and B1 -sites. Fig.3.7(e) shows that the shape of the cluster is not modified after the interaction only for the T2-site where the interaction between Au and N is weaker. It is important to note that the cluster transforms from a planar to a three -dimensional structure in cases of adsorption on H1, H2, T1 and B1 -sites for NH_3 and H1- and H2- sites for H_2S within GGA and B2- site for NH_3 and T1- site for H_2S within LDA [24].

The calculated adsorption energies and bond lengths of NH_3 on Au_3Pt_3 are given in Table 3.6 We observe that the most stable structure is H2 with the largest adsorption energy. The smallest bond length between Pt and N is for the H2- site which is close to the experimental value of $(2.01(\text{\AA}))$ [139]. There is a stronger interaction between Pt and N atoms than between Au and Pt so that they have smaller bond lengths. N

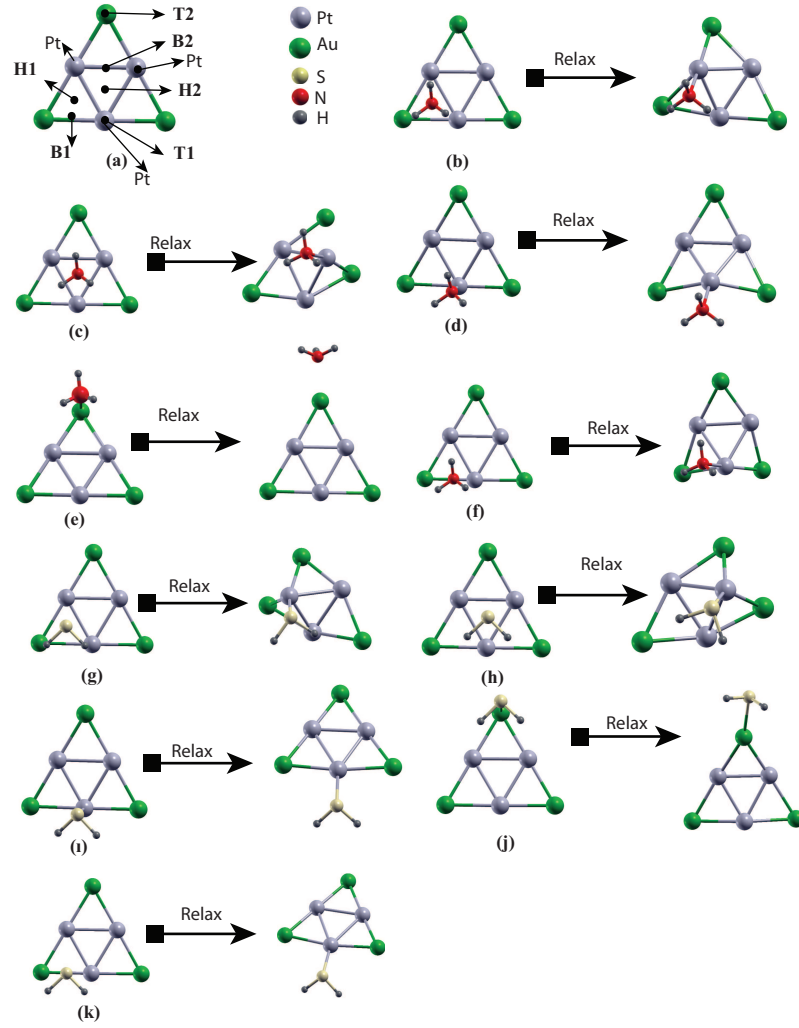


Figure 3.7: $Au_3Pt_3 - NH_3$ and $- H_2S$ within GGA, (a) the stable configuration of Au_3Pt_3 , (b) initial (left) and final (right) configurations at H1 (c) initial (left) and final (right) configurations at H2, (d) initial (left) and final (right) configurations at T1, (e) initial (left) and final (right) configurations at T2, (f) initial (left) and final (right) configurations at B1, (g) initial (left) and final (right) configurations at H1 for $Au_3Pt_3 - H_2S$, (h) initial (left) and final (right) configurations of H2, (i) initial (left) and final (right) configurations at T1, (j) initial (left) and final (right) configurations at T2, (k) initial (left) and final (right) configurations at B1 [24].

atom prefers to bind to the Pt atom. The bond length between Au and N is longest for the T2- site. It is close to the bond lengths given in the literature [140, 141].

The total charge transfers are given in Table.3.6 for NH_3 adsorption on Au_3Pt_3 within GGA. While the charge on Au_3 increases, the charge on Pt_3 and NH_3 decreases as seen in Table.3.6 for H1, H2 -sites. There is charge transfer from NH_3 to Au_3Pt_3 cluster. The total charge on Au_3 and Pt_3 increases but the charge on the Pt atom

Table 3.6: GGA results for NH_3 on Au_3Pt_3 : adsorption energies E_a (eV), bond lengths (d) (Å), the total charge transfer from the adsorbate to Au_3Pt_3 ($\Delta\rho$), total magnetization (M)($\mu_B/cell$) for all sites, NB stands for 'not binding' [24].

	H1	H2	T1	T2	B1
E_a	1.39	1.64	1.12	1.00	1.44
d ($Au-N$)	NB	NB	NB	2.24	NB
d ($Pt-N$)	2.14	2.11	2.17	NB	2.14
d ($Au-Pt$)	2.69	2.64	2.65	2.65	2.66
d ($N-H$)	1.02	1.02	1.02	1.02	1.02
d ($Pt-Pt$)	2.63	2.62	2.62	2.61	2.62
$\Delta\rho(e)$	0.18	0.16	0.17	0.26	0.16
M	3.22	3.11	3.20	3.38	3.20

which binds N decreases. The charge on NH_3 decreases for T1- and B1- sites. For the T2- site, the charge transfer is similar to the case of T1- site but in addition, there is a charge transfer between Au and Pt atoms.

The total magnetization of NH_3 on Au_3Pt_3 is given in Table.3.6. Magnetization values are closer to each other for all sites within GGA.

We have also calculated the energy levels and charge densities near the Fermi level at the Γ -point for spin up and spin down states within GGA. Energy levels and charge densities, for five configurations and for the bare Au_3Pt_3 cluster are given in Fig.3.8. Fig.3.8 (b) and (c) show that charge distributions for the highest occupied molecular orbital (HOMO) are on the Pt and Au atoms and the bond between Pt and N . This result is in agreement with the charge transfer analysis. Fig.3.8 (d) shows that the charge distributions for the HOMO, there is the charge on Pt and Au atoms. This charge distribution is also reflected on the charge distribution of the HOMO. For T2, charge distributions are on the Pt and Au atoms as seen in Fig.3.8 (e). For B1-site, Generally, the charge distributions on the HOMO and the the lowest unoccupied molecular orbital (LUMO) are on the Pt and Au atoms as seen in Fig.3.8(f). LUMO is closer to Fermi level for B1-site as in Fig.3.8(f).

We have done the same calculations within LDA. Adsorption energy (E_a), bond lengths (d), M, $\Delta\rho$ are given in Table 3.7.

The calculations for the adsorbate at the H1,H2 and B1-sites are not converged. The most stable configuration is for the T1 -site as seen in Table 3.7.

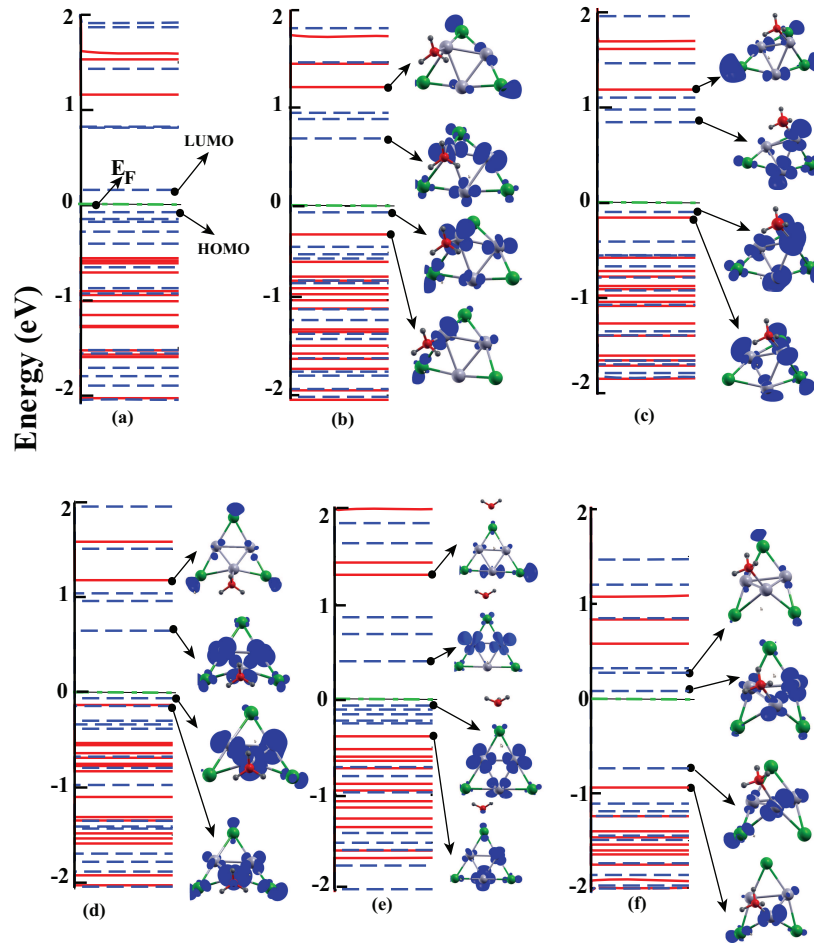


Figure 3.8: Energy levels and charge densities Au_3Pt_3 within NH_3 for GGA; (a) bare Au_3Pt_3 (b) H1, (c) H2, (d) T1, (e) T2, (f) B1 (line shows spin up states. Dashed line shows spin down states) [24].

N prefers to bind to the Pt atom. These results are in agreement with the GGA results. The total magnetization for B2-site is zero. The highest magnetization value is for the adsorption to the T2- site. The stable configurations are given in Fig.3.9.

The energy levels and charge densities near the Fermi level for spin up and spin down states are given in Fig.3.10 (a)-(c). Generally, the charges are on the Au_3Pt_3 cluster. The results show that the calculated values strongly depend on the type of exchange-correlation functional used.

We performed the same calculations for $Au_3Pt_3-H_2S$. The stable and initial configurations are given in Fig.3.7 (g)-(k). We obtain similar configurations as in $Au_3Pt_3-NH_3$.

Table 3.7: LDA results for NH_3 on Au_3Pt_3 : adsorption energies E_a (eV), bond lengths (d) (Å), the total charge transfer from the adsorbate to Au_3Pt_3 ($\Delta\rho$ (e)), total magnetization (M) ($\mu_B/cell$) for all sites [24].

	T1	T2	B2
E_a (eV)	2.26	1.78	2.16
d ($Au-N$)	NA	2.13	NA
d ($Pt-N$)	2.04	NA	2.07
d ($Au-Pt$)	2.52	2.56	2.57
d ($N-H$)	1.03	1.03	1.03
d ($Pt-Pt$)	2.62	2.54	2.53
$\Delta\rho$ (e)	0.32	0.31	0.27
M	0.96	3.00	0.00

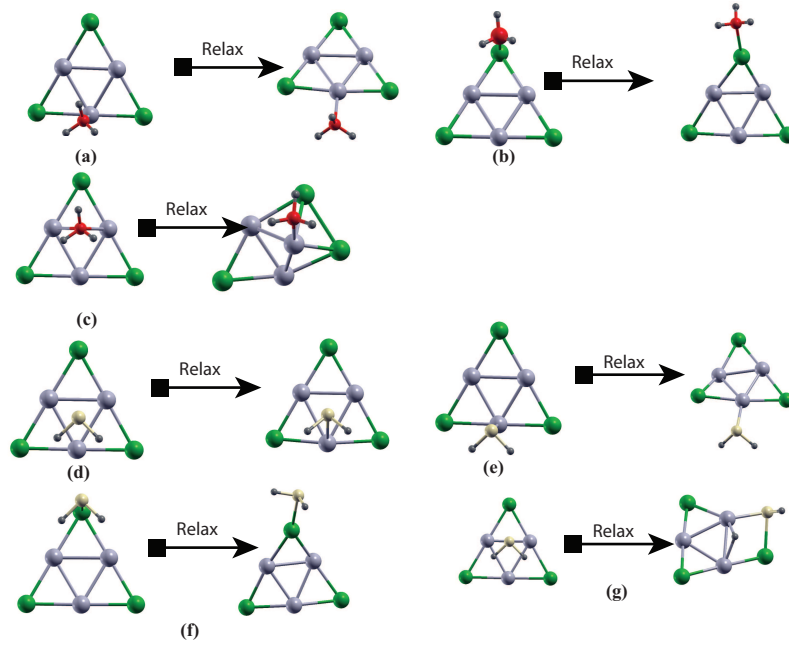


Figure 3.9: $Au_3Pt_3-NH_3$ and $Au_3Pt_3-H_2S$ for LDA, (a) initial (left) and final (right) configurations at T1 (b) initial (left) and final (right) configurations at T2, (c) initial (left) and final (right) configurations at B2, (d) initial (left) and final (right) configurations at H2 for $Au_3Pt_3-H_2S$, (e) initial (left) and final (right) configurations at T1 for $Au_3Pt_3-H_2S$, (f) initial (left) and final (right) configurations at T2 for $Au_3Pt_3-H_2S$, (g) initial (left) and final (right) configurations at B2 for $Au_3Pt_3-H_2S$ [24].

There is a strong interaction between S and Pt atoms. The shape of the cluster is modified after the adsorption, as seen in Fig.3.7(g) and (h).

Adsorption energies and bond lengths calculated within GGA are given in Table.3.8. We see that the relaxed structures for starting B2 and H2 are the same [24]. The most stable configuration is H1. The bond length between $Au-S$ and $Pt-S$ are in agreement

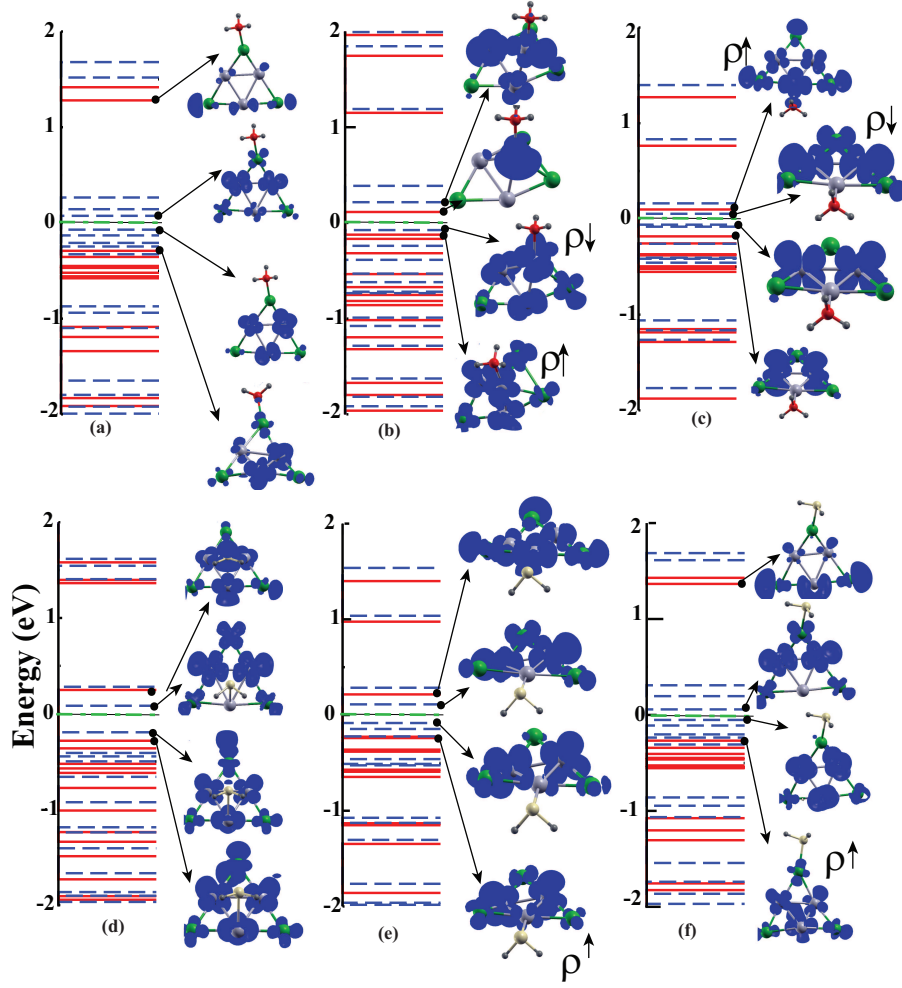


Figure 3.10: Energy levels and charge densities within $Au_3Pt_3-NH_3$ and $Au_3Pt_3-H_2S$ for LDA; (a) NH_3 at T1 -site, (b) NH_3 at T2 -site, (c) NH_3 at B2- site, (d) H_2S at H2 -site, (e) H_2S at T1 -site (f) H_2S at T2 -site, (g) H_2S at B2 -site [24].

with the available literature [142, 143].

The total charge transfers are given in Table.3.8 within GGA. The charge on the Pt atom which bonds to S atom increases for H1- and H2- sites. The charge on H_2S decreases for H2-, T2- and H1- sites but overall, the charge on the Au_3Pt_3 cluster increases.

For T1- and B1-sites, the charge on the Au_3 atoms decreases, Pt_3 atoms increases, There is also charge transfer to Au and Pt atoms. The charge on the H_2 atoms increases for T1- and B1- sites. The charge on the Au_3 atoms increases, Pt_3 atoms decreases within T2. There is a net charge transfer from H_2S to the Au_3Pt_3 cluster for

Table 3.8: GGA results for H_2S on Au_3Pt_3 : E_a (eV), bond lengths (d) (Å) and the total charge transfer from the adsorbate to Au_3Pt_3 ($\Delta\rho(e)$), total magnetization (M) ($\mu_B/cell$) for all sites [24].

	H1	H2	T1	T2	B1
E_a	1.61	1.60	1.16	0.84	1.16
d ($Au-S$)	NB	NB	NB	2.428	NB
d ($Pt-S$)	2.256	2.25	2.25	NB	2.26
d ($Au-Pt$)	2.68	2.68	2.62	2.65	2.62
d ($S-H$)	1.37	1.37	1.37	1.36	1.37
d ($Pt-Pt$)	2.63	2.63	2.69	2.60	2.69
$\Delta\rho$ (e)	0.18	0.18	0.24	0.37	0.24
M	3.08	3.10	2.49	3.35	2.51

all sites.

The total magnetization of $Au_3Pt_3-H_2S$ is given in Table.3.8 within GGA. Generally, the magnetization values are close to each other. The smallest magnetization value is for the adsorption on T1- site.

We have calculated the energy levels and charge densities corresponding to states around the Fermi level for spin up and spin down states. Energy levels diagrams and charge densities for five configurations and for bare Au_3Pt_3 cluster are given in Fig.3.11.

Fig.3.11(a) shows that, generally the charge distribution are on the Au and Pt atoms for H1- site. But there exists the charge distribution on the S atoms for the LUMO. For H2- site, It has similar charge distribution to H1- site as seen in Fig.3.11(b). The charge density are on the Au , Pt and the bond between Pt and S atoms for T1- site (Fig.3.11(c)). But for, there is no charge density on Pt which binds to N for the LUMO. For T2- site, Fig.3.11(d) shows that there exists charge on the Au and Pt atoms. For the HOMO, while there exists charge on the Pt atom which bonds to S atoms, there is no charge on the bond between Pt and S atoms within B1- site (Fig.3.11(e))for the LUMO. The LUMO is closer to Fermi level for H1-, H2-, T1- and B1- sites as seen in Fig.3.11(a),(b),(c), and (e). These results are in agreement with the charge transfer results.

E_a , d , M, $\Delta\rho$ values calculated within LDA are given in Table.3.9. The self- consistent computation for the adsorbate at the H1 and B1-sites are not converged. There

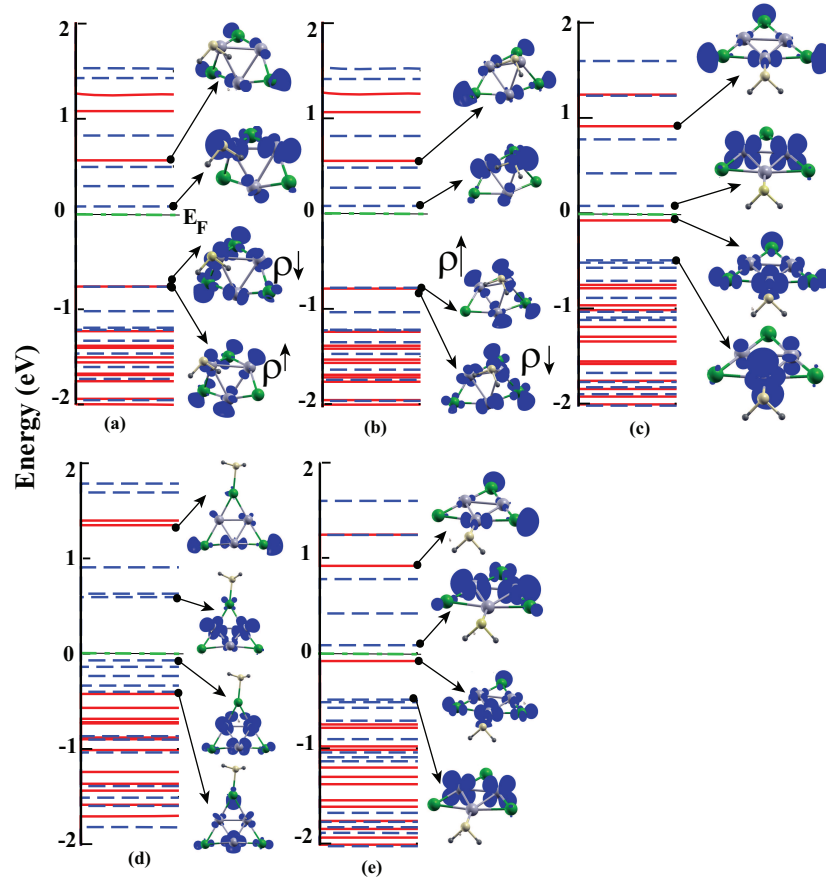


Figure 3.11: Energy levels and charge densities within $Au_3Pt_3-H_2S$ for GGA; (a) H1, (b) H2, (c) T1, (d) T2, (e) B1 [24].

are no relaxed structures for these sites. The adsorption of the B2 -site shows a totally different structure from others. H_2S dissociates at this site. The dissociated H binds to Pt . The remaining S binds to both Au and Pt with its H attached as seen in Fig.3.9(g)[24]. The bond length of $Pt-H$ is in agreement with literature [106, 144]. The adsorption energies calculated are bigger than those calculated within GGA. The most stable configuration is B2- site, as seen in Table 3.9. The highest magnetization value is for the adsorption to T2- site. There is total charge transfer from the adsorbate to cluster but there occurs a charge transfer to both H from the binding Pt and S atoms. The stable configurations are given in Fig.3.9. The energy levels and charge densities near the Fermi level for spin up and spin down states are given in Fig.3.10 (d)-(f) and in in Fig.3.12. Generally, there are charges on the Au_3Pt_3 cluster. There is

Table 3.9: LDA results for H_2S on Au_3Pt_3 : E_a (eV), bond lengths (d) (Å) the total charge transfer from the adsorbate to Au_3Pt_3 ($\Delta\rho$ (e)), the total magnetization (M) ($\mu_B/cell$) for all sites [24].

	H2	T1	T2	B2
E_a	1.43	2.05	1.61	8.59
d (Au-S)	NB	NB	2.31	2.33
d (Pt-S)	2.22	2.19	NB	2.23
d (Au-Pt)	2.56	2.54	2.56	2.62
d (S-H)	1.40	1.37	1.36	1.37
d (Pt-Pt)	2.69	2.61	2.53	2.58
d(Pt-H)	NB	NB	NB	1.73
$\Delta\rho$ (e)	0.50	0.40	0.43	0.25
M	1.00	1.00	3.00	1.09

a charge on the bond between $Au-S$ for B2-site, as seen in Fig.3.12.

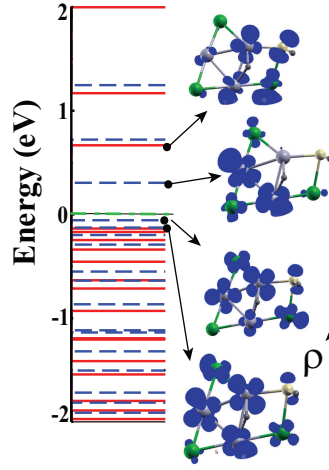


Figure 3.12: Energy levels and charge densities within $Au_3Pt_3-H_2S$ for B2 within LDA [24].

We observe that $Au_3Pt_3-NH_3$ and $Au_3Pt_3-H_2S$ have Fermi levels between the HOMO and the LUMO for all sites. There is a charge transfer from the adsorbate to Au_3Pt_3 cluster in accordance with the Löwdin analysis. It makes Au_3Pt_3 cluster semiconducting.

The results indicated generally that the electronic and geometrical factors are playing key roles for adsorption sites. Adsorption energies within GGA (LDA) are bigger for the sites H1 and H2 (T1 and T2) with higher coordination numbers for NH_3 . The bond lengths between the adsorbates and the Pt atom are the shortest. For H_2S , adsorption energies within GGA (LDA) are bigger for the sites H1 and H2 (B2) with

higher coordination numbers. The adsorption of H_2S to the B2 -site shows a totally different structure from others. H_2S dissociates at this site within LDA.

There is a strong interaction between Pt and N atoms and also between Pt and S atoms . Some of configurations are modified after the interaction. The clusters transforms from a planar to three dimensional structures for these sites [24]. We see that bond lengths between Au and N , Pt and N , Au and S , Pt and S , Pt and H are in agreement with the available literature [106, 139, 140, 141, 142, 143, 144].

There is a charge transfer from the adsorbate to the Au_3Pt_3 cluster according to the Löwdin analysis. We see that total charge transfer and total magnetization values are closer to each other for all sites within GGA. LDA results give smaller total magnetization and bigger charge transfer than GGA.

We have also calculated the energy levels for all configurations. We observe that the energy levels around the the Fermi level correspond to charge distributions which are in agrement with the results of the Löwdin analysis.

Comparing d and E_a for both adsorbates, we see that $Pt-N$ interaction is generally stronger than $Pt-S$ interaction, as a result of this, E_a in NH_3 adsorption (d) is bigger (smaller) than in H_2S adsorption, with the exception of B2- site within LDA [24].

CHAPTER 4

Au₈ CLUSTER ADSORPTION ON Si(100):2x1 ASYMMETRIC SURFACE

In this chapter, we investigate the adsorption of Au₈ cluster onto H-terminated Si(100):2x1 asymmetric surface [2].

A group of adsorption studies on *Si*(100) concentrates on problems associated with the electronic device applications; namely the metal contacts needed in this technology [145, 146, 147, 148, 149, 150, 151]. The study of adsorption of the nano-clusters on *Si* surfaces is developing fast. J.Mach et al. [152] investigated the influence of atomic hydrogen on the *Si*(100) substrate with submonolayer gallium surface phases as well as the deposition of gallium on monohydride terminated *Si*(100):(2x1)-H surface using synchrotron radiation photoelectron spectroscopy and low energy electron diffraction.

G. Lee et al. [153] studied thallium nanoclusters on *Si*(111):7x7 by using density functional total energy calculations. They found that thallium is unstable with the triangular cluster in comparison with clusters of other group III elements (Al, Ga, and In).

There is less information about gold cluster adsorption on *Si* surfaces. L. Zhang et al. [154] investigated the influence of substrate temperature on the adsorption of submonolayer *Au* on *Si*(111):(7x7) surface by using scanning tunneling microscopy. When the substrate temperature is increased from room temperature to 565 °C, they observed a 5x2 reconstruction as a result of interaction between *Au* and *Si* atoms.

L.Zhao et al. [155] have grown dome-shaped gold nano-particles on *H-Si* (100) and have shown the gold-silicide formation at the interface.

S.Konar et al. [26] investigated atomic gold chain formation on hydrogen terminated *Si*(001):(1x1) surface by using density functional theory (DFT) based total energy calculations. The adsorption of gold linear chain on silicon (001):(1x1) surface is carried out for various submonolayer coverages by removing desired hydrogen atoms from the surface. They found that the chainlike structures of Au atoms are favorable and that favorable sites change with increase in the coverage.

B.Yoon et al. [31] have shown that charging of the Au_8 cluster on *MgO* is very important in increasing their chemical activity. The cluster-solid surface bond length distribution and size -selected cluster deposition on solid surfaces are studied experimentally and theoretically [156, 157].

Despite of all earlier investigations there is still a need to understand better the interaction between the adsorbed cluster and the *Si* substrate. In this work, we, therefore, investigate the adsorption of Au_8 cluster on hydrogen terminated *Si*(100)-4x4 surface by using DFT within local density approximation (LDA) and generalized gradient approximation (GGA). In the absence of the experimental information it makes sense to start first with the simplest calculations. We consider only eight atoms in the cluster, which makes the total number of atoms considered in this work 120 [2]. Au_8 clusters are important because they are the smallest clusters with catalytic activity [31]. There are several investigations in the literature showing that the shape of the adsorbed cluster does not change much for a large number of atoms in the cluster [158, 159]. This is why we consider a small cluster. There is no reported work about Au_8 cluster adsorption on *Si*(100) surface, up to now.

We have calculated the adsorption energy, band structure and charge distribution. Our results show that the shape of the adsorbed Au_8 cluster changes depending on the adsorption site. We show that the shape of the adsorbed cluster and adsorption energy change both with the numbers of *Si* and *Au* atoms interacting with each other [2].

4.1 Computational Details

We have used PWSCF program [15]. The kinetic energy cutoff of plane waves is taken as 408 eV. The *Au*-cluster and *Si* substrate complex is modelled by a periodic supercell. This super cell consists of seven *Si* layers in including a surface cell, *Si*(100) p(2x1) asymmetric surface, which is modelled by [160]. The supercell are separated by about 10Å. The dangling bonds of the lower surface atoms in the slab were saturated with hydrogen atoms. Saturation with *H* is needed to the stabilize configuration of the substrate. The supercell contains 96 *Si*, 16 *H* and 8 *Au* atoms [2].

The Brillouin-zone (BZ) sampling is performed using 2x4x1 grid of Monkhorst-Pack [161] special k points and using a Methfessel and Paxton [162] smearing approach for the electronic states near the Fermi level, with a Gaussian width of 0.02 Ry. The figure of BZ is given as Fig.3 in the paper by Ramstad et al.,[160].

The choice of exchange-correlation (xc) functional is one of the essential points in all DFT calculations. We have used the ultra soft pseudopotentials (Perdew-Zunger [109] and Perdew-Burke-Ernzerhof [63, 163] and Rabe Rappe Kaxiras Joannopoulos [137] exchange-correlation (xc).

The adsorption energy is defined as

$$E_a = E_{total} - E_s - E_c. \quad (4.1)$$

where, E_{total} , E_s and E_c are energies of *Si* substrate+cluster, the isolated *Si* substrate and the metal cluster, respectively.

Firstly, We obtain the stable configuration of Au_8 clusters within GGA and LDA in previous chapter. We find similar structures for Au_8 cluster within GGA and LDA. Then, *Si-H* system is relaxed to equilibrium keeping the lowest two *Si* layers fixed. The Hellmann-Feynman forces on the atoms after the ionic relaxation are smaller than 0.005 eV/Å. We use an orthorhombic supercell in this calculation. The lattice constants of the supercell are $a= 15.20$, $b= 15.35$ and $c= 30.41$ Å.

We calculated the charge transfer by using the Löwdin analysis [2, 138]

4.2 Si Bulk and Si(100):2x1 Asymmetric Surface

The *Si* bulk structure is decided by (sp_3) hybridization of *Si* atoms, resulting in four equivalent covalent bonds to nearest neighbors in a tetrahedral coordination. The bulk lattice has diamond structure with a basis formed by two *Si* atoms at (0,0,0) and (1/4, 1/4, 1/4) respectively as seen in Fig.4.1

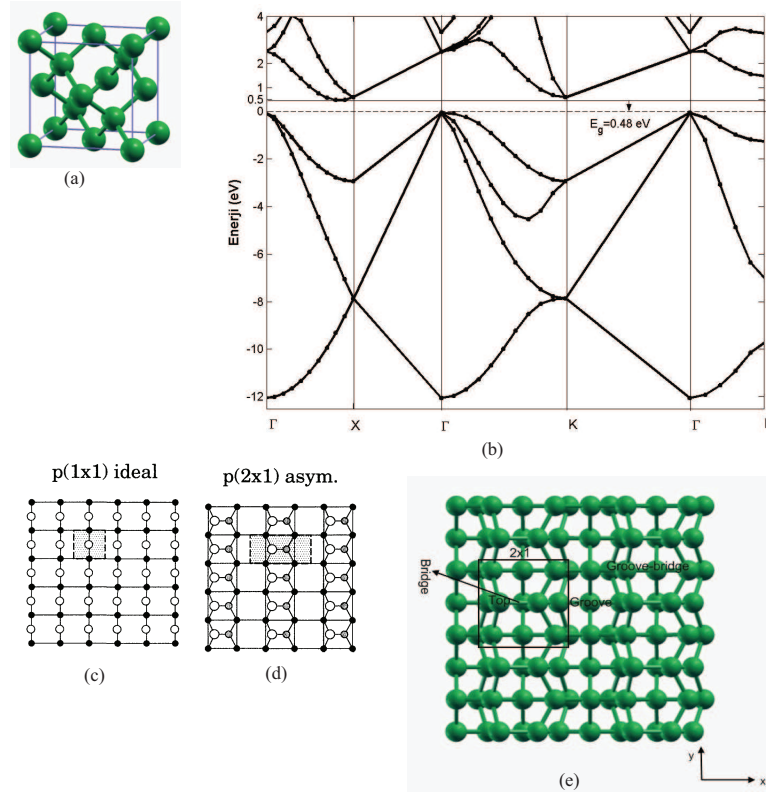


Figure 4.1: (a) The bulk structure of *Si*, (b) The band structure of bulk *Si*, (c) Top view of the ideal surface (Smaller and darker circles show deeper atoms) [160], (d) p(2x1) asymmetric surface [160].

We found that the lattice constant is 5.41 Å. This is in agreement with experimental data [164] within LDA. The Energy band diagram is given in Fig.4.1(b) for the bulk.

The reactivity of the *Si* surface is in part due to dangling bonds. *Si* atoms are bonded fewer than four bulk *Si* atoms at the surface and leaving dangling bonds. The *Si*(100)

Table 4.1: The adsorption energies and bond lengths of Au_8 cluster for different sites on the Si(100) : (2x1) surface [2].

Site	$d(Au-Si \text{ \AA})$	$d(Au-Au \text{ \AA})$	$E_a(\text{eV})$
P	2.37	2.78	13.38
B	2.39	2.62	3.58
T	2.40	2.58	9.67
G	2.29	2.63	5.20

surface, atoms rearrange, that is a reconstruction occurs to minimize the total energy and eliminate the dangling bonds. Its surface geometry shows different properties from the that of bulk [165]. There exists a number of differently reconstructed Si(100) surface, such as , p(2x1)symmetric, c(4x2) and p(2x1) asymmetric surface. Between them, we choose p(2x1) asymmetric surface. The shape of the reconstruction p(2x1) asymmetric surface and Si (100) asymmetric surface are given in Fig.4.1(d) and (e). Asymmetric surface have lower energy than symmetric surface [160].

4.3 Electronic and Structure Properties Analysis

We consider four possible configurations for the Au_8 cluster for adsorption on Si surface. The top site (T) which is directly above a Si -atom, the bridge site (B) at the midpoint of a Si and Si bond, groove site (G) is the midpoint on the atomic groove of Si surface and parallel configuration (P) in which the adsorbate lies parallel to the surface.

The stable configurations of Au_8 on Si surface and initial configuration in the cell are given in Fig. 4.2. For LDA, there is no change in the shape of Au_8 cluster in the G-, B-, P- configurations, but the shape of the cluster is modified in the T- site geometry, Si-Au interaction is stronger than the Au-Au interaction. Thus, the bond between Au-Au breaks, Au_8 cluster is modified more in this configuration, as seen in Fig. 4.2b. In the P- site geometry, there is a little modification in the cluster.

The adsorption energies, maximum and minimum distances between Si and Au atoms and Au-Au atoms within LDA are given in Table.4.1.

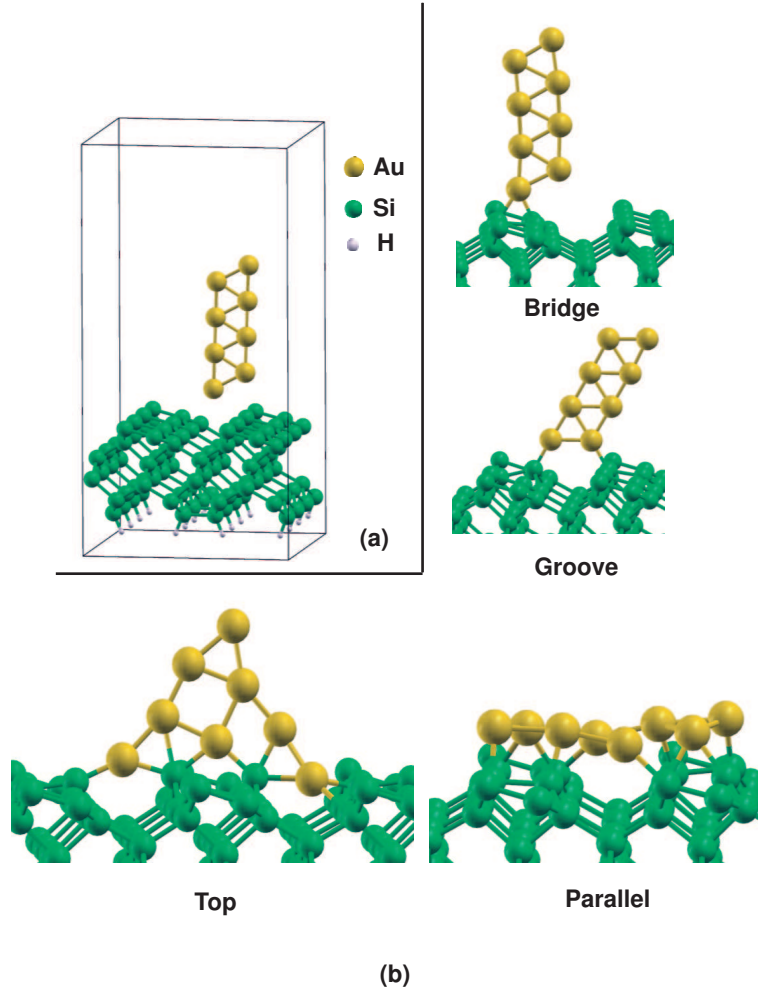


Figure 4.2: The configuration of Au_8 on $H-Si(100)$ system a) orthorhombic unit cell and stable configurations of Au_8 cluster adsorption on different sites of the H-terminated Si (100) surface [2].

The adsorption energy for the P-configuration is much larger as seen in Table.4.1. The number of gold atoms interacting with Si surface are more than those in other sites, so the adsorption energy for P- configuration is bigger, even though the $Au-Si$ distance for G- site is smaller than that for the P- site. The adsorption energy for G- site is higher than the B- site. Furthermore, the bond length between $Au-Si$ atom is smaller than that for the other sites. In the G- site, the number of surface atoms interacting with Au_8 cluster are bigger than for the B- site. These results show clearly that the shape of the adsorbed cluster and adsorption energy change both with the numbers of Si and Au atoms interacting with each other.

The band structure and charge density of the four configurations and bare *Si* surface within LDA are given in Fig. 4.3 and Fig. 4.4 [2].

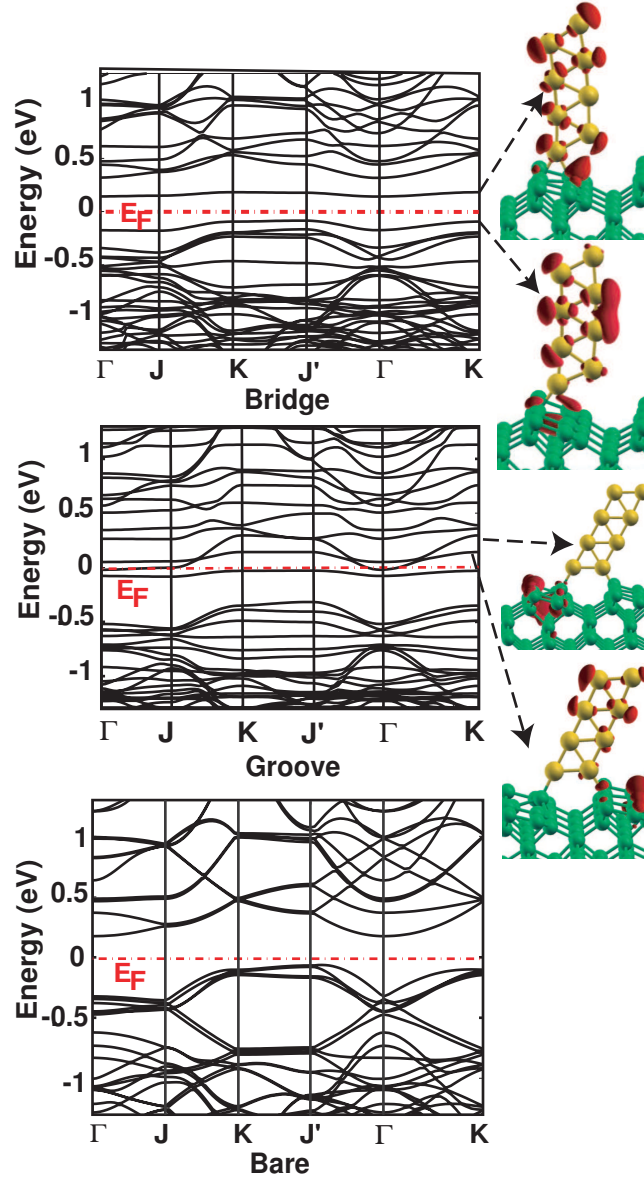


Figure 4.3: Electronic energy bands of Au_8 on $H-Si(100)$ system for the Au_8 cluster on the B-, G- sites and for the bare H -terminated $Si(100)$ within LDA [2].

Band structure of *Si* slab has been found to have semiconducting properties in agreement with the literature [160]. It is interesting to note that while for B-, T- and P-sites, these systems show semiconducting properties, For G- site, the system may be metallic. The physical properties of the substrate with gold cluster is found to change

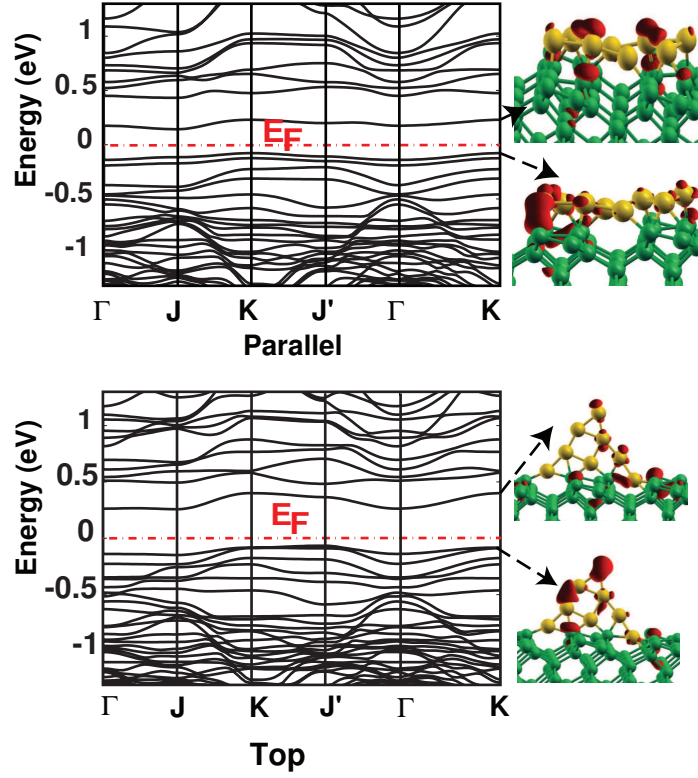


Figure 4.4: Electronic energy bands of Au_8 on $H-Si(100)$ system for the Au_8 cluster on the P- and T- sites within LDA [2].

with respect to the location of the cluster.

We also calculate the charge densities within LDA for four configurations near the Fermi level at the Gamma point. The charge density is given in Fig. 4.3 for the slabs with the cluster on B- site. The Charge densities corresponding to bands just under and above the Fermi level are mainly on the Au atoms and also in the $Au-Si$ bonds. There is little charge on the Si surface coming from the band just under the Fermi level. But in the G- site, charge density corresponding to bands just under the Fermi level is on the surface atoms, charge density is mainly on Au and Si atoms above the Fermi level. The charge is denser near Au atoms which are away from the surface.

The charge distribution and bands within LDA are given in Fig.4.4 for the P-configuration and T-site. Charge densities corresponding to bands just under and above the Fermi level are mainly on the Au_8 cluster for both sites. There is a little charge on the Si surface and the charge is in between $Au-Si$ atoms for both.

We have also investigated the charge transfer between Au_8 cluster and Si surface by means of Löwdin analysis for four configurations. For B-, T- and P- site, there is a charge transfer from the surface to the Au atoms resulting in a decrease on the Si atoms near the Si surface. We also observe that there is a charge transfer between Si atoms. In the G- site geometry, there is a charge transfer from the surface to the Au atoms. But the charge on Au atoms which have four bonds at the middle decrease, while the charge on Si atoms which binds to Au atoms increase. The charge on other Si atoms which binds to other Au atoms decreases.

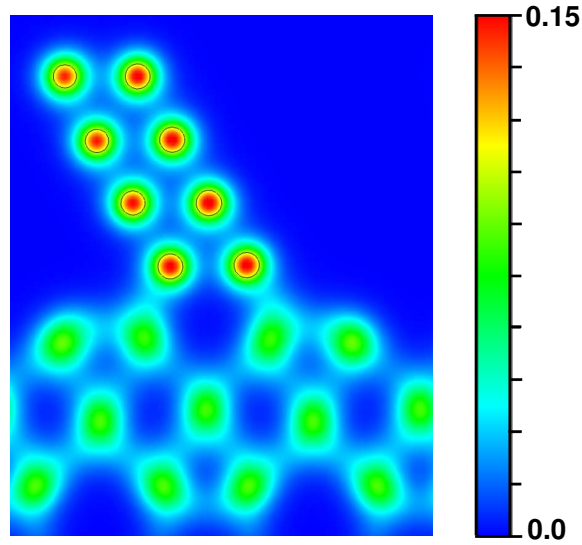


Figure 4.5: The charge density of Au_8 on $H-Si(100)$ system for the Au_8 cluster on the G-site site within LDA [2].

We calculate the charge density of the Si slab with the cluster in four configurations. For brevity, we give only the charge density for G- site in Fig. 4.5. $Au-Si$ bonds have covalent character as seen in the figure. Charge is also in the $Si-Si$ bonds. Both bonds show covalent character. These results show clearly that the shape of the adsorbed Au_8 cluster depends on the adsorption site.

The total density of states(DOS), partial density of states (PDOS) and local density of states (LDOS) are given in Fig.4.6. These are in line with our band structure and charge transfer results. The Fermi level is at a position with finite DOS only for the G-site case. This is in agreement with our earlier suggestion that the Au_8 cluster at

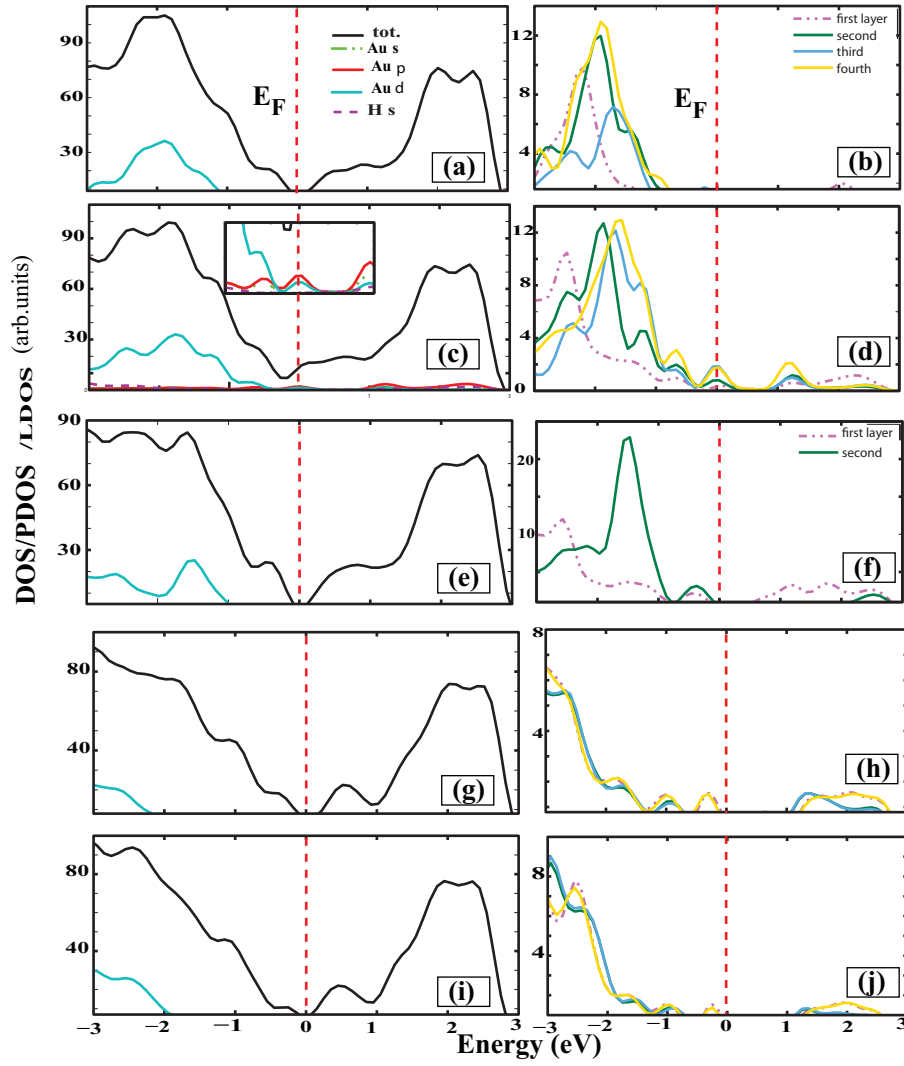


Figure 4.6: The density of states (DOS) of Au_8 on $H-Si(100)$ and partial density of states (PDOS) for Au_8 cluster for different sites. the Local density of states (LDOS) are given for different layers of the the Au_8 . (the first layer is two Au atoms closest to the surface (as shown in Fig.4.2 (b)) for B-G-P- sites, and it is the five Au atoms for T-site (as shown in Fig.4.2 (b)) (a) DOS and PDOS for B- site (b) LDOS for B-site (c) (DOS) and (PDOS) for G-site (d) LDOS for G-site (e) DOS and PDOS T-site (f) LDOS for T-site (g) DOS and PDOS for P-site (h) LDOS for P-site (i) DOS and PDOS for P-site GGA (j) LDOS for P-site GGA [2].

G-site yields a metallic complex.

We have also calculated the adsorption energy of gold cluster within GGA. For brevity, we give only the electronic properties for adsorption on the P-configuration. We find that adsorption energy is 10.25 eV. This is smaller than that of LDA. The band structure and corresponding charge distributions are given in Fig.4.7. We obtain

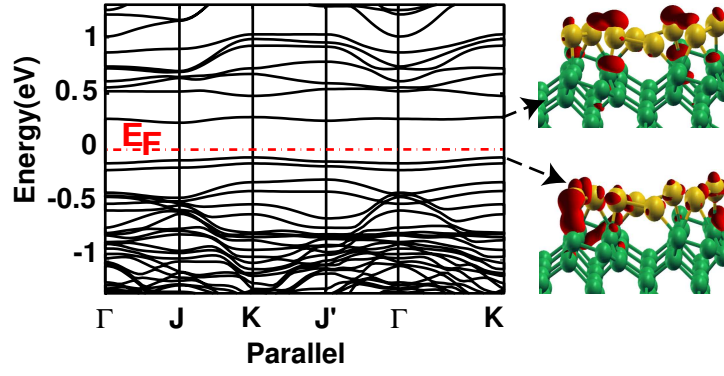


Figure 4.7: Electronic energy band of Au_8 on $H-Si$ (100) system for the Au_8 cluster on the P-site within GGA [2].

very similar bands and the corresponding charge distributions as in LDA for the P-configuration. We investigate the charge transfer between Au_8 cluster and Si surface. We observe that there is a charge transfer from the surface to Au atoms as in LDA for the parallel site. We see that GGA results are in general agreement with the LDA results [2].

CHAPTER 5

CLUSTERS ADSORPTION ON GRAPHENE

5.1 Graphene

Graphene is receiving increasing attention in condensed matter physics because of its unusual electronic properties. Electrons can travel in graphene thousands of inter-atomic distances without any scattering [34, 35, 39]. Graphene is a conductor with remarkable electronic properties [36, 37, 166, 167, 168]

Graphene is described as a flat monolayer of carbon atoms tightly packed into a two dimensional honeycomb lattice. It is a fundamental building block for graphitic materials of all other dimensionalities. Fullerenes (0D) is to be formed by wrapping up graphene and graphite (3D) is the 3D form of graphene. Carbon nano tube (1D) is to be formed by rolling graphene as shown in in Fig. 5.1.

Graphene is widely studied theoretically and is used to explain properties of the various carbon- based materials [35]. Graphene is obtained experimentally for the first time by a group of physicists from Manchester led by A.Geim and K. Novoselov [34, 166, 169]. They began with three-dimensional graphite and subtracted a single sheet (a monolayer of atoms)using micromechanical cleavage technique [34, 166, 169]. It is known that graphite is a layered material and can be described as a number of graphene crystals weakly coupled together. This property is used by the Manchester team. This finding is very important since two dimensional crystals exist and they are stable under environmental conditions and show high structural quality [34, 35, 36, 37, 38, 39, 169].

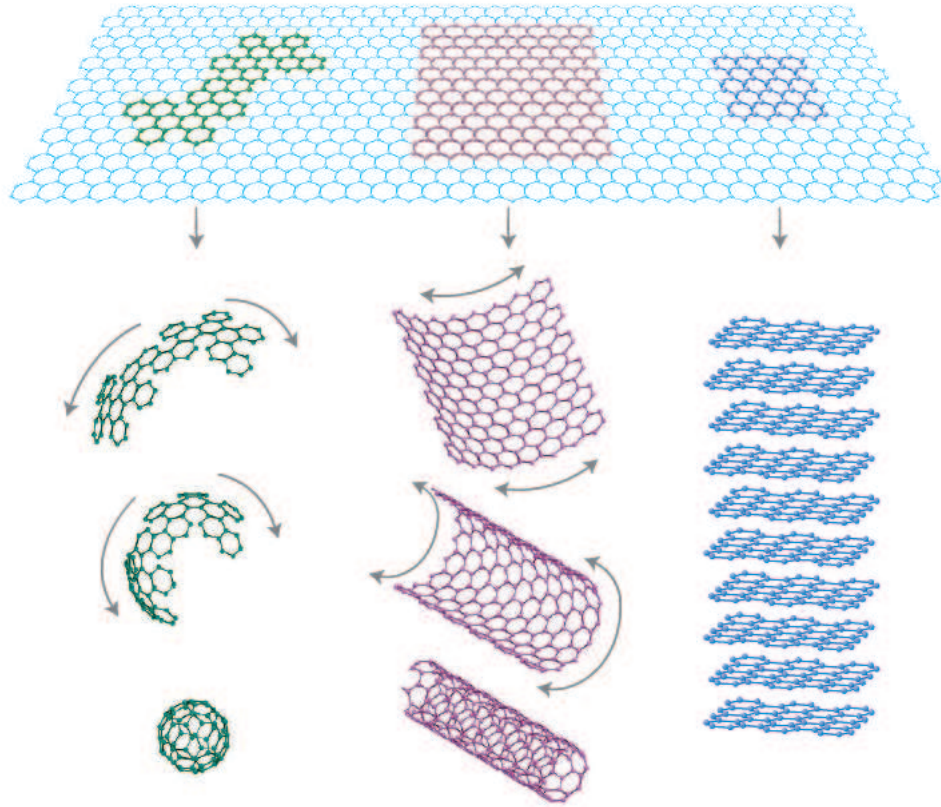


Figure 5.1: Graphene can be wrapped up into 0D fullerenes, rolled into 1D nanotubes or stacked into 3D graphite [35].

More than 70 years ago, Landau and Peierls claimed that strictly 2D crystals were thermodynamically not stable and could not exist. Mermin extended this argument by experimental observation. If the thin film thickness is decreased, the melting temperature decreases so the films become unstable at a thickness of dozens of atomic layers. 2D materials without such a 3D base were assumed not to exist until the discovery of graphene [35].

Graphene has two atoms per 1×1 unit cell. This results in two conical points per Brillouin zone where band crossing occurs, K' and K as shown in Fig.5.2. The electron energy is linearly dependent on the wave vector near these crossing points [169].

What makes graphene so interesting for researches? It has unusual transport and electronic properties. In condensed matter physics, Schrödinger equation is widely used. It is enough to describe electronic properties of materials. But it is not enough for

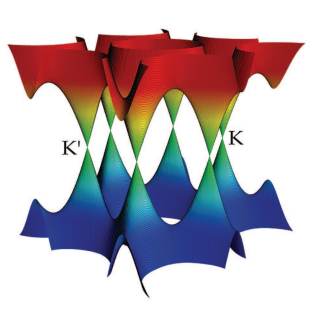


Figure 5.2: Band structure of graphene. (The conductance band touches the valence band at the K and K' points) [169].

graphene. Its charge carries similar to relativistic particles and described by starting with the Dirac equation instead of the Schrödinger equation.

Graphene has a spectrum which is closely similar to the Dirac spectrum for massless fermions. The Dirac equation defines relativistic quantum particles with spin $1/2$, such as electrons. Although there is nothing actually relativistic about electrons moving around carbon atoms, due to their interaction with the periodic potential of graphene's honeycomb lattice, new quasi particles occur at low energies E . They are described by the $(2 + 1)$ - dimensional Dirac equation with an effective speed of light $v_F \approx 10^6 m^{-1} s^{-1}$. These quasi particle which are called fermions can be described as electrons that have lost their rest mass m_0 or as neutrinos that acquired electron charge e . A quasi particle in graphene shows a linear dispersion relation $E = \hbar k v_F$ as if it was a massless relativistic particle. Due to the linear spectrum, it is excepted that quasi particles in graphene may be treated differently from those in conventional metals and semiconductors where the energy spectrum can be estimated by a parabolic (free electron-like) dispersion relation. From the point of view of graphene electronic properties, it is a zero-gap semiconductor [35, 169].

Graphene begins to be widely used in technology. It has been shown that granulated graphene of uncoagulated micrometer-size crystallites can be produced in a way scaleable to mass production. Another interesting possibility is the use of graphene powder in electric batteries. Due to large surface -to-volume ratio and high conductivity, it is possible to increase efficiency of batteries, taking over from the carbon

nanofibres used in modern batteries [35].

It is found that epitaxial graphene has good properties for coherent nanoscale electronics applications [170]. Graphene is therefore finding application in areas, such as hydrogen storage [35, 171, 172, 173, 174, 175, 176, 177], gas sensors [178, 169, 179] and spin-valve devices [169, 180, 181].

In this chapter, we investigate the adsorption properties of Au_nPt_n cluster and Bi , Bi_n on the graphene surface.

5.2 Au_nPt_n Clusters Adsorbed on Graphene

There are several investigations on metal atom adsorption and impurities on graphene [41, 182, 183, 184, 185, 186, 187] as stated in chapter 1. Metal-graphene interface is getting increasing attention in understanding the electronic transport through a graphene sheet [41, 188, 189, 190].

The research on interaction between adatoms, molecules and graphene are developing rapidly [43, 191, 192, 193, 194, 195, 196, 197, 198, 199]. This is important in controlling the modification of graphene [191].

H. Sevincli et al., [197] investigated electronic and magnetic properties of graphene and graphene nanoribbons functionalized by 3d transition-metal (TM) atoms. They found that binding energies of adsorbed TM atom depends on their species and coverage density. Graphene is found to become a magnetic metal after the adsorption of TM atoms.

K. T. Chan et al., [191] investigated the adsorption of twelve different metal adatoms on graphene by using DFT with the generalized gradient approximation (GGA). They investigated transition, noble, and group IV metals and found that the calculations are in agreement with covalent bonding, and strong hybridization between adatom and graphene.

The problem of gold atoms and dimers on the surface of graphene is investigated by

R. Varns and P. Strange [192] using DFT. They found that the gold-gold interaction is stronger than the gold-graphene interaction and the stable configuration of single gold atom is when Au is directly above a carbon atom. The dimer, on the other hand, is directly above a carbon-carbon bond.

G.M.Wang et al [200]., have investigated the interaction of deposited gold adatoms and dimers with multilayer relaxed graphite surfaces by using DFT with numerical orbitals and a relativistic core pseudopotential.

The adsorption of single Pt atom and Pt clusters on graphene and carbon nanotube is investigated by D.H.Chi et al [201]., by using DFT within GGA. They found that the Pt-Pt bond length and the charge transfer from Pt clusters to the nanotube change as a function of cluster size. The catalytic activities of Pt cluster adsorbed on the nanotube is found to be better than that of the free cluster.

Y.Okamoto [202] investigated Pt_{13} or Au_{13} cluster on graphene sheets and flakes by using DFT. It is found that the stability of the interface increases by introducing five- or seven-member rings into the graphene.

The cluster-graphene interface can be used to test our understanding of the fabrication of electronic devices [191, 192, 203].

We are especially interested in Au and Pt . Au has poorer catalytic properties than Pt . Au - Pt clusters show different catalytic and magnetic properties [106, 204]. To the best of our knowledge, there is no work on interaction between Au_nPt_n clusters and graphene surface up to $n=3$. Catalytic activity increases as the cluster size is getting smaller. This is why we calculate the adsorption of Au_nPt_n on graphene. In this work, adsorption energy, band structure, charge transfers, are investigated by using DFT within LDA and GGA. We have also included spin polarization in our calculation. We observe that Au_nPt_n adsorption on graphene influences the electronic structure drastically [3].

5.2.1 Computational Details

The total energy and electronic structure calculations are performed with (PWSCF) [15]. The kinetic energy cutoff of plane waves is taken as 612 eV. We have used the ultra-soft pseudopotentials within GGA (Perdew-Burke-Ernzerhof exchange -correlation (xc)) and LDA [64, 71, 109, 137]. The Brillouin-zone (BZ) sampling is done by using 9x9x1 grid of Monkhorst-Pack [161] special k points and using a Methfessel and Paxton method [162].

The structures investigated include a single graphene layer with (4x4) unit cell to minimize the interaction between clusters on repeating slabs and a Au_nPt_n cluster adsorbed at different sites on the surface. Firstly, we obtain the stable configurations of Au_nPt_n clusters in vacuum. We find similar structures for Au_nPt_n within GGA and LDA. Then, the adsorbate+graphene system is relaxed to equilibrium. The Hellmann-Feynman forces and conventional minimization techniques are used to determine the equilibrium structures. Hellmann-Feynman forces after the ionic relaxation, are smaller than 0.001 eV/Å.

The adsorption energy is calculated as

$$E_a = -(E_{gc} - E_g - E_c). \quad (5.1)$$

where, E_{gc}, E_g, E_c are energies of graphene-cluster, the free-standing graphene and the cluster, respectively. Convergence criteria of total energy between two self consistent field steps is taken to be 10^{-6} eV.

The charge difference is defined as;

$$\Delta\rho = \rho_{total} - \rho_{graphene} - \rho_{cluster}. \quad (5.2)$$

where ρ_{total} , $\rho_{graphene}$ and $\rho_{cluster}$ are the total charge on Au_nPt_n -graphene, graphene and the cluster or atom, respectively. We have also included the spin polarization into our calculations.

We have investigated the charge transfer by using the Löwdin analysis [3]. It is claimed that there are two charge transfer mechanisms. Firstly, it is the relative position of the HOMO and LUMO of the adsorbate with respect to Dirac point in pure graphene that determines the direction of charge transfer for paramagnetic adsorbates [178, 205, 198]. O. Leenaerts et al., [178] have shown that if the HOMO is above the Dirac point, there will be charge transfer to graphene. If the LUMO is below the Dirac point, there will be charge transfer to substrate. Secondly, the charge transfer could also be determined by using hybridization of the HOMO and LUMO with graphene orbitals. This orbital mixing with graphene orbitals results in effective charge transfer and it occurs for all adsorbates [205, 178, 198].

There are some computational problems in the calculation of charge transfer by DFT [198, 205]. O. Leenaerts et al., [198, 205] has shown that the charge transfer between paramagnetic molecules and graphene layer may crucially depend on the size of the supercell used in the calculation [3].

5.2.2 Electronic Properties of Au_nPt_n Clusters Adsorbed on Graphene

We consider three possible sites for each adsorbate, namely the top site (T) which is directly above a C -atom, the bridge site (B) at the midpoint of a C – C bond and hollow site (H) on the center of the hexagon.

We find that wherever we start, Au atom always end up at the T-site on graphene within LDA as seen in Fig. 5.3(a). Pt atom, on the other hand, prefers to stay on the B-site site as seen in Fig. 5.3(b) and Fig. 5.3(b) within LDA and GGA [3]. These results are in agreement with available literature [191, 192, 201].

The calculated binding energies, bond lengths and the charge transfer from the adsorbate to graphene are given in Table.5.1

As can be seen in Table.5.1. LDA binding energies are consistently larger than GGA ones. The corresponding bond lengths are therefore shorter for LDA. These results are in agreement with the available literature [192, 200]. Pt atom has higher adsorption

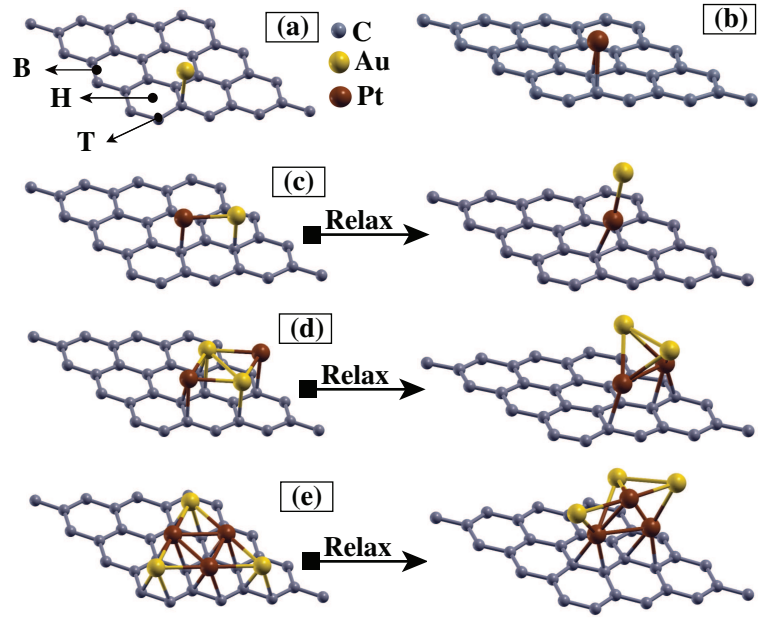


Figure 5.3: The Au_nPt_n -graphene structures within LDA. B: bridge site, H: hollow site and T: top site (a) the stable configuration of Au -graphene.(b) the stable configuration of Pt -graphene. (c) initial (left) and final (right) configurations of $AuPt$ -graphene. (d) initial (left) and final (right) configurations of Au_2Pt_2 -graphene. (e) initial (left) and final (right) configurations of Au_3Pt_3 -graphene [3].

energy than Au . The reason that Pt atom has large adsorption energy may be due the strong hybridization between Pt and adjacent C atoms [201]. As seen in Fig. 5.4(a) there is no chemisorption between Au and C atoms for Au -graphene within GGA. The initial configuration is given as B-site but after the interaction we observe that Au atom is moving up to a higher position as seen in Fig. 5.4 (a).

The charge differences are also as expected. There is a charge transfer from graphene to gold, whereas Pt is found to be a donor, transferring charge to the graphene in

Table 5.1: Au and Pt on graphene: the bond length (d) the adsorption energy (E_a) and the total charge transfer from the graphene to Au and from Pt to graphene for the most stable relaxed position calculated by using LDA and GGA [3].

Adsorbate/xc	Position	d(Å)	E_a (eV)	Total charge transfer(e)
Au/LDA	T	2.20	0.98	-0.19
Au/GGA	B	3.64	0.14	-0.20
Pt/LDA	B	2.06	2.74	0.14
Pt/GGA	B	2.10	2.17	0.08

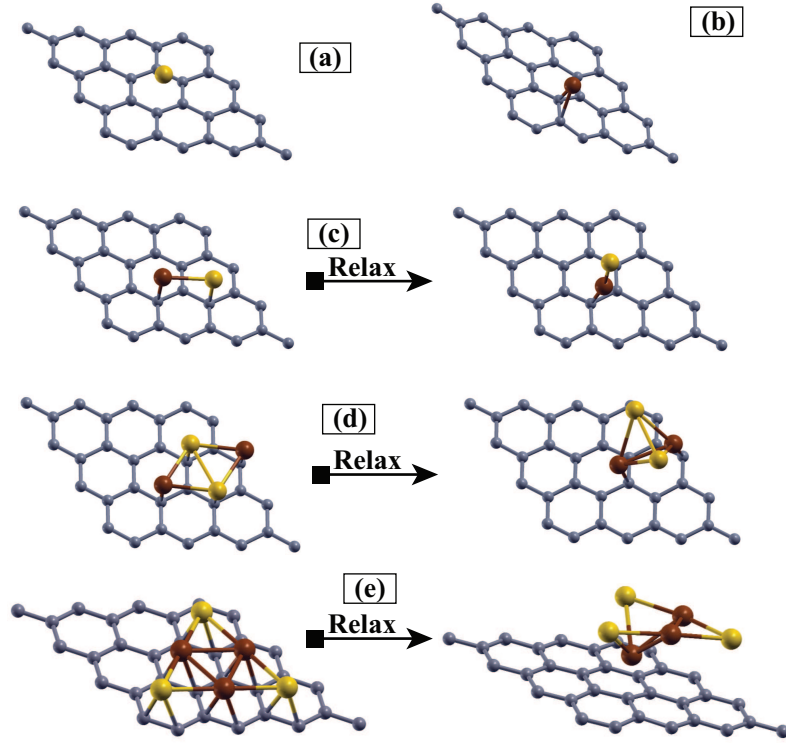


Figure 5.4: The Au_nPt_n -graphene structures within GGA. (a) the stable configuration of Au -graphene. (b) the stable configuration of Pt -graphene. (c) initial (left) and final (right) configurations of $AuPt$ -graphene. (d) initial (left) and final (right) configurations of Au_2Pt_2 -graphene. (e) initial (left) and final (right) configurations of Au_3Pt_3 -graphene. (f) initial (left) and final (right) configurations of Au_3Pt_3 -graphene [3].

agreement with available literature [192, 200, 201]. The charge transfer is shown in Fig. 5.5 and Fig. 5.6 in more detail. The negative regions in this figure correspond to decrease of charge from the vicinity. The spin polarized calculations yield lower binding energy for Au in LDA (0.50 eV). Total magnetization of the Pt -graphene (Au -graphene) the system is found as zero $\mu_B/cell$ ($0.82 \mu_B/cell$) for GGA.

The calculated binding energies, bond lengths, charge transfers and the magnetization of the adsorbed $AuPt$ are given in Table.5.2. There is a charge transfer from graphene to $AuPt$. Excess charge is more localized around the Au atom ($-0.26 e$). The accompanying magnetization to the charge transfer is calculated as $0.95 \mu_B/cell$.

The adsorption energy (bond length) are 1.96 eV, (2.12 Å) in LDA, 1.14 eV, (2.17 Å) in GGA.

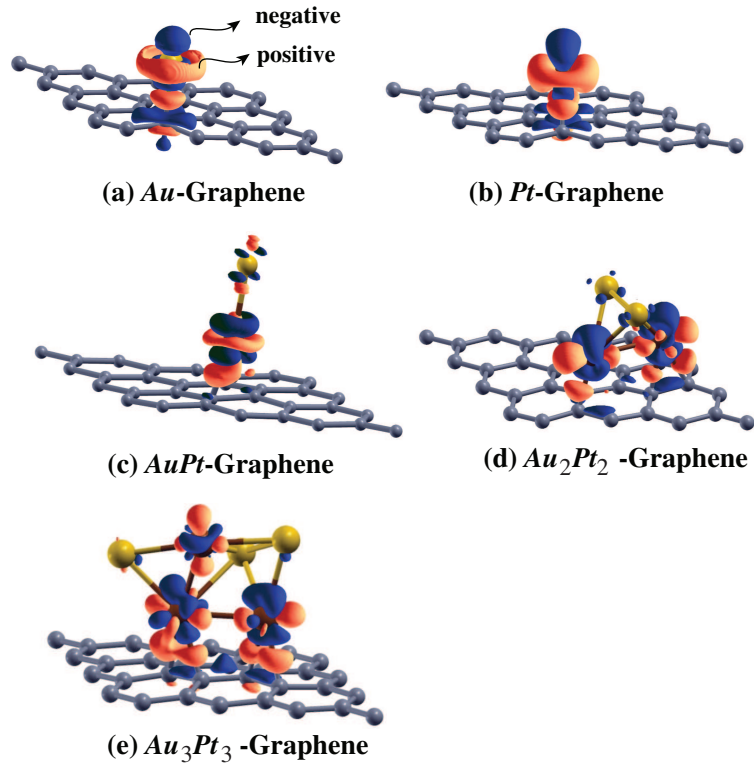


Figure 5.5: The charge differences between adsorbates and the graphene within LDA. The dark regions correspond to decrease in charge. The light regions correspond to increase in charge [3].

The starting position of *AuPt* cluster on graphene surface is taken as the T-site. The relaxed position in LDA (GGA) is shown in Fig. 5.3 (c) (Fig. 5.4(c)). As can be seen from these figures, *AuPt* cluster is shifted to a position in between T- and B-sites.

The charge differences for *AuPt*-graphene calculated within LDA is shown in Fig. 5.5 (c). It is clearly seen that *AuPt* receives some charge from graphene which is in line with our total charge transfer results.

Table 5.2: *AuPt* on graphene: the bond length (d) the adsorption energy (E_a) and the total charge transfer from the graphene to *AuPt* for the most stable relaxed position calculated by using LDA and GGA [3].

Adsorbate/xc	Position	d(Å)	E_a (eV)	Total charge transfer(e)
AuPt/LDA	T/B	2.12	1.96	-0.08
AuPt/GGA	T/B	2.17	1.14	-0.003

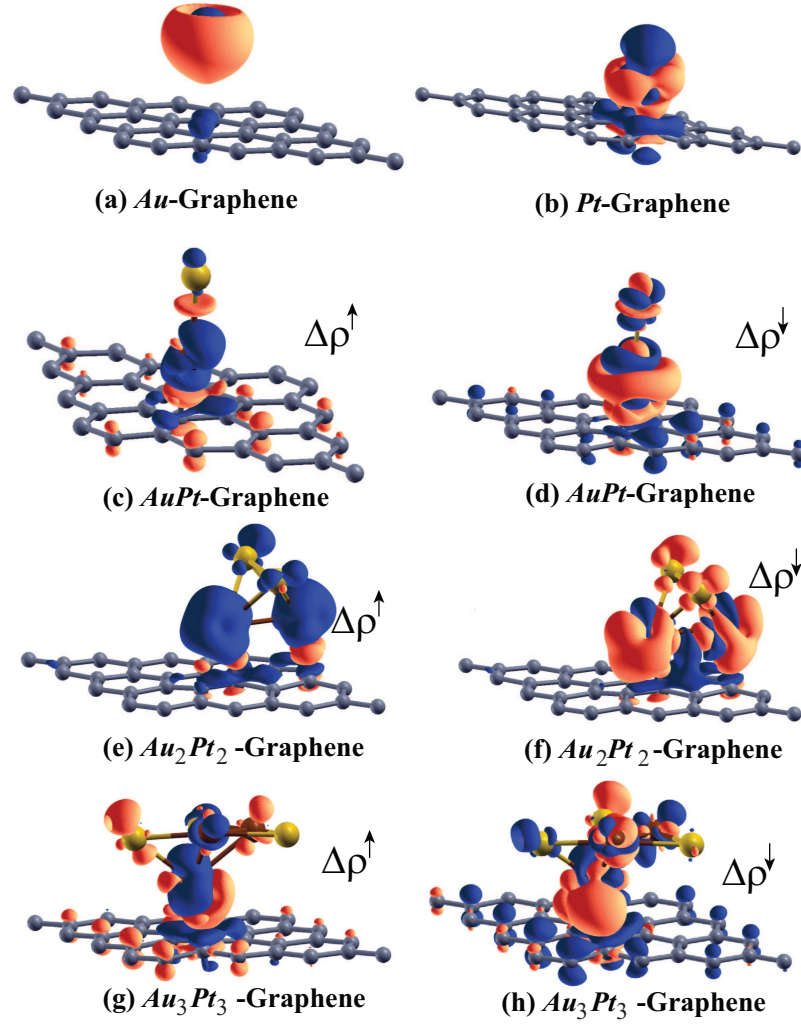


Figure 5.6: The charge differences between adsorbates and the graphene within GGA. The dark regions correspond to decrease in charge. The light regions correspond to increase in charge. The charge differences are decomposed into their spin components [3].

The spin polarized GGA results are shown in Fig. 5.6 (c) and Fig. 5.6 (d) for spin-up and spin-down states, respectively. These are similar to our LDA charge difference results.

There is also a charge transfer from *Pt* to *Au*, as can easily be seen in Fig. 5.6 (c) and Fig. 5.6 (d).

Our results for Au_2Pt_2 adsorbed on graphene are given in Table.5.3. For this case, charge is transferred from Au_2Pt_2 to the graphene. *Au* atom receive less charge (-0.18 (e)) than given by the *Pt* atoms (+0.49e).

Table 5.3: Au_2Pt_2 on graphene: the bond length (d) the adsorption energy (E_a) and the total charge transfer from the Au_2Pt_2 to graphene for the most stable relaxed position calculated by using LDA and GGA [3].

Adsorbate/xc	Position	d(Å)	E_a (eV)	Total charge transfer(e)
Au_2Pt_2 /LDA	T/B	2.15	3.20	0.31
Au_2Pt_2 /GGA	T/B	2.17	1.81	0.08

Table 5.4: Au_3Pt_3 on graphene: the bond length (d) the adsorption energy (E_a) the total charge transfer from the graphene to Au_3Pt_3 for the most stable relaxed position calculated by using LDA and GGA [3].

Adsorbate/xc	Position	d(Å)	E_a (eV)	Total charge transfer(e)
Au_3Pt_3 /LDA	T/B	2.15(av.)	3.61	-0.25
Au_3Pt_3 /GGA	T/B	3.89(av.)	0.54	-0.05

The relaxed position of Au_2Pt_2 within LDA (GGA) is given in Fig. 5.3 (d) (Fig. 5.4 (d)). The structure of cluster is modified from planar to 3D and shifted from T-site (GGA) (B-site (LDA)) to somewhere in between T-and B-sites.

The charge differences for Au_2Pt_2 -graphene calculated within LDA is shown in Fig. 5.5 (d). There is a charge transfer from Pt to graphene and also between interacting orbitals of Au and Pt. The spin polarized GGA results are shown in Fig. 5.6 (e) and Fig. 5.6 (f) for spin-up and spin-down states, respectively. These are similar to our LDA charge difference results.

Total magnetization of the system is found as $0.01 \mu_B/cell$

The calculated quantities for Au_3Pt_3 are given in Table.5.4. The charge is transferred form graphene to Au_3Pt_3 . Total magnetization of the system is found as $2.95 \mu_B/cell$.

The relaxed position of Au_3Pt_3 within LDA (GGA) is given in Fig. 5.3 (e) (Fig. 5.4 (e)). After the relaxation,the structure of cluster is modified from planar to 3D as seen in Fig. 5.3 (e) and Fig. 5.4 (e). GGA adsorption energy is much smaller than that in LDA and there is no chemical binding to the surface within GGA.

The charge transfer is similar to the case of $AuPt$ as can be seen in Fig. 5.5 (e) and Fig. 5.6 (g) and (h).

The interaction properties of the graphene and adsorbate that is summarized up to now may also be seen in the calculated band structures. LDA and GGA results are given in Fig. 5.7 and Fig. 5.8, respectively.

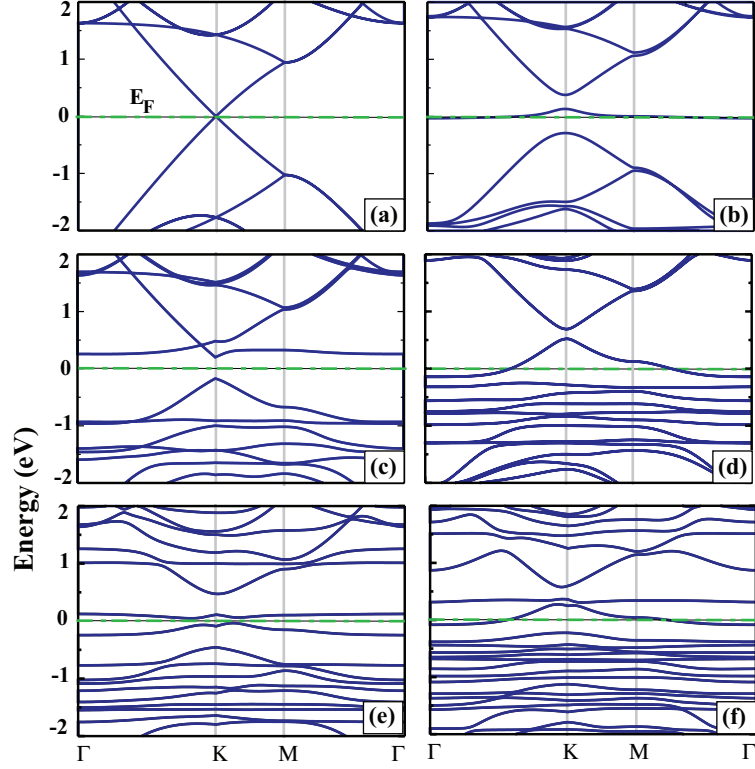


Figure 5.7: The Energy band structures within LDA; (Note that spin-up and spin-down bands overlap exactly in LDA)(a) graphene (b) *Au*-graphene, (c) *Pt*-graphene, (d) *AuPt*-graphene, (e) *Au₂Pt₂*-graphene, (f) *Au₃Pt₃*-graphene [3].

We observe that the band structure of bare graphene [35, 171, 197] and the charge transfer results for all the cases studied are in agreement with the available literature [192, 200, 201]. Charge transfer from graphene to cluster or atoms may make graphene metallic. We observe that there is a charge transfer from graphene to the adsorbed entity for *Au*, *AuPt*- and *Au₃Pt₃*. These results are in agreement with the available literature [192, 200]. We observe that GGA and LDA correctly predicts the

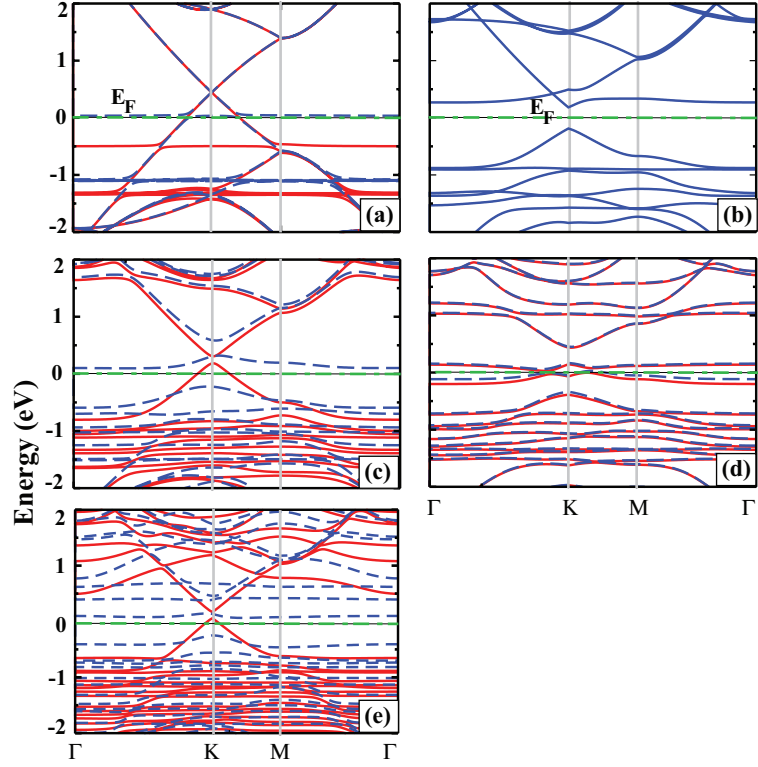


Figure 5.8: The Energy band structures within GGA (a) *Au*-graphene, (b) *Pt*-graphene (Note that spin-up and spin-down bands overlap exactly), (c) *AuPt*-graphene, (d) *Au₂Pt₂*-graphene, (e) *Au₃Pt₃*-graphene (line; spin up bands. Dashed line; spin down bands) [3].

direction of charge transfer between adsorbate and the graphene.

The bands are also decomposed into contributions by different spins. We find, for *AuPt*- and *Au₃Pt₃* -graphene within GGA, that while spin up bands show metallic properties, spin down bands show semiconducting properties. Thus, the corresponding systems show half metallic properties.

We note that the band structures around the Dirac point are affected by cluster adsorption on graphene. The presence of adsorbates results in flat, molecular -like levels around the Fermi energy. Usually, a small band gap opens. For *Au*, *AuPt* and *Au₃Pt₃*, electrons are transferred from the upper valance band of the graphene to the adsorbate so that the Fermi energy intersects the valence band. For *Pt* and *Au₂Pt₂*, electrons are given to the graphene which shifts the Fermi energy into the conduction band. The linear dispersion around the Fermi level seems to survive in cases *Au*, *AuPt*

and Au_2Pt_2 on graphene. This is equivalent to doping the graphene with donors and acceptors [3].

5.3 Bismuth Doping of Graphene

The development of graphene-based nano-electronics depends on our ability to dope this interesting material. The chemical doping or functionalization of graphene is usually done by adsorbing atoms and/or molecules on its surface [191, 197, 206, 207, 43]. n-type doping results if electrons are donated by the adsorbate to the graphene layer [42]. The alkali atoms, for example, are shown to release their valence electron rather easily and act as agents for n-doping of graphene, fullerenes and intercalation doping [42, 208, 209, 43].

Chemical p-type doping of graphene is known to be a real challenge [42]. For p-type doping of graphene, it is the graphene that has to donate electrons to the adsorbate. This is shown to be the case for very reactive and thus electronically unsuitable cases of molecules such as NO_2 , H_2O , NH_3 , H_2S and $F4-TCNQ$ [42, 179, 210, 211, 212]. The alternative candidates that have been investigated are heavier atoms such as *Bi*, *Sb*, *Au* and molecules such as N_2O_4 [42]. These are elements whose electron affinity is smaller than that of atomic carbon. We have shown earlier that *Au* and Au_3Pt_3 also have the ability for p-type doping of graphene but at the expense of heavily influencing its band structure [3].

Recently, I. Gierz et al., [42] have shown by angle-resolved photoemission spectroscopy that p-doping of epitaxial graphene on $4H-SiC$ (0001) is possible by the adsorption of *Bi*, *Sb* and *Au*. It is important to note that there is a basic difference between the free-standing and epitaxial graphene on *SiC* as far as doping is concerned. The epitaxial graphene is naturally n-doped by charge transfer from the substrate *SiC* [42]. I. Gierz et al. [42], have demonstrated that this naturally n-doping of epitaxial graphene can be turned into p-doping by *Bi*, *Sb*, and *Au*-adsorption without changing the essential conical band structure of graphene. The increasing amount of adsorbates shifted the Dirac point into the occupied states towards the Fermi level.

We aim to follow up this experimental work with a first principles DFT computation of the electronic structure of *Bi*-doped graphene. We investigate the adsorption of *Bi* and *Bi*₂ on free-standing graphene in more detail. We investigate also the substitutional doping of graphene by *Bi*. Our aim is to clearly identify the resulting effects of these both types of doping on the electronic structure of graphene. We find that the adsorbed *Bi* causes a weak p-type doping of graphene without causing a drastic change of pure graphene band structure within GGA. On the other hand, adsorbed *Bi* studied within LDA shows n-type doping and the calculated adsorption energy is bigger than that of GGA. Whereas, the substitutional *Bi* causes n-type doping at the expense of changing the band structure drastically [43].

5.3.1 Computational Details

Our calculations are performed using the PWSCF [15] within the generalized gradient approximation (GGA). We have also used the VASP [16, 17] within local density approximation (LDA). The kinetic energy cutoff of plane waves is taken as 816 eV within GGA. Ultra soft pseudopotentials (Perdew-Burke-Ernzerhof exchange-correlation and Rabe Rappe Kaxiras Joannopoulos [64] and Martins-Troullier [213]) are used within GGA. We use projector augmented wave (PAW) potentials [214] within LDA. The energy cut off is taken 450 eV within LDA. The Brillouin-zone(BZ) sampling is performed by using 9x9x1 grid of Monkhorst-Pack [161].

A single graphene layer with (4x4) unit cell is used in our calculations to minimize the interaction between substitutional atoms. *Bi* and *Bi*₂ per unit cell, as adsorbates and substitutional dopants on graphene are investigated. Firstly, The stable configuration of *Bi* and *Bi*₂ adsorption on graphene is found. The Hellmann-Feynman forces and conventional minimization techniques are used to determine the equilibrium structures. Hellmann-Feynman forces after the ionic relaxation, are smaller than 0.001 eV/Å. There exist a weak pressure on the unit cell. It is less than 0.5 kBar. A minimum of vacuum spacing is kept as 10 Å. The stable configurations of substitutional *Bi* and *Bi*₂ on graphene are obtained.

The adsorption energy [3] (E_a) and substitutional energy (E_{sub}) [206] are calculated as

$$E_a = -(E_{gb} - E_g - E_{bi}), \quad (5.3)$$

$$E_{sub} = -(E_{gs} - \frac{N-1}{N}E_g - E_{bi}). \quad (5.4)$$

where, E_{gb} , E_g , E_{bi} , E_{gs} , are energies of graphene+bismuth, the free-standing graphene and the bismuth, graphene+substitutional bismuth, respectively and N is the number of carbon atoms in the ideal graphene. Convergence criteria of total energy between two self consistent field steps is taken to be 10^{-6} eV.

The charge differences are calculated as follows;

$$\Delta\rho = \rho_{total} - \rho_{graphene} - \rho_{bi}. \quad (5.5)$$

where ρ_{total} , $\rho_{graphene}$ and ρ_{bi} are the total charge on Bi_n +graphene, graphene and the bismuth, respectively. The spin polarization is included into our calculations. The charge transfers are investigated using the Löwdin analysis [138] within GGA and Bader [215] method within LDA [43].

5.3.2 The Adsorption and Substitution and Electronic Properties of Bi and Bi_2 on Graphene

We consider three possible sites for bismuth, namely the top site (T) which is directly above a C -atom, the bridge site (B) at the midpoint of a $C-C$ bond and hollow site (H) on the center of the hexagon. We found that the final position of Bi atom and Bi_2 molecule are away from the graphene surface for all sites within GGA and there exists a small deformation on the graphene surface. The most stable sites are H-site for single Bi -atom within LDA. The total magnetization of Bi is $3.00 \mu_B/cell$. The C atoms which is under the Bi atoms move down, approximately by 0.07 \AA , the most stable site for Bi_2 -molecule is the B-site as seen in Fig.5.9(b). The Bi_2 moves up

from the B-site. We found two stable structures for substitutional Bi and Bi_2 within LDA, conf1 and conf2 as shown in Fig.5.9(c) and Fig.5.10 (a). While in conf1, they stay in plane, conf2 causes deformation on graphene surface, Bi moves up and Bi_2 moves down. Total magnetization for the substitutional case within LDA for conf2 is approximately zero.

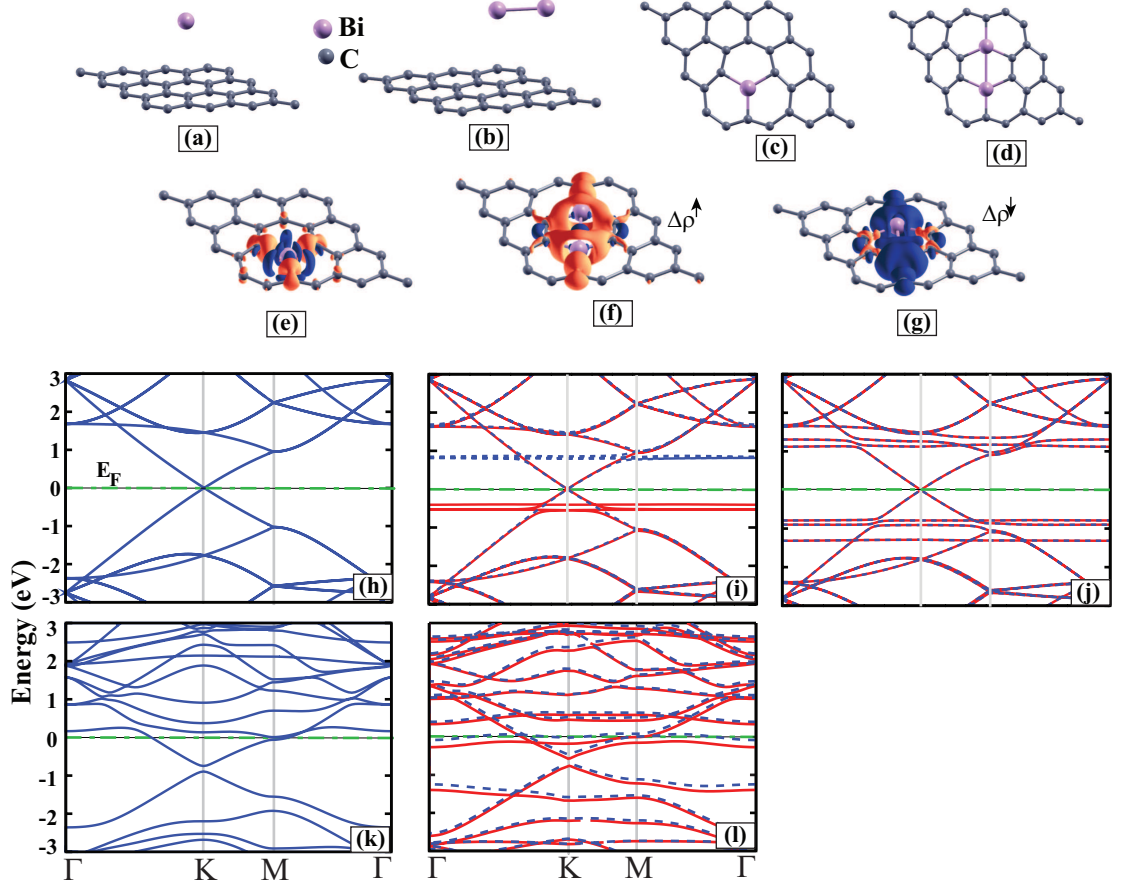


Figure 5.9: (a) The stable configuration of Bi on graphene within LDA, (b) The stable configuration of Bi_2 on graphene within LDA, (c) The stable configuration of substitutional Bi on graphene within GGA (conf1), (d) The stable configuration of substitutional Bi_2 on graphene within GGA, (e) The charge differences of substitutional Bi on graphene (The dark regions correspond to decrease in charge, the light regions correspond to increase in charge), (f) The charge differences of substitutional Bi_2 on graphene within spin up states, (g) The charge differences of substitutional Bi_2 on graphene within spin down states, (h) Energy band structure of bare graphene, (i) Energy band structure of graphene with Bi within LDA (line; spin-up bands. Dashed line; spin-down bands), (j) Energy band structure of graphene with Bi_2 within LDA, (k) Energy band structure of graphene with substitutional Bi within GGA, (l) Energy band structure of graphene with substitutional Bi_2 within GGA [43].

The lattice parameters, the calculated binding and substitutional energies, bond lengths

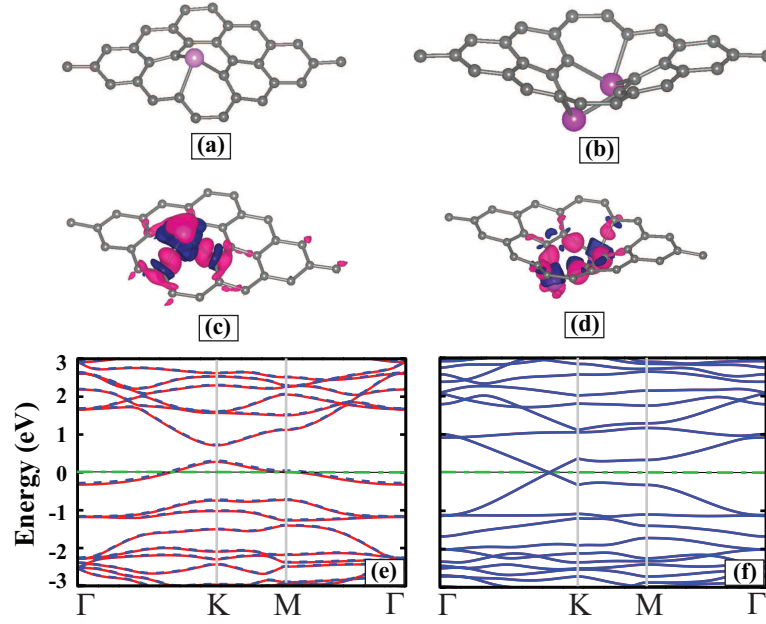


Figure 5.10: (a) The stable configuration of substitutional Bi on graphene within LDA (conf2), (b) The stable configuration of substitutional Bi_2 on graphene within LDA (c) The charge differences of substitutional Bi on graphene (The dark regions correspond to decrease in charge, the light regions correspond to increase in charge), (d) The charge differences of substitutional Bi_2 on graphene within LDA, (e) Energy band structure of graphene with substitutional Bi within LDA, (f) Energy band structure of graphene with substitutional Bi_2 within LDA [43].

and the charge transfer from the Bi_n to graphene are given within GGA and LDA in Table. 5.5 and Table. 5.6

We find that there is a weak binding between Bi and C atoms for Bi and Bi_2 on graphene within GGA. As seen in Table.5.5, LDA gives higher adsorption energy than that of GGA. As the number of Bi atom is increased, the adsorption energy increases. It is in agreement with experimental result [42]. Adding more atoms on the surface causes the cluster formation. We have calculated Bi per unit cell adsorption energy for 2×2 graphene surface within LDA. It is found as 0.17 eV. The pressure on the unit cell is so small that it is not required to expand it. On the other hand, we expand the unit cell to decrease the pressure for the substitutional case [43]. Bi - Bi bond length is in agreement with literature [216]. Substitutional energy for Bi and Bi_2 on graphene is given in Table.5.5. GGA results are in general agreement with LDA results for the substitutional case. The bond length between C - C near the Bi atom in Bi_2 -graphene is

Table 5.5: Bi_n on graphene: a lattice parameter, the adsorption energy E_a , substitutional energy E_{sub} and the charge transfer from the atom to graphene (+) , graphene to atom (-) for the most stable relaxed position [43].

	$a(\text{\AA})$	E_a or $E_{sub}(\text{eV})$	total charge transfer (e)
Bi/GGA	9.84	0.011	-0.04
Bi_2/GGA	9.84	0.036	-0.08
H-site (Bi)/LDA+PAW	9.79	0.15	0.07
B-site (Bi_2)/LDA+PAW	9.79	0.27	0.06
sub.1/GGA (conf1)	10.19	11.08	1.47
sub.2/GGA (conf1)	10.50	21.38	2.04
sub.1/LDA+PAW (conf1)	10.10	13.06	4.59
sub.1/LDA+PAW(conf2)	9.81	16.33	2.54
sub.2/LDA+PAW (conf1)	10.41	20.67	3.73
sub.2/LDA+PAW(conf2)	9.90	29.16	5.09

Table 5.6: Bond length for the most stable relaxed position [43].

	$d(\text{Bi-C}) (\text{\AA})$	$d(\text{Bi-Bi})(\text{\AA})$	$d(\text{C-C}) (\text{\AA})$
Bi/GGA	4.60	NA	1.42
Bi_2/GGA	4.59	2.68	1.42
H-site (Bi)/LDA+PAW	3.63	NA	1.42
B-site (Bi_2)/LDA+PAW	3.52	2.62	1.41
sub.1/GGA (conf1)	1.92	NA	1.40-1.47
sub.2/GGA (conf1)	1.98-2.00	2.99	1.36-1.51
sub.1/LDA+PAW (conf1)	1.89	NA	1.39-1.46
sub.1/LDA+PAW(conf2)	2.19- 3.08	NA	1.39-1.42
sub.2/LDA+PAW (conf1)	1.94-1.98	2.97	1.35-1.50
sub.2/LDA+PAW(conf2)	2.18-3.34	3.41	1.35-1.43

smaller than that of *Bi*-graphene. Thus, *Bi* atoms modify the structure of graphene but the shape remains two dimensional (2D) after substitutional doping as seen in Fig.5.9 (c). Total magnetization of the system is $0.60 \mu_B/\text{cell}$ for substitutional Bi_2 . Contrary to the case of adsorbed bismuth within GGA there is a charge transfer from *Bi* atoms to graphene within LDA for both adsorption and substitutional-doping. I.Gierz et al. [42], find that there is a charge transfer from graphene to bismuth atoms, of the amount of 0.01 (e) per *Bi* atom, this result is in agreement with our charge transfer results according to the Löwdin analysis.

We have also calculated the charge differences. For adsorption, charge transfer is extremely small within GGA. On the other hand, LDA gives bigger charge transfers. The charge transfer and the charge difference results are in agreement with each other as seen in Table.5.5. We observe that the charge difference results and band structures within LDA are in agreement with GGA results for the substitutional case. Therefore we give only the result for the substitutional *Bi* within GGA. As seen in Fig.5.9 (e), there is negative region on bismuth, that is, there exist charge transfer from *Bi* to *C* atom. There is also charge transfer between *C* atoms. For Bi_2 , the charge difference for spin up and spin down states are given in Fig.5.9 (f) and (g). There exists negative region between *Bi* atoms. There is a charge transfer from *Bi* to *C* atoms.

The calculated energy band structures are given in Fig.5.9(h)-(l) and Fig.5.10(e) and (f) . We observe that the band structure of bare graphene is in agreement with the literature [171, 35, 32]. The band structure within GGA is similar to that of LDA for adsorption. For brevity, we give the band structures within LDA only, for the adsorption. *Bi* and Bi_2 adatoms do not modify the graphene band structure much within LDA but it modifies the *Bi* related energy levels within the bands. Our result for adsorption is in agreement with the experimental result [42]. There exists a localized energy level of *Bi* near the Fermi energy as seen in Fig.5.9 (i) and (j). The spin up states overlap with spin down states in the band structure of single substitutional *Bi* in graphene and substitutional Bi_2 in graphene for conf2 within LDA . These states are separated for the Bi_2 case within conf1. Both systems show metallic property as shown in Fig.5.9 (k) and (l). But, Bi_2 substitutional, systems have semimetallic

properties although the band structure is modified for conf2 as shown in Fig.5.10 (f).

As far as the magnetic properties are concerned we note that for a strong impurity potential there would be localized states in the pseudogap around the Dirac point. A weak impurity potential may not lead to localized states. It is therefore necessary to have paramagnetic dopants for strong doping effects. Nonmagnetic dopants are expected to be weak in their doping effects. Diamagnetic Bi is not expected to be a strong dopant. This is what we observe for Bi and Bi_2 as adsorbates [43].

CHAPTER 6

CONCLUSION

We performed our calculation using the density functional theory (DFT) method. We see that DFT is successful to investigate such systems, as clusters, graphene, *Si* surface.

In chapter 3, we investigate the electronic properties of small Ag_n and Au_n up to eight atoms and NH_3 and H_2S adsorption on Au_3Pt_3 cluster [19, 24]. We obtain the stable structures of *Pt* and *Cu* clusters up to eight atoms. We determine the stable structures of these clusters and compare with the available experimental data.

Our results are in agreement with experimental data for the dimer of *Au* and *Ag*. We find that both *Ag* and *Au* clusters have planar structures. STM images and DOS are calculated for Ag_8 and Au_8 . For *Au* cluster, we see that there exists a hybridization in both DOS and STM and that covalent binding is more effective. For *Ag* clusters, s and d orbitals are involved in metallic binding which is more effective than covalent binding. We present for the first time normal mode of *Ag* and *Au* clusters, and this should be helpful in understanding of the elastical properties of clusters [19].

We investigated the site dependent electronic properties of $Au_3Pt_3-NH_3$ and $Au_3Pt_3-H_2S$. We have studied six adsorption sites. The results indicate generally that the electronic and geometrical factors are playing key roles for adsorption sites. Adsorption energies within GGA (LDA) are bigger for the sites H1 and H2 (T1 and T2) with higher coordination numbers for NH_3 . The bond lengths between the adsorbates and the *Pt* atom are the shortest. For H_2S , adsorption energies within GGA (LDA)

are bigger for the sites H1 and H2 (B2) with higher coordination numbers. The adsorption of H_2S to the B2 -site shows a totally different structure from others. H_2S dissociates at this site within LDA. We find that there is a strong interaction between Pt and N atoms and also between Pt and S atoms for the NH_3 and H_2S adsorption on Au_3Pt_3 cluster. Some of the configurations are modified after the interaction. The clusters transform from a planar to three dimensional structures for these sites. There is a charge transfer from the adsorbate to the Au_3Pt_3 cluster according to the Löwdin analysis. We see that total charge transfer and total magnetization values are closer to each other for all sites within GGA. LDA results give smaller total magnetization and bigger charge transfer than GGA. We have also calculated the energy levels for all configurations. We observe that the energy levels around the Fermi level correspond to charge distributions which are in agreement with the results of the Löwdin analysis. Comparing d and E_a for both adsorbates, we see that $Pt-N$ interaction is generally stronger than $Pt-S$ interaction, as a result of this, E_a in NH_3 adsorption (d) is bigger (smaller) than in H_2S adsorption, with the exception of B2- site within LDA [24].

In the chapter 4, we investigate the adsorption of Au_8 cluster onto H-terminated $Si(100):2\times 1$ asymmetric surface. We report the adsorption of Au_8 cluster on the $Si(100) (2\times 1)$ asymmetric surface by using the DFT. Electronic properties are investigated. We have shown that the electronic properties change with the location of Au_8 cluster. We tried four possible adsorption configurations. The geometry of Au_8 cluster is modified more for the top site. We see that the most preferable site is the P-configuration since the number of Au atoms interacting with surface is the biggest there. While for B-, T-, P-sites, these structures have semiconducting properties, for G-site, the structure has metallic properties. We investigate bands, charge transfer and charge densities. We find that GGA results are in agreement with LDA results. We show that the adsorption energy within LDA is bigger than that of GGA.

Adding more atoms requires more computing power. It may be interesting to study cluster-cluster interaction on the surface, if more Au clusters are adsorbed. There are also possible improvements to be made in handling the DFT. The relativistic corrections for Au may be included. Trends in physical properties, investigated in this

thesis, may be studied as one changes the number of atoms in the cluster [2].

In the chapter 5, adsorption of Au_nPt_n clusters on graphene surface and adsorption and substitutional Bi on graphene.

We have shown that the presence of Au_nPt_n clusters on graphene changes the electronic properties in an important way by using the first principles DFT-LDA/GGA method. In almost all cases we find moderate adsorption energies corresponding to physisorption. We find a downward shift of the Fermi level relative the Dirac point for Au , $AuPt$ and Au_3Pt_3 on graphene and upward shift for Au_2Pt_2 -graphene and Pt -graphene on graphene. We find, for $AuPt$ - and Au_3Pt_3 -graphene within GGA, that they show half metallic properties [3].

Molecular dynamics and Monte Carlo simulation approaches are also used to study the cluster-substrate interaction [219, 220, 221]. There are successful interatomic potentials, such as the quantum Sutton-Chen potentials [219] that enable researchers to investigate dynamic processes at the surface. The work of D.H. Seo et al [219], on the relative strength of interatomic bonding of Au and Pt on carbon nanotubes is in agreement with our work [3].

We have investigated the doping effects of Bi and Bi_2 in graphene both as adsorbates and as substitutional impurities. We have shown that Bi and Bi_2 change their local environment more when they are doped substitutionally. We found two stable structures for substitutional doping within LDA, conf1 and conf2. The electronic band structure of graphene is changed more drastically in this case. Substitutional Bi atom makes the system metallic. But, Bi_2 substitutional, system shows semimetallic properties although the band structure is modified for conf2. For adsorption, we observe that the adsorption energy within LDA is bigger than it is in GGA. When the number of Bi atoms is increased, the adsorption energy increases and Bi atoms tend to form clusters on the graphene surface.

Bi clusters may then be chemisorbed onto the graphene surface. But, we do not find chemisorption within both GGA and LDA for Bi and Bi_2 , though the absorption energy turns out to be larger in the case of stronger physisorption within LDA. In

the case of weak binding within GGA, it may be difficult to say something about the adsorption site since the binding energy comes out to be too small [43].

DFT is rather an efficient method to investigate these structures. Car-Parrinello method may be better for investigating these structures. But it requires more computer power and time. Although the band gaps are problematic in DFT, the trends may come out to be correct. DFT is rather efficient in finding different geometries. But finding different energies and bond lengths in LDA and GGA signals that energy results are questionable. The real values may be somewhere between the LDA and GGA results [3]. LDA and GGA are also known to be problematic for charge transfer studies [217, 218, 222]. This problem can only be handled if one goes beyond the simple first order approach [223].

The other disadvantage of DFT is that the induced dipole - dipole interaction can not be described properly in DFT (both GGA and LDA). When a molecule is chemically bound to a surface the effect of not describing the induced dipole - dipole interaction may often be ignored. It may be because of this that we do not observe chemisorption of *Bi* on graphene. A method which includes the van der Waals interaction may be useful for such a system [43].

REFERENCES

- [1] G. Cao, "Nanostructures and Nanomaterials, Synthesis, Properties and Applications", Imperial College Press, (2004).
- [2] O. Ü. Aktürk and M. Tomak, to be published Thin Solid Films.
- [3] O. Ü. Aktürk and M. Tomak, Phys. Rev. B **80** (2009) 085417.
- [4] K. Tanaka, Thin Solid Films **341** (1999) 120.
- [5] E. Kaxiras, "Atomic and Electronic Structure of Solids", Cambridge University Press (2003).
- [6] J. Kohanoff, "Electronic Structure Calculations for Solids and Molecules, Theory and Computational Methods", Cambridge University Press, (2006).
- [7] D. C. Rapaport, "The Art of Molecular Dynamics Simulation", Cambridge University Press, (2004).
- [8] A. R. Leach, "Molecular Modelling Principles And Applications", Longman, (1996).
- [9] M. C. Payne, M. P. Teter, D. C. Allan, T. A. Arias, J. D. Joannopoulos, Rev. Mod. Phys. **64** (1992) 4.
- [10] K. Burke and friends, "The ABC of DFT", (2007).
<http://chem.ps.uci.edu/kieron/dft/book/>, the last visited on, October (2009).
- [11] R. Car and M. Parrinello, Phys. Rev. Lett. **55** (1985) 2471.
- [12] M. Teter, P. M. C. Payne and D. C. Allan, Phys. Rev. B **40** (1989) 12255.
- [13] M. J. Gillan, J. Phys.: Condens. Matter **1** (1989) 689.
- [14] R. M. Martin, "Electronic Structure Basic Theory and Practical Methods", Cambridge University press, (2004).
- [15] S. Baroni, A. Dal Corso, S. de Gironcoli, P. Giannozzi, <http://www.pwscf.org>, the last visited on December (2009).
- [16] G. Kresse and J. Hafner, Phys. Rev. B **47** (1993) 558.
- [17] G. Kresse and J. Furthmüller, Phys. Rev. B **54** (1996) 11169.

- [18] H. M. Lee, M. Ge, B. R. Sahu, P. Tarakeshwar, and K. S. Kim, J. Phys. Chem. B **107** (2003) 9994.
- [19] O. Ü. Aktürk, O. Gülseren and M. Tomak, Int. J. Modern Phys. B **23** 31 (2009) 5819.
- [20] (a)V. B. Koutecky, L. Cespiva, P. Fantucci, J. Koutecky, J. Chem. Phys. **98** (1993) 7981 (b) V. B. Koutecky, L. Cespiva, P. Fantucci, J. Pitner, J. Koutecky, J. Chem. Phys. **100** (1994) 490.
- [21] (a) R. Fournier, J. Chem.Phys. **115** (2001) 2165 (b) K. A. Bosnick, T. L. Haslett, S. Fedrigo, M. Moskovits, W-T. Chan, R. Fournier, J. Chem. Phys. **111** (1999) 8867.
- [22] G. Bravo-Pérez, I. L. Garzón, O. Novaro J. Mol. Struct. (Theochem) **493** (1999) 225.
- [23] N. T. Wilson, R. L. Johnston, Eur. Phys. J. D **12** (2000) 161.
- [24] O. Ü. Aktürk and M. Tomak , submitted to Thin Solid Films.
- [25] G.J.-Jun, Y. J.-Xian, D. Dong, J. Mol. Struct. (Theochem) **764** (2006) 117121.
- [26] S. Konar, Bikash C. Gupta, and Inder P. Batra, Phys. Rev. B **77** (2008) 245411.
- [27] S. Hosoki, S. Hosaka, and T. Hasegawa, Appl. Surf. Sci. **60** (1992) 643.
- [28] M. F. Crommie, C. P. Lutz, and D. M. Eigler, Science **262** (1993) 218.
- [29] T.-C. Shen, C. Wang, G. C. Abeln, J. R. Tucker, J. W. Lyding, Ph. Avouris, and R. E. Walkup, Science, **268** (1995) 1590.
- [30] T.-C. Shen, C. Wang, and J. R. Tucker, Phys. Rev. Lett. **78** (1997) 1271.
- [31] B. Yoon, H. Häkkinen, U. Landman, A. S. Wörz, J. M. Antonietti, S. Abbet, K. Judai, and U. Heiz, Science A **307** (2005) 403.
- [32] A. H. Castro Neto, F. Guinea, N. M. R. Peres, K. S. Novoselov and A. K. Geim, Rev. Of. Modern. Phys., (2009) JANUARY-MARCH.
- [33] H. Zheng, Z. F.Wang, T. Luo, Q.W. Shi, and J. Chen, Phys. Rev. B **75** (2007) 165414.
- [34] K. S. Novoselov, A. K. Geim, S. V. Morozov, D. Jiang, Y. Zhang, S. V. Dubonos, I. V. Grigorieva, and A. A. Firsov, Science **306** (2004) 666.
- [35] A. K. Geim and K. S. Novoselov, Nat. Mater **6** (2007) 183.
- [36] K. S. Novoselov, D. Jiang, F. Schedin, T. J. Booth, V. V. Khotkevich, S. V. Morozov, and A. K. Geim, Proc. Natl. Acad. Sci. U.S.A. **102** (2005) 10451.

- [37] Y. Zhang, Y. W. Tan, H. L. Stormer, and P. Kim, *Nature (London)* **438** (2005) 201.
- [38] S. Stankovich, D. A. Dikin, G. H. B. Dommett, K. M. Kohlhaas, E. J. Zimney, E. A. Stach, R. D. Piner, SonBinh T. Nguyen, and Rodney S. Ruoff, *Nature (London)* **442** (2006) 282.
- [39] J. C. Meyer, A. K. Geim, M. I. Katsnelson, K. S. Novoselov, T. J. Booth, and S. Roth, *Nature (London)* **446** (2007) 60.
- [40] C. Berger, Z. Song, T. Li, X. Li, A. Y. Ogbazghi, R. Feng, Z. Dai, A. N. Marchenkov, E. H. Conrad, P. N. First, and W. A. de Heer, *J. Phys. Chem. B* **108** (2004) 19912.
- [41] G. Giovannetti, P. A. Khomyakov, G. Brocks, V. M. Karpan, J. van den Brink, and P. J. Kelly, *Phys. Rev. Lett.* **101** (2008) 026803.
- [42] I. Gierz, C. Riedl, U. Starke, C. R. Ast, *Nano Lett.* **8** (2008) 12 4603.
- [43] O. Ü. Aktürk and M. Tomak , submitted to *Appl. Phys. Lett.*
- [44] L. H. Thomas, *Proc. Cambridge Phil. Soc.* **23** (1927) 542.
- [45] E. Fermi, *Z. Phys.* **48** (1928) 73.
- [46] P. Hohenberg and W. Kohn, *Phys. Rev. B* **136** (1964) 864.
- [47] N. D. Mermin, *Phys. Rev. A* **137** (1965) 1441.
- [48] W. Kohn and L. J. Sham, *Phys. Rev. A* **140** (1965) 1133.
- [49] P. Giannozzi, *Metodi Numerici in Struttura Elettronica*, Anno accademico (2007-2008), <http://www.quantum-espresso.org/wiki/index.php/MethodologicalBackground>, the last visited on December (2009).
- [50] V. Fock, *Z. Phys* **61** (1930) 126.
- [51] J.C. Slater, *Phys.Rev.* **32** (1930) 339.
- [52] P. A. M. Dirac, *Proc. Cambridge Phil. Roy. Soc.*,**26** (1930) 376.
- [53] J. C. Slater, *Phys. Rev.* **81** (1951) 385.
- [54] E. P. Wigner, *Trans. Faraday Soc.* **34** (1938) 678.
- [55] E. Teller, *Rev. Mod. Phys.* **34** (1962)627.
- [56] M. Springborg, "Density Functional Methods in Chemistry and Materials Science", John Willey and Sons, (1997).

- [57] J. Thijssen, "Computational Physics", Cambridge University Press, (2007).
- [58] J. P. Perdew and Y. Wang, Phys. Rev. B **33** (1986) 8800.
- [59] J. P. Perdew, Phys. Rev. B **33** (1986) 8822.
- [60] Y. Wang and J. Perdew, Phys.Rev. B **44** (1991) 13298.
- [61] A. D. Becke, Phys. Rev. A **38** (1988) 3098.
- [62] C. Lee, W. Yang, R. G. Parr, Phys.Rev.B **37** (1988) 785.
- [63] J. P. Perdew, K. Burke, and M. Enzozhof, Phys. Rev. Lett. **77** (1996) 3865.
- [64] J. P. Perdew, K. Burke, and M. Enzozhof, Phys. Rev. Lett. **78** (1997) 1396.
- [65] C. Lee, W. Yang, R. G. Parr, Phys. Rev. B **37** (1988) 785.
- [66] R. Colle and D. Salvetti, Theor. Chim. Acta **37** (1975) (329).
- [67] J. P. Perdew and Y. Wang, Phys. Rev. B **45** (1992) 13244.
- [68] J. P. Perdew and Y. Wang, Phys. Rev. B **46** (1992) 12947.
- [69] <http://en.wikipedia.org/wiki/Pseudopotential>, the last visited on: December (2009).
- [70] D. R. Hamann, M. Schlüter, and C. Chiang, Phys. Rev. Lett. **43** (1979) 1494.
- [71] D. Vanderbilt, Phys. Rev. B **41** (1990) 7892.
- [72] J. A. Alonso, Chem. Rev. **100** (2000) 637.
- [73] P. B. Balbuena, P. A. Derosa and J. M. Seminario, J. Phys. Chem. B **103** (1999) 2830.
- [74] L. Xio and L. Wang, J. Phys. Chem. A **108** (2004) 8605.
- [75] K. A. Jackson, Phys. Rev. B **47** (1992) 9715.
- [76] H. Grönbeck and P. Broqvist, Phys. Rev. B **71** (2005) 073408.
- [77] V. G. Grigoryan, D. Alamanova and M. Springborg, Eur. Phys. J. D. **34** (2005) 187.
- [78] U. Lammers and G. Borstel, Phys. Rev. B **49** (1993) 17360.
- [79] S. H. Yang, D. A. Drabold, J. B. Adams, P. Ordejón and K. Glassford, J. Phys.: Condens. Matter **9** (1997) L39.
- [80] T. Li and P. B. Balbuena, J. Phys. Chem. B **105** (2001) 9943.

- [81] (a) V. B. Koutecky, L. Cespiva, P. Fantucci, J. Koutecky, *J. Chem. Phys.* **98** (1993) 7981 (b) V. B. Koutecky, L. Cespiva, P. Fantucci, J. Pitner, J. Koutecky, *J. Chem. Phys.* **100** (1994) 490.
- [82] (a) R. Fournier, *J. Chem. Phys.* **115** (2001) 2165 (b) K. A. Bosnick, T. L. Haslett, S. Fedrigo, M. Moskovits, W-T. Chan, R. Fournier, *J. Chem. Phys.* **111** (1999) 8867.
- [83] G. Bravo-Pérez, I. L. Garzón, O. Novaro *J. Mol. Struct. (Theochem)* **493** (1999) 225.
- [84] H. M. Lee, M. Ge, B. R. Sahu, P. Tarakeshwar, and K. S. Kim, *J. Phys. Chem. B* **107** (2003) 9994.
- [85] N. T. Wilson, R. L. Johnston, *Eur. Phys. J. D* **12** (2000) 161.
- [86] H. Häkkinen, U. Landman, *Phys. Rev. B* **62** (2000) R2287.
- [87] J. Wang, G. Wang, J. Zhao, *Phys. Rev. B* **66** (2002) 35418.
- [88] R. M. Olson, S. VARGANOV and et al., *J. Am. Chem. Soc.* **127** (2005)
- [89] J. R. Lombardi, B. Davis, *Chem. Rev.* **102** (2002) 2431.
- [90] E. M. Fernández, J. M. Soler, I. L. Garzón and L. C. Balbás, *Phys. Rev. B* **70** (2004) 165403.
- [91] D. Sánchez-Portal, E. Artacho, J. Junquera, P. Ordejón, A. Garcia and J. M. Soler, *Phys. Rev. Lett.* **83** (1999) 19.
- [92] S. Chilukuri, T. Joseph, S. Malwadkar, C. Damle, S. B. Halligudi, B. S. Rao, M. Sastry , and P. Ratnasamy, *Stud. Surf. Sci. Catal.* **146** (2003) 573.
- [93] B. D. Chandler , A. B. Schobel, L. H. Pignolet *J. Catal.* **193** (2000) 186.
- [94] A. M. Joshi, M. H. Tucker, W. Nicholas Delgass, and K. T. Thomson, *J. Chem. Phys.* **125** (2006) 194707.
- [95] M. M. Sadek, L. Wang, *J. Phys. Chem. A* **110** (2006) 14036.
- [96] L. Wang, *Chem. Phys. Lett.* **443** (2007) 304.
- [97] C. Song, Q. Ge and L. Wang, *J. Phys. Chem.* **109** (2005) 22341.
- [98] C. Mihut, C. Descorne, D. Duprez, M. D. Amiridis, *J. Catal.* **212** (2002) 125.
- [99] J. Luo, M. M. Maye, N. N. Kariuki, L. Wang, P. Njoki, Y. Lin, M. Schadt, H. R. Naslund, C. -J. Zhong, *Catal. Today*, **99** (2005) 291.

- [100] Y. B. Luo, M. M. Maye, L. Han, J. Luo and C. J. Zhong, Chem. Commun. **473** (2001).
- [101] W. Q. Tian, M. Ge, F. Gu, T. Yamada, and Y. Aoki, J. Phys. Chem. A **110** (2006) 6285.
- [102] R. Esparza, G. Rosas, F. Valenzuela, S. A. Gamboa, U. Pal, R. Pérez, Revista Matéria **13** (2008)n. 4, pp. 579 – 586.
- [103] H.M. Chen, H.-C. Peng , R.S. Liu, S.F. Hu b, L.-Y. Jang, Chem. Phys. Lett. **420** (2006) 484.
- [104] D. Mott, J. Luo, A. Smith, P. N. Njoki, L. Wang, C.-J. Zhong, Nanoscale Res. Lett. **2** : 12 – 16, (2007) DOI 10.1007/s11671-006-9022-8 .
- [105] D. W. Yuan, Y. Wang, and Z.Zeng, J.Chem. Phy. **122** (2005) 114310.
- [106] A. Cruz, E. Poulain, G. D. Angel, S. Castillo, V. Bertin, Int.J. Quantum Chem. **67** (1998) 6 399.
- [107] H. Tada, F. Suzuki, S. Ito, T. Kawahara, T. Akita, K. Tanaka, and H. Kobayashi, Chem. Phys. Chem. **7** (2002) 1439.
- [108] O. O. -Neria, A. Cruz, H. Luna-García, A. A.-García, E. Poulain, and S. Castillo, J. Chem. Phys, **123** (2005) 164302.
- [109] J. P. Perdew and A. Zunger, Phys. Rev.B **23** (1981) 5048.
- [110] J. Tersoff and D. R. Hamann, Phys. Rev. B **31** (1985) 2.
- [111] A. D. Corso, A. Pasquarello, and A. Baldereschi, Phys. Rev. B **56** (1997) R11369.
- [112] S. Baroni, P. Giannozzi, and A. Testa, Phys. Rev. Lett. **58** (1987) 1861.
- [113] P. Giannozzi, S. de Gironcoli, P. Pavone, and S. Baroni, Phys. Rev. B **43** (1991) 7231.
- [114] S. K. Gupta, B. M. Nappi, K. A. Gingerich, Inorg. Chem. **20** (1981) 966.
- [115] M. D. Morse, Chem. Rev. (Washington, D.C.) **86** (1986) 1049.
- [116] B. H. Billings and D. E. Gray, "American Institute of Physics Handbook", 3rd ed.(McGraw-Hill, New York, (1972).
- [117] B. Simard and P. Hackett, J. Mol. Spec. **142** (1990) 310.
- [118] A. Kokalj, Comp. Mat. Sci. **28** (2003) 155. <www.xcrysden.org>, the last visited on December 2009.

- [119] J. Oviedo, R. E. Palmer J. Chem. Phys. **117** (2002) 9548.
- [120] A. V. Walker, J. Chem. Phys. **122** (2005) 094310.
- [121] G. Bravo-Pérez, I.L. Garzón, O. Novaro J. Mol. Struct. (Theochem) **493** (1999) 225.
- [122] X. Gu, M. Ji, S. H. Wei and X. G. Gong, Phys. Rev. B **70** (2004) 205401.
- [123] K. Hilpert and K. A. Gingerich, Ber. Bunsenges., Phys. Chem. **84** (1980) 739.
- [124] D. Dai and K. Balasubramanian, J. Chem. Phys. **100** (1994) 4401.
- [125] E. Kooi, J. G. Vanlierop, J. A. Appels, J. Electrochem. Soc. **123** (1976) 117.
- [126] J. W. Osenbach, J. Appl. Phys. **63** (1988) 4494.
- [127] Y. Ma, T. Yasuda, G. Lucowsky, J. Vac. Sci. Technol. **B11** (1993) 1533.
- [128] N. López, M. García-Mota, and J. G.-Díaz, J. Phys. Chem. C **112** (2008) 247.
- [129] F. A. Pedersen, J. Greeley, F. Studt, J. Rossmeisl, T. R. Munter, P. G. Moses, E. Skulason, T. Bligaard, J. K. Nørskov, Phys. Rev. Lett. **99** (2007) 016105.
- [130] C. J. Westrate, J. W. Bakker, E. D. L. Rienks, J. R. Martinez, C. P. Vinod, S. Lizzit, L. Petaccia, A. Baraldi, B. E. Nieuvenhuys, J. Catal. **235** (2005) 92.
- [131] J. M. Bradley, A. Hopkinson, D. A. King, J. Phys. Chem. **99** (1995) 17032.
- [132] M. Kim, S. J. Pratt, D. A. King, J. Am. Chem. Soc. **122** (2000) 2409.
- [133] B. Lescop, A. Galtayries, G. Fanjoux, J. Phys. Chem. B **108** (2004) 13711.
- [134] J. C. Ganley, F. S. Thomas, E. G. Seebaner, R. I. Masel, Catal. Lett. **96** (2004) 117.
- [135] S. H. Israni, B. K. R. Nair, M. P. Harold, Catal. Today **139** (2009) 299.
- [136] D. R. Alfonso, Surf. Science **602** (2008) 2758.
- [137] A. M. Rappe, K. M. Rabe, E. Kaxiras and J. D. Joannopoulos, Phys. Rev. B **41** (1990) 1227.
- [138] P. O. Lowdin, J. Chem. Phys. **18** (1950) 365.
- [139] E. S. Dy and H. Kasai, e-J. Surf. Sci. Nanotech. **3** (2005) 473.
- [140] S. Hou, J. Zhang, R. Li, J. Ning, R. Han, Z. Shen, X. Zhao, Z. Xue and Q. Wu, Nanotechnology **16** (2005) 239.
- [141] E. S. Kryachko and F. Remacle, J. Chem. Phys. **127** (2007) 194305.

- [142] M. S. Hussain and E. O. Schlemper, *Acta Cryst.* **C43** (1987) 450.
- [143] V. V. Gritsenko, O. A. Dyachenko, P. Cassoux, A. L Kotov, E. E. Laukhina, C. Faulmann, and E. B. Yagubskii, *Russian Chemical Bulletin* **42** (1993) 7.
- [144] M. K. Oudenhuijzen, J. H. Bitter, and D. C. Koningsberger, *J. Phys. Chem. B* **105** (2001) 4616.
- [145] L. J. Brillson, "In Contacts to Semiconductors", (Noyes Publications:Park Ridge, New Jersey. p.245, 1993).
- [146] S. S. Cohen, and G. S. Gildenblat, eds. *VLSI Electronics:Microstructure Science*. Vol. **13**, Academic Press:Orlando (1986).
- [147] L. Ma, J. Wang, S. Wei, G. Wang, *Vacuum* **77** (2005) 337.
- [148] A. S. Foster, M. A. Gosálvez, T. Hynninen, R. M. Nieminen, and K. Sato, *Phys. Rev. B* **76** (2007) 075315.
- [149] L. Pirolli, A.V. Teplyakov, *Surf. Sci.* **600** (2006) 3313.
- [150] L. Y. Zhao, K. R. Eldridge, K. Sukhija, H. Jalili, N. F. Heinig, and K. T. Leunga, *Appl. Phys. Lett.* **88** (2006) 033111.
- [151] A. M. Mazzone, *Eur. Phys. J. B* **35** (2003) 517.
- [152] J. Mach, J. Čechal, M. Kolíbal, M. Potoček, T. Šikola, *Surf. Sci.* **602** (2008) 1898.
- [153] G. Lee, C. G. Hwang, N. D. Kim, J. Chung and J. S. Kim, S. Lee, *Phys. Rev. B* **76** (2007) 245409.
- [154] L. Zhang, Y. Kim, H. Shim, and G. Lee, *J. Phys.: Condens. Matter* **19** (2007) 486004.
- [155] L. Zhao, A. C.-L. Siu, J. A. Petrus, Z. He, and K. T. Leung, *J. Am. Chem. Soc.* **129** (2007) 5730.
- [156] L-L. Wang, S. V. Khare, V Chirita, D. D. Johnson, Angus A. Rockett, Anatoly I. Frenkel, Nathan H. Mack, and Ralph G. Nuzzo, *J. Am. Chem. Soc.* **128** (2006) 131.
- [157] C. Xirouchaki and R. E. Palmer, *Vacuum* **66** (2002) 167.
- [158] R. J. Baierle, M. J. Caldas, E. Molinari, and S. Ossicini, *Solid State Commun.* **102** (1997) 545.
- [159] I. Vasiliev, J. R. Chelikowsky, and R. M. Martin, *Phys. Rev.B* **65** (2002) 121302(R).

- [160] A. Ramstad, G. Brocks, and P. J. Kelly, Phys. Rev. B **51** (1995) 14504.
- [161] H. J. Monkhorst, J. D. Pack, Phys. Rev. B **13** (1976) 5188.
- [162] M. Methfessel, A. T. Paxton, Phys. Rev. B **40** (1989) 3616.
- [163] U. von Barth and R. Car unpublished; for a brief description of this method, see A. Dal Corso, S. Baroni, R. Resta, and S. de Gironcoli, Phys. Rev. B **47** (1993) 3588.
- [164] R. Hull and J. C. Bean, "Germanium Silicon: Physics and Materials", Academic Press, (1999).
- [165] A. Nilsson, L. G. M. Pettersson and J. K. Nørskov, "Chemical Binding Surfaces and Interfaces", Elsevier, (2008).
- [166] K. S. Novoselov, E. McCann, S. V. Morozov, V. I. Falko, M. I. Katsnelson, U. Zeitler, D. Jiang, F. Schedin, and A. K. Geim, Nat. Phys. **2** 177 (2006).
- [167] S. V. Morozov, K. S. Novoselov, M. I. Katsnelson, F. Schedin, L. A. Ponomarenko, D. Jiang, and A. K. Geim, Phys. Rev. Lett. **97** 016801 (2006).
- [168] P. M. Ostrovsky, I. V. Gornyi, and A. D. Mirlin, Phys. Rev. **B 74** 235443 (2006).
- [169] M. I. Katsnelson, Materials today **10** (2007) 1.
- [170] C. Berger, Z. Song, X. Li, X. Wu, N. Brown, C. Naud, D. Mayou, T. Li, J. Hass, A. N. Marchenkov, E. H. Conrad, P. N. First, W. A. de Heer, Science **312** (2006) 1191.
- [171] C. Ataca, E. Aktürk, S. Ciraci, and H. Ustunel, Appl. Phys. Lett. **93** (2008) 043123.
- [172] C. Ataca, E. Aktürk, and S. Ciraci, Phys. Rev. B **79** (2009) 041406(R).
- [173] I. Cabriaa, and M. J. López, J. A. Alonso, J. of Chem. Phys. **123** (2005) 204721.
- [174] L. A. Chernozatonskiia, P. B. Sorokinb, J. W. Brüning, Appl. Phys. Lett. **91**(2007) 183103.
- [175] Y. Miura, H. Kasai, W. Diño, and H. Nakanishi, T. Sugimoto, J. of Appl. Phys. **93** (2003) 6.
- [176] D. W. Boukhvalov, M. I. Katsnelson, A. I. Lichtenstein, Phys. Rev. B **77** (2008) 035427.
- [177] J. O. Sofo, Ajay S. Chaudhari, and Greg D. Barber, Phys. Rev. B **75** (2007) 153401.

- [178] O. Leenaerts, B. Partoens, and F. M. Peeters, Phys. Rev. B **77** (2008) 125416 .
- [179] E. H. Hwang, S. Adam, and S. Das Sarma, Phys. Rev. B **76** (2007) 195421.
- [180] E. W. Hill, A. K. Geim, K. Novoselov, F. Schedin, and P. Blake, IEEE Trans. Mag. **42** (2006) 2694.
- [181] N. Tombros, C. Jozsa, M. Popinciuc, H. T. Jonkman and B. J. van Wees, Nature Lett. **448**(2007) doi:10.1038/nature06037 .
- [182] C. Oshima and A. Nagashimaz, J. Phys.: Condens. Matter **9** (1997) 1.
- [183] Yu. S. Dedkov, A. M. Shikin, V. K. Adamchuk, S. L. Molodtsov and C. Laubschat, A. Bauer and G. Kaindl, Phys. Rev. B **64** (2001) 035405.
- [184] G. Giovannetti, P. A. Khomyakov, G. Brocks, P. J. Kelly, and J. van den Brink, Phys. Rev. B **76** (2007) 073103.
- [185] B. Uchoa, C.-Y. Lin, and A. H. Castro Neto, Phys. Rev. B **77** (2008) 035420 .
- [186] A. V. Krasheninnikov, P. O. Lehtinen, A. S. Foster, P. Pyykkö and R. M. Nieminen, Phys. Rev. Lett. **102** (2009) 126807.
- [187] M. Wu, E.-Z. Liu, M. Y. Ge and J. Z. Jiang, Appl. Phys. Lett. **94** (2009) 102505.
- [188] K. S. Novoselov, A. K. Geim, S. V. Morozov, D. Jiang, M. I. Katsnelson, I. V. Grigorieva, S. V. Dubonos, A. A. Firsov, Nature Lett. **438** (2005) 10.
- [189] V. M. Karpan, G. Giovannetti, P. A. Khomyakov, M. Talanana, A. A. Starikov, M. Zwierzycki, J. van den Brink, G. Brocks, and P. J. Kelly, Phys. Rev.Lett. **99** (2007) 176602.
- [190] Ya. M. Blanter, I. Martin, Phys. Rev. B **76** (2007) 155433.
- [191] K. T. Chan, J. B. Neaton, and M. L. Cohen, Phys. Rev. B **77** (2008) 235430.
- [192] R. Varns and P. Strange, J. Phys.: Condens. Matter **20** (2008) 225005 (8pp).
- [193] Y. Mao, J. Yuan and J. Zhong, J. Phys.: Condens. Matter **20** (2008) 115209 (6pp).
- [194] P. O. Lehtinen, A. S. Foster, A. Ayuela, A. Krasheninnikov, K. Nordlund, and R. M. Nieminen, Phys. Rev. Lett. **91**(2003) 017202.
- [195] S. D. Chakarova-Käck, E. Schröder, B. I. Lundqvist, and D. C. Langreth, Phys. Rev. Lett. **96** (2006) 146107.
- [196] A. Ishii, M. Yamamoto, H. Asano and K. Fujiwara, Journal of Physics: Conference Series **100** (2008) 052087.

- [197] H. Sevinçli, M. Topsakal, E. Durgun, and S. Ciraci, Phys. Rev. B **77** (2008) 195434.
- [198] O. Leenaerts, B. Partoens, F. M. Peeters, Microelectronics Journal **40** (2009) 860.
- [199] H. Şahin and R. T. Senger, Phys. Rev. B **78** (2008) 205423.
- [200] G. M. Wang, J. J. BelBruno, S. D. Kenny, and R. Smith, Phys. Rev. B **69** (2004) 195412.
- [201] D. H. Chi, N. T. Cuong, N. A. Tuan, Y.-T. Kim, H. T. Bao, T. Mitani, T. Ozaki, H. Nagao, Chem. Phys. Lett. **432** (2006) 213.
- [202] Y. Okamoto, Chem. Phys. Lett. **420** (2006) 382.
- [203] G. Jian-Jun, Y. Ji-Xian, D. Dong, J. Mol. Struct: Theochem **764** (2006) 117.
- [204] J. Schwank, K. Balakrishnan, and A. Sachdev., Proc. 10th Intern. Congress on Catalysis, Hungary, **905** (1992).
- [205] O. Leenaerts, B. Partoens, and F. M. Peeters, Appl. Phys. Lett. **93** (2008) 193107.
- [206] R. Singh and P. Kroll, J. Phys.: Condens. Matter **21** (2009) 196002 (7pp).
- [207] E. J. Santos, A. Ayuela, S. B. Fagan, J. M. Filho, D. L. Azevedo, Phys. Rev. B **78** (2008) 195420.
- [208] A. Bostwick, T. Ohta, T. Seyller, K. Horn, E. Rotenberg, Nat. Phys. **3** (2007) 36.
- [209] T. Ohta, A. Bostwick, T. Seyller, K. Horn, E. Rotenberg, Science **313** (2006) 951.
- [210] W. Chen, S. Chen, D. C. Qui, X.Y. Gao, A. T. S. Wee, J. Am. Chem. Soc. **129** (2009) 10419.
- [211] T. O. Wehling, K. S. Novoselov, S. V. Morozov, E.E. Vdovin, M.I. Katsnelson, A.K. Geim, A.I. Lichtenstein, Nano Lett. **8** (2008) 173.
- [212] S. Y. Zhou, D. A. Siegel, A. V. Fedorov, A. Lanzara, Phys. Rev. Lett. **101** (2008) 086402.
- [213] N. J. Troullier and J. L. Martins, Phys. Rev. B **43** (1991) 3.
- [214] P. E. Blöchl, Phys. Rev. B **50** (1994) 17953.
- [215] G. Henkelman, A. Arnaldsson, and H. Jonsson, Comput. Mater. Sci. **36** (2006) 354.

- [216] N. Tokitoh, Y. Arai, R. Okazaki, S. Nagase, *Science* **277** (1997) 78.
- [217] C. Toher, A. Filippetti, S. Sanvito, K. Burke, *Phys. Rev. Lett.* **95** (2005) 146402.
- [218] S. -H. Ke, H. U. Baranger, W. Yang, *J. Chem. Phys.* **126** (2007) 201102.
- [219] D. H. Seo, H. Y. Kim, J. H. Ryu, and H. M. Lee, *J. Phys. Chem. C* **113** (2009) 10416.
- [220] V. V. Barkaline, A. S. Chashunski, *Rev. Adv. Mater. Sci.* **20** (2008) 21.
- [221] D. Henwood, J. D. Carey., *Mol. Simul.* **34** (2008) 1019.
- [222] A. J. Cohen, P. Mori-Sánchez, W. Yang, *Science* **321** (2008) 792.
- [223] T. Ziegler, M. Seth, M. Kryknnov, J. Autschbach, F. Wang, *J. Mol. Struct. (Theochem)*, In press (2009).

VITA

Olçay Üzengi Aktürk was born in Eskişehir/Turkey in 1977.

1995-1999 Ege University, Physics, Theoretical Physics Programs, İzmir/Turkey Polarization of Light Senior Project: Prof. Dr. İsmet ERTAS

1999-2002 Anadolu University, Physics, MS, Eskişehir/Turkey Conduction Mechanisms in Solids Supervisor: Asst. Prof. Dr. Sabiha AKSAY

2001 She was married.

2003-2004 Middle East Technical University, Foreign Language Department, Ankara/Turkey

2004- She started her Ph.D. studies in condensed matter at Middle East Technical University

Publications:

1. O.Üzengi Aktürk, E.Aktürk and M.Tomak, Can Sobolev Inequality Be Written for Sharma-Mittal Entropy? , Int. J. of Theoretical Phys., 47 ,12, (2008)
2. O. Üzengi Aktürk , O.Gülseren and M.Tomak, Int. J. Modern Phys. B, **23**,31, (2009), 5819.
3. Olçay Üzengi Aktürk and Mehmet Tomak, to be published in Thin Solid Films
4. Olçay Üzengi Aktürk and Mehmet Tomak, Phys. Rev. B **80**, (2009), 085417.
5. Olçay Üzengi Aktürk and Mehmet Tomak, submitted to Thin Solid Films
6. Olçay Üzengi Aktürk and Mehmet Tomak, submitted to Apl.Phys.Lett.